JAMES | Journal of Advances in Modeling Earth Systems®

RESEARCH ARTICLE
10.1029/2022MS003126

Key Points:

- Ocean biogeochemical model represented the impact of photoprotective carotenoids (PPCs) in the light absorption coefficients of phytoplankton
- Proposed model characterized the global variability of phytoplankton light absorption when compared to in situ and satellite observations
- The impact of PPCs in phytoplankton light absorption reduced the dependence of reflectance on total chlorophyll

Supporting Information:

Supporting Information may be found in the online version of this article.

Correspondence to:

E. Álvarez,
ealvarez@ogs.it

Citation:

Álvarez, E., Losa, S. N., Bracher, A., Thoms, S., & Völker, C. (2022). Phytoplankton light absorption impacted by photoprotective carotenoids in a global ocean spectrally-resolved biogeochemistry model. *Journal of Advances in Modeling Earth Systems*, *14*, e2022MS003126. https://doi.org/10.1029/2022MS003126

Received 8 APR 2022
Accepted 20 SEP 2022

Author Contributions:

Conceptualization: Eva Álvarez, Svetlana N. Losa, Astrid Bracher, Silke Thoms, Christoph Völker
Data curation: Eva Álvarez, Astrid Bracher
Formal analysis: Eva Álvarez
Funding acquisition: Astrid Bracher, Christoph Völker
Methodology: Eva Álvarez

Phytoplankton Light Absorption Impacted by Photoprotective Carotenoids in a Global Ocean Spectrally-Resolved Biogeochemistry Model

Eva Álvarez[1], Svetlana N. Losa[2,3], Astrid Bracher[2,4], Silke Thoms[2], and Christoph Völker[2]

[1]National Institute of Oceanography and Applied Geophysics – OGS, Trieste, Italy, [2]Alfred Wegener Institute Helmholtz Centre for Polar and Marine Research, Bremerhaven, Germany, [3]Shirshov Institute of Oceanology, Russian Academy of Sciences, Moscow, Russia, [4]Institute of Environmental Physics, University of Bremen, Bremen, Germany

Abstract The chlorophyll-specific absorption spectrum of phytoplankton $\left[a^*_{\mathrm{PH}}(\lambda)\right]$ multiplied with phytoplankton chlorophyll provides the total absorption coefficient of phytoplankton $[a_{\mathrm{PH}}(\lambda)]$, a fundamental quantity with significance in many marine biogeochemical (BGC) and environmental processes. Representing accurately the sources of variability of $a_{\mathrm{PH}}(\lambda)$ in BGC ocean models is a crucial task. The two main sources of variability in $a^*_{\mathrm{PH}}(\lambda)$ are changes in the pigment composition of the phytoplankton community and the size-dependent constraints to pigment packaging. Therefore, changes in community structure and physiological state impact $a^*_{\mathrm{PH}}(\lambda)$ and consequently $a_{\mathrm{PH}}(\lambda)$. The objective of this work is to improve estimates of $a_{\mathrm{PH}}(\lambda)$ in a BGC model of the global ocean by portraying the variability of $a^*_{\mathrm{PH}}(\lambda)$ driven by the variable content in photoprotective carotenoids (PPCs) in the phytoplankton community. We used a three-dimensional spectrally-resolved BGC model to simulate the inherent and apparent optical properties of the global ocean based on its content on optically active constituents. The $a^*_{\mathrm{PH}}(\lambda)$ for each phytoplankton type represented in the model were made variable as a function of the type-specific content in PPCs. By comparing model-derived $a_{\mathrm{PH}}(\lambda)$ to satellite retrievals and an extensive field data set of optical and BGC observations, we concluded that photoprotective pigments content impacted significantly the contribution of the $a_{\mathrm{PH}}(\lambda)$ to the total non-water absorption in the ocean. Pigment-impacted $a^*_{\mathrm{PH}}(\lambda)$ contributed to reproduce the global variability of $a_{\mathrm{PH}}(\lambda)$ as well as the observed bio-optical relationship between $a_{\mathrm{PH}}(\lambda)$ and chlorophyll. The improved representation of the $a_{\mathrm{PH}}(\lambda)$ of the phytoplankton community influenced model simulations in terms of water-leaving radiances.

Plain Language Summary The multifaceted interactions between light and particles suspended in the ocean translate to complex light paths at larger scale, such as the color of the light that leaves the ocean, can be detected by satellites and is used to map the concentration of phytoplankton. In this work, we have developed an Earth-system biogeochemical model that represents how different colors of light travel though the ocean and interact with phytoplankton and other suspended matter. As phytoplankton cells contain a variety of algal pigments and different pigments absorb different colors of light, the amount and diversity of pigments found in the phytoplankton community determines how much and which color of light they absorb. In our model, the pigments that phytoplankton accumulate to protect themselves from the harmful effects of light alter the amount of light that the cells absorb in the blue-green region of the spectrum. Our model was able to better represent how much light phytoplankton absorbed when compared with many observations collected by expeditions and satellites in the global ocean. Our proposed model structure can have high potential implications in the future, from providing insight to the causes of changes in the color of the ocean to refining model estimates of phytoplankton production.

1. Introduction

Phytoplankton is one of the main optically-active constituents in the upper ocean. Light fuels photochemical reactions that allow phytoplankton to assimilate different nutrients (e.g., nitrate, phosphate, silica, and iron) and to fix carbon by photosynthesis. The total absorption coefficient of phytoplankton $[a_{\mathrm{PH}}(\lambda)]$ accounts for the light energy entering both: the photochemical pathway where it is used for photosynthesis, and the non-photochemical pathway where hence the energy is dissipated. Therefore, the $a_{\mathrm{PH}}(\lambda)$ contributes to the attenuation of light in the water column and influences the intensity and spectrum of the light that leaves the ocean. The $a_{\mathrm{PH}}(\lambda)$ of the phytoplankton community is a fundamental quantity in marine biogeochemical (BGC) and environmental processes

Resources: Svetlana N. Losa, Astrid Bracher, Christoph Völker
Software: Eva Álvarez, Svetlana N. Losa, Christoph Völker
Supervision: Christoph Völker
Validation: Eva Álvarez, Astrid Bracher
Visualization: Eva Álvarez
Writing – original draft: Eva Álvarez
Writing – review & editing: Svetlana N. Losa, Astrid Bracher, Silke Thoms, Christoph Völker

by impacting the underwater light field and consequently the photosynthetic response of phytoplankton. Hence, the value of $a_{\mathrm{PH}}(\lambda)$ is central for the understanding of the optical variability of oceanic waters and the coupling between available light and carbon fixation by phytoplankton.

The absorption properties of phytoplankton at different spatial and temporal scales have been widely studied in numerous regions of the world ocean (e.g., Bricaud et al., 2004; Lohrenz et al., 2003). The two main sources of variability in $a_{\mathrm{PH}}(\lambda)$ (m^{-1}) at a given chlorophyll a concentration (TChla, mg m^{-3}) are the influence of cellular pigment composition and pigment packaging (Bricaud et al., 2004). Algal pigments have distinguishable absorption bands in the visible region of the electromagnetic spectrum (Bidigare et al., 1990; Bricaud et al., 2004) and the type and quantity of pigments present in the phytoplankton community is affected by two main mechanisms. First, different phytoplankton groups are characterized by different pigment suites (Clementson & Wojtasiewicz, 2019; Sathyendranath et al., 1987) as they are adapted to the prevailing light conditions they encounter in the environment. And second, under fluctuating light conditions phytoplankton cells adjust their intracellular pigment content to balance light absorption and electron transport and therefore optimize photosynthesis, in a process called photoacclimation. Hence, $a_{\mathrm{PH}}(\lambda)$ varies with changes in the relative proportion of different types of pigments, either by shifts in community composition or by photoacclimation within a particular taxon. The packaging effect accounts for the decrease in the actual absorption coefficients with increasing size as result of geometrical constraints on pigment packaging inside the cells (Duyens, 1956). Given the covariation between TChla, accessory pigments content and the mean size of phytoplankton populations, chlorophyll-specific phytoplankton absorption coefficients ($a^*_{\mathrm{PH}}(\lambda) = a_{\mathrm{PH}}(\lambda)/\mathrm{TChla}$, m^2 $\mathrm{mgTChla}^{-1}$) were generally found to vary inversely to the chlorophyll concentration in natural communities (Bricaud et al., 1995, 2004; Organelli et al., 2011). This bio-optical relationship, explained by the interplay between changes in community size structure and pigment composition (Bricaud et al., 2004), signifies that the value of the community aggregated $a^*_{\mathrm{PH}}(\lambda)$ is variable.

The spectral shape and amplitude of the community aggregated $a^*_{\mathrm{PH}}(\lambda)$ reflect changes in phytoplankton physiology and species composition, tied to fluctuations in the physical and chemical environment. Photoprotective pigments accumulate in high-light-exposed communities and contribute to the dissipation of the excess energy that can be harmful to the photosynthetic machinery of microalgae. Variations in the relative proportions of carotenoid accessory pigments alter the shape of $a^*_{\mathrm{PH}}(\lambda)$. The difference between $a^*_{\mathrm{PH}}(490)$ and $a^*_{\mathrm{PH}}(530)$ (normalized to 676 nm) has been found to be larger in high-light compared to low-light adapted cultures (Johnsen et al., 1994). Therefore, under high light, increases in photoprotective carotenoids (PPCs), decreases in accessory photosynthetic carotenoids (PSCs), and a reduction in pigment packaging may cause the $a^*_{\mathrm{PH}}(\lambda)$ spectral slopes to become steeper, while the reverse is true for low-light conditions (Eisner et al., 2003). Furthermore, changes in PPC content relative to TChla may differ among taxa because there are taxonomic particularities (Lavaud et al., 2004; T. Key et al., 2010) and allometric constraints (Edwards et al., 2015; Finkel, 2004; Malerba & White, 2017) that influence the accumulation of pigments. Spectral variations in $a^*_{\mathrm{PH}}(\lambda)$ exist, then, due to the types and relative concentrations of phytoplankton and their physiological responses to growth conditions including light, nutrient availability, and temperature. This leads to temporal, spatial and depth variations in the spectral shapes of $a^*_{\mathrm{PH}}(\lambda)$ that are encountered in the ocean.

Radiative transfer models (e.g., Hydrolight by Sequoia Scientific, OARM by Gregg (2002), SCIATRAN by Rozanov et al. (2014)) capture the interactions of light scattering and absorption through the water column, and hence simulate the wavelength-dependent optical properties of the ocean based on its content on optically active constituents (OACs). BGC models that added radiative transfer components have the potential to advance in the understanding of the interaction of photophysiology with environmental drivers (e.g., Babin et al., 1993; Kettle & Merchant, 2008). An increasing number of studies demonstrate the value of adding spectrally-resolved optics to BGC models, from explicitly resolving inherent optical properties (IOPs; Fujii et al., 2007; Gregg & Casey, 2007), simulating spectral light habitats (Hickman et al., 2010; Holtrop et al., 2021; Salihoglu & Hofmann, 2007), simulating ocean color (Baird et al., 2016; Dutkiewicz et al., 2015; Gregg & Rousseaux, 2017; Xiu & Chai, 2014) to ultimately increase the amount and types of data comparable to model output, from satellite-based ocean color as well as other observed optical properties (e.g., Dutkiewicz et al., 2018; Fujii et al., 2007; Gregg & Rousseaux, 2017; Jones et al., 2016).

The in-water BGC constituents that affect ocean optical properties and can be defined as OAC in a radiative transfer model, include water molecules, phytoplankton, detrital matter, colored dissolved organic matter (CDOM), minerals, salt and air bubbles (Stramski et al., 2004). Although BGC models that include spectrally-resolved

optics differ in which BGC components they consider as OAC and rarely include them all, largely all of them do include phytoplankton. BGC models provide the abundance and distribution of a variable number of phytoplankton types in the ocean and therefore the information on $a^*_{\mathrm{PH}}(\lambda)$ and its variations is central for deriving $a_{\mathrm{PH}}(\lambda)$ from phytoplankton biomass (IOCCG, 2020). Mostly, the underlying optical relationships used to compute $a_{\mathrm{PH}}(\lambda)$ are dependent on empirically-derived constant $a^*_{\mathrm{PH}}(\lambda)$ spectra, and hence $a_{\mathrm{PH}}(\lambda)$ depends on the concentration of the corresponding model state variables (commonly Chla) and on the $a^*_{\mathrm{PH}}(\lambda)$ spectra prescribed for each phytoplankton type. The predefined spectral shapes for $a^*_{\mathrm{PH}}(\lambda)$ are derived from both different phytoplankton taxa growing in culture (e.g., Dutkiewicz et al., 2015; Gregg & Rousseaux, 2016) or explicitly prescribing intracellular pigment concentrations and cell diameter for each phytoplankton type (e.g., Baird et al., 2016). In these BGC models that employ a limited number of constant $a^*_{\mathrm{PH}}(\lambda)$ spectra, $a_{\mathrm{PH}}(\lambda)$ is therefore an emergent property of solely the feedbacks involving the production and transport of the BGC products, just reflecting the impact on $a_{\mathrm{PH}}(\lambda)$ of shifts in community composition. While larger scale estimates of reasonable accuracy may be achievable with the use of constant type-specific $a^*_{\mathrm{PH}}(\lambda)$ spectra, it is important to recognize that these spectra themselves must be representative of the phytoplankton optical types found in the ocean. And even being representative, by not considering the impact of photoacclimation processes, they imply simplifications in the description of photophysiology, which can decrease the ability of coupled BGC-optical models in capturing the full range of temporal and spatial variability of $a_{\mathrm{PH}}(\lambda)$.

A limited number of spectrally-resolved BGC models allow the $a^*_{\mathrm{PH}}(\lambda)$ of each phytoplankton type to vary (e.g., Fujii et al., 2007; Xiu & Chai, 2014), all of them based on the EcoLight setup, which makes $a^*_{\mathrm{PH}}(\lambda)$ variable based on the content of photosynthetic pigments. These authors consider the impact on the shape of $a^*_{\mathrm{PH}}(\lambda)$ of both changes in community composition and photoacclimation by scaling two $a^*_{\mathrm{PH}}(\lambda)$ spectra (measured under high-light and low-light conditions, respectively) with the chlorophyll to carbon ratio. This means they assume implicitly that changes in the content of photosynthetic pigments (i.e., Chl:C ratio) do not affect the relative contribution of non-photosynthetic pigments to $a^*_{\mathrm{PH}}(\lambda)$, which seems to be the case for PSC and PPC (Barlow et al., 2002) but not always for Chl-a and PPC, depending on the phytoplankton type being considered (Barlow et al., 2013). No BGC model that includes spectrally-resolved optics has considered explicitly, to the best of our knowledge, the impact of a variable pool of PPC in the shape of $a^*_{\mathrm{PH}}(\lambda)$ and the resultant impact on the global estimates of $a_{\mathrm{PH}}(\lambda)$. This circumstance is mostly attributable to the fact that BGC models of the ocean do not include comprehensive estimates about the amount and diversity of pigments accumulated by phytoplankton. Given the significance of $a_{\mathrm{PH}}(\lambda)$ in many marine BGC and environmental processes, failing to capture the full range of temporal and spatial variability of $a_{\mathrm{PH}}(\lambda)$ observed in the global ocean, can eventually decrease the ability of the models to accurately simulate the underwater light field and consequently primary production.

The Regulated Ecosystem Model version 2 (REcoM2; Hohn, 2009; Schartau et al., 2007) is a relatively simple ecosystem model in terms of number of phytoplankton types but recently has been extended to simulate a comprehensive pigment signature of the phytoplankton community in terms of photosynthetic pigments (Chl-a) and PPCs (Álvarez et al., 2019). Briefly, the rationale is based on a photoinhibition model proposed by H. L. Marshall et al. (2000), that accounts for changes in the optical absorption cross section of the cells, defined as light absorbed per unit length, and in the photochemical efficiency of the photosystems (PSII), defined as carbon fixed per unit of light absorbed, driven by the relative number of active reaction centers (D1) in PSII. The decrease in both variables under high light and in the absence of a variable pool of PPC leads to the photoinhibition of the light harvesting apparatus and therefore to the decrease in the photosynthetic rate. Assuming that photoinhibition is minimal in phytoplankton communities adapted to prevailing light conditions, the difference between the product of the maximum values of the optical absorption cross section and photochemical efficiency and the product of their non-photoprotected counterparts accounts for the amount of PPC relative to Chl-a that each phytoplankton group needs to accumulate to avoid such photoinhibition. This PPC:Chla ratio includes all xanthophylls potentially involved in photoprotection. This comprises both epoxidated and de-epoxidated states, because the timescale of xanthophyll cycling is much shorter (less than a day) than that of photoacclimation, and both, epoxidated and de-epoxidated xanthophylls act as photoprotective in the medium to long term (more than a day). This also comprises xanthophylls associated to different phytoplankton taxa, because, rather than assuming any particular short-term mechanism of action for a given xanthophyll type, the PPC:Chla ratio simulates the resilience of the phytoplankton type to photodamage. Therefore, when this version of REcoM2 was used to simulate the global ocean, the community aggregated value of PPC relative to total chlorophyll (TChla) in the whole phytoplankton community was observed to be highly correlated with observations of PPC content that consisted

of alloxanthin (Allo), lutein (Lut), violaxanthin (Viola), zeaxanthin (Zea), diadinoxanthin (DD), diatoxanthin (DT), and α/β-carotenes (Caro).

The objective of the presented study is to improve the representation of the variability of $a_{\mathrm{PH}}(\lambda)$ within a coupled BGC-optical model of the ocean by accounting for the impact on $a^*_{\mathrm{PH}}(\lambda)$ of a variable PPC:Chla ratio in each phytoplankton type represented. With this aim, we coupled a state-of-the-art radiative transfer model (Dutkiewicz et al., 2015) to the REcoM2 ecosystem model. To assess how the variable composition of PPC pigments influences the variability in phytoplankton $a_{\mathrm{PH}}(\lambda)$ observed in nature, we first evaluated to what extent the use of constant $a^*_{\mathrm{PH}}(\lambda)$ for the phytoplankton types represented in the model captured the optical properties of the ocean and its OACs and BGC products. Alternatively, we proposed an approach to include variability in the $a^*_{\mathrm{PH}}(\lambda)$ of the phytoplankton types using the stoichiometry of PPC. The proposed model setup yields total and type-specific $a^*_{\mathrm{PH}}(\lambda)$ as a continuous function of the PPC:Chl-a ratio linked empirically through the correlation between PPC:Chl-a and the spectral shape of $a^*_{\mathrm{PH}}(\lambda)$ obtained from in situ global observations. By comparing $a_{\mathrm{PH}}(\lambda)$ simulated by both model setups with a global compilation of independent in situ $a_{\mathrm{PH}}(\lambda)$ measurements as well of satellite retrieved $a_{\mathrm{PH}}(\lambda)$, we evaluated the ability of both model setups in representing the global variability of $a_{\mathrm{PH}}(\lambda)$. Finally, we explored how these two representations of the light harvesting capabilities of the phytoplankton community influenced model simulations in terms of remote sensing reflectance and how model output compared to in situ data and satellite retrievals.

2. Materials and Methods

The methods section includes the description of the modeling framework and outlines how a radiative transfer component was incorporated into the coupled physical-BGC model, and how phytoplankton growth and physiology were described under spectral light (Section 2.1). Afterward, it describes the model experiments performed (Section 2.2).

2.1. Model Framework

The modeling framework was shaped by three elements: (a) a radiative transfer model that resolves the underwater spectral light field based on the presence in the water column of OAC, (b) the REcoM2 that describes the biogeochemistry in the ocean and hence simulates the distributions of OAC, and (c) the MIT general circulation model (MITgcm) that advects and mixes the BGC variables. Figure 1 shows how these three parts integrated.

2.1.1. Radiative Transfer Model

The radiative transfer model described in Dutkiewicz et al. (2015) was coupled to REcoM2, implementing the code that was made public with Dutkiewicz et al. (2018) and available at Dutkiewicz (2018) as the package *monod* version 1 designed for the MITgcm. A complete description of the code can be found in those publications but here we present a summary of the steps performed to fit the code into REcoM2 (Álvarez, Losa, et al., 2022). Briefly, the radiative transfer component followed the propagation of light through the water column in 13 wavebands that cover the visible part of the light spectrum. The nominal wavelengths of the bands are distributed in 25 nm intervals from 400 to 700 nm. From 425 to 675, the bands have a bandwidth of 25 nm and are centered at the nominal wavelength. First (400 nm) and last (700 nm) bands have a bandwidth of 12.5 nm and the nominal wavelength represents the lower and the upper extreme, respectively. The radiative transfer component resolved the penetration of light in each waveband as it was absorbed and scattered within the water column by several OAC, namely two phytoplankton types, detrital particles (non-algal particles, NAP) and CDOM. Therefore, it simulated the spectral irradiance available for BGC processes in the water column and the spectral irradiance that reached again the surface of the ocean.

2.1.1.1. Input Light

Incoming spectral irradiance at the top of the ocean was obtained from the data product derived from the Ocean-Atmosphere Spectral Irradiance Model (OASIM; Gregg and Casey (2009)) and available at the NASA Global Modeling and Assimilation Office ftp (NOBM, 2019). OASIM data contained two downward streams just below the surface of the ocean: direct $[E^{\mathrm{below}}_{d0}(\lambda)]$ and diffuse $[E^{\mathrm{below}}_{s0}(\lambda)]$, both in W m^{-2} and averaged in 33 wavebands with monthly resolution. We collected the 13 wavebands between 400 and 700 nm used in the model and created a climatological year combining data from year 2008–2012 to be used as surface forcing to the model.

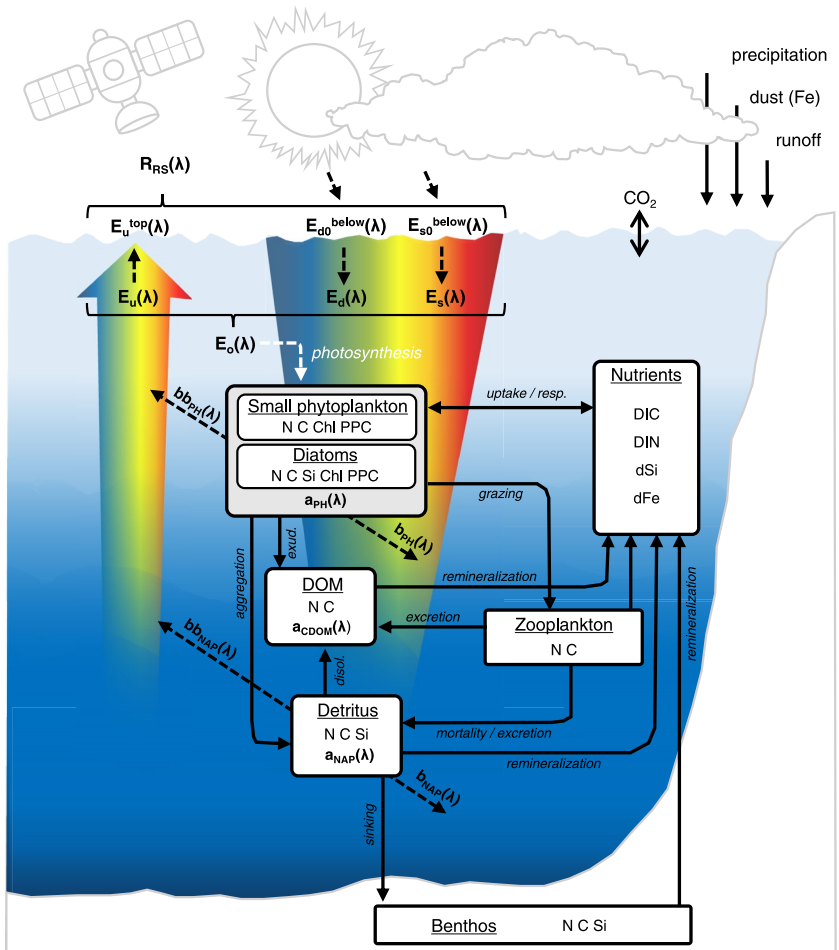

Figure 1. Schematic representation of the biogeochemical (BGC) model Regulated Ecosystem Model version 2 (REcoM2) and the radiative transfer model (Dutkiewicz et al., 2015, 2018) used for this study. REcoM2 represents two phytoplankton types (small phytoplankton and diatoms), one zooplankton type and compartments for the dissolved organic matter (DOM), detritus, the benthos and the main inorganic nutrients (DIN, dSi, and dFe). The BGC components in REcoM2 are represented by their elemental components, among carbon (C), nitrogen (N), silica (Si), chlorophyll (Chl), and photoprotective carotenoids (PPC). Solid arrows represent the BGC processes that link the different components. Dashed arrows represent the processes described by the radiative transfer model and therefore are resolved spectrally. All abbreviations are explained in Table 1.

2.1.1.2. Three Streams

Vertically-resolved irradiance was described with three state variables: direct $[E_d(\lambda)]$ and diffuse $[E_s(\lambda)]$ downward components and an upward diffuse component $[E_u(\lambda)]$, all in W m^{-2}. The three-stream propagation along the depth of the water column (z) was resolved by the following system of differential equations (Aas, 1987; Ackleson et al., 1994; Gregg, 2002):

$$d\,E_d(\lambda)/dz = -\frac{a(\lambda)+b(\lambda)}{\overline{\upsilon_d}} \cdot E_d(\lambda) \tag{1}$$

$$d\,E_s(\lambda)/dz = -\frac{a(\lambda)+r_s \cdot bb(\lambda)}{\overline{\upsilon_s}} \cdot E_s(\lambda) + \frac{r_u \cdot bb(\lambda)}{\overline{\upsilon_u}} \cdot E_u(\lambda) + \frac{b(\lambda)-r_d \cdot bb(\lambda)}{\overline{\upsilon_d}} \cdot E_d(\lambda) \tag{2}$$

$$-d\,E_u(\lambda)/dz = -\frac{a(\lambda)+r_u \cdot bb(\lambda)}{\overline{\upsilon_u}} \cdot E_u(\lambda) + \frac{r_s \cdot bb(\lambda)}{\overline{\upsilon_s}} \cdot E_s(\lambda) + \frac{bb(\lambda)}{\overline{\upsilon_d}} \cdot E_d(\lambda) \tag{3}$$

where $a(\lambda)$, $b(\lambda)$, and $bb(\lambda)$ are the total absorption, scattering and backscattering coefficients, respectively (all in m^{-1}), which are independent of the ambient light field and defined as IOPs. r_d, r_s, and r_u are the effective scattering coefficients, and $\overline{\upsilon_d}$, $\overline{\upsilon_s}$, and $\overline{\upsilon_u}$ are the average direction cosines of the three irradiance streams, which are constant for diffuse radiance but vary with solar zenith angle for direct radiance (Table 1).

The IOPs $a(\lambda)$, $b(\lambda)$, and $bb(\lambda)$ depend on the additive contribution of seawater and the OAC present in the water, as follows:

$$a(\lambda) = a_W(\lambda) + a_{\mathrm{NAP}}(\lambda) + a_{\mathrm{CDOM}}(\lambda) + a_{\mathrm{PH}}(\lambda) \tag{4}$$

$$b(\lambda) = b_W(\lambda) + b_{\mathrm{NAP}}(\lambda) + b_{\mathrm{PH}}(\lambda) \tag{5}$$

$$bb(\lambda) = b_W(\lambda) \cdot br_W + b_{\mathrm{NAP}}(\lambda) \cdot br_{\mathrm{NAP}} + bb_{\mathrm{PH}}(\lambda) \tag{6}$$

where $a(\lambda)$ results from the absorption by water molecules ($a_W(\lambda)$, m^{-1}), NAP ($a_{\mathrm{NAP}}(\lambda)$, m^{-1}), CDOM ($a_{\mathrm{CDOM}}(\lambda)$, m^{-1}), and phytoplankton ($a_{\mathrm{PH}}(\lambda)$, m^{-1}); $b(\lambda)$ and $bb(\lambda)$ result from the scattering and backscattering, respectively, by water ($b_W(\lambda)$, m^{-1}), NAP ($b_{\mathrm{NAP}}(\lambda)$, m^{-1}) and phytoplankton ($b_{\mathrm{PH}}(\lambda)$, m^{-1}). We did not consider any wavelength dependency on the $b(\lambda)$ to $bb(\lambda)$ ratio for any of the constituents, hence $bb(\lambda)$ was computed for all constituents as their respective $b(\lambda)$ times a constant backscattering to total scattering ratio, that was 0.5 for water (br_W; Morel, 1974) and 0.005 for NAP (br_{NAP}; Gallegos et al., 2011) (Table 1).

2.1.1.3. Solution

To resolve the three-stream system of equations (Equations 1–3), the *monod* version 1 package provides several alternatives (Dutkiewicz, 2018). We used the direct solver that integrates the $E_d(\lambda)$ equation exactly, and computes $E_s(\lambda)$ and $E_u(\lambda)$ by solving a set of linear equations for the amplitudes in the exact solution (see e.g., Kylling et al., 1995). At the bottom of each depth layer, the method computed the direct [$E_d^{\mathrm{bottom}}(\lambda)$] and diffuse [$E_s^{\mathrm{bottom}}(\lambda)$] downward irradiances and the upward irradiance [$E_u^{\mathrm{bottom}}(\lambda)$]. At the top of each layer, it computed the diffuse downward [$E_s^{\mathrm{top}}(\lambda)$] and the upward [$E_u^{\mathrm{top}}(\lambda)$] irradiances which are equal to $E_s^{\mathrm{bottom}}(\lambda)$ and $E_u^{\mathrm{bottom}}(\lambda)$ of the layer above. For details about the solution of the three-stream system see Dutkiewicz et al. (2018, 2015).

At the center of the depth layer, $E_d(\lambda)$, $E_s(\lambda)$, and $E_u(\lambda)$ were averaged geometrically between the top and the bottom of the layer. Total scalar irradiance, $E_0(\lambda)$, was computed by scaling the three streams by their inverse average direction cosines. $E_0(\lambda)$ was converted from irradiance values in units of W m^{-2} to photon flux given in μmol quanta m^{-2} d^{-1} by multiplying by λ in meters, dividing by the product of the Avogadro's constant, h (Planck's constant), and c (speed of light) and converting mol quanta to μmol quanta and s^{-1} to d^{-1}:

$$E_0(\lambda) = \left[E_d(\lambda)/\overline{\upsilon_d} + E_s(\lambda)/\overline{\upsilon_s} + E_u(\lambda)/\overline{\upsilon_u}\right] \cdot \lambda \cdot \frac{1\,\mathrm{m}}{10^9\mathrm{nm}} \cdot \frac{1}{h \cdot c \cdot 6.23 \cdot 10^{23}} \cdot \frac{10^6 \mu\mathrm{mol\,quanta}}{1\,\mathrm{mol\,quanta}} \cdot 86,400\,\mathrm{s/d} \tag{7}$$

$E_0(\lambda)$ was the light available for phytoplankton growth (see Equation 19 in Section 2.1.3), and its integral value from 400 to 700 nm constituted the photosynthetically active radiation (PAR) that was used as the common light input for all non-spectrally resolved processes, that in our set up were the CDOM photobleaching (see Equation 24 in Section 2.1.3) and the inactivation of PSII in the pigments model (Section 2.1.4).

$$\mathrm{PAR} = \int_{400}^{700} E_0(\lambda)\, d\lambda \tag{8}$$

After solving the water column light penetration, the subsurface reflectance [$R_0(\lambda)$] was computed as the dimensionless ratio between $E_u^{\mathrm{top}}(\lambda)$ in the most superficial layer ($k = 1$) relative to the incoming irradiance just below ocean surface [$E_{d0}^{\mathrm{below}}(\lambda) + E_{s0}^{\mathrm{below}}(\lambda)$]:

$$R_0(\lambda) = E_u^{\mathrm{top}}(\lambda)[k = 1] / \left(E_{d0}^{\mathrm{below}}(\lambda) + E_{s0}^{\mathrm{below}}(\lambda)\right) \tag{9}$$

To compare to the reflectance seen by satellites, we converted $R_0(\lambda)$ to remote sensing reflectance, $R_{\mathrm{RS}}(\lambda, 0^-)$, using a bidirectional function Q, assumed as a constant value of 3 steradians (Morel et al., 2002). Q depends on several variables, including IOPs, wavelength and solar zenith angles but constant Q has been employed before

Table 1
Definitions of Variables and Parameters Included in the Bio-Optical Component

Name	Description	Value	Unit	Source
Input variables				
$E_{d0}^{\text{below}}(\lambda)$	Direct stream of light below ocean surface	OASIM	W m^{-2}	NOBM (2019)
$E_{s0}^{\text{below}}(\lambda)$	Diffuse stream of light below ocean surface	OASIM	W m^{-2}	NOBM (2019)
State variables				
$E_d(\lambda)$	Downwelling direct stream	Equation 1	W m^{-2}	
$E_s(\lambda)$	Downwelling diffuse stream	Equation 2	W m^{-2}	
$E_u(\lambda)$	Upwelling stream	Equation 3	W m^{-2}	
Intermediate variables				
$R_0(\lambda)$	Below surface reflectance	Equation 9	–	
$R_{\text{RS}}(\lambda)$	Above surface remote-sensing reflectance	Equation 10	sr^{-1}	
$a(\lambda)$	Total light absorption	Equation 4	m^{-1}	
$b(\lambda)$	Total light scattering	Equation 5	m^{-1}	
$bb(\lambda)$	Total light backscattering	Equation 6	m^{-1}	
$a_{\text{PH}}(\lambda)$	Light absorption by phytoplankton	Equation 11	m^{-1}	
$a_{\text{CDOM}}(\lambda)$	Light absorption by CDOM	Equation 15	m^{-1}	
$a^*_{\text{CDOM}}(\lambda)$	Mass-specific absorption coefficients of CDOM	Equation 15	m^2 mmolC^{-1}	
$a_{\text{NAP}}(\lambda)$	Light absorption by NAP	Equation 16	m^{-1}	
$a^*_{\text{NAP}}(\lambda)$	Mass-specific absorption coefficients of NAP	Equation 16	m^2 mmolC^{-1}	
$b_{\text{PH}}(\lambda)$	Light scattering by phytoplankton	Equation 13	m^{-1}	
$b_{\text{NAP}}(\lambda)$	Light scattering by NAP	Equation 17	m^{-1}	
$b^*_{\text{NAP}}(\lambda)$	Mass-specific scattering coefficients of NAP	Equation 17	m^2 mmolC^{-1}	
$bb_{\text{PH}}(\lambda)$	Light backscattering by phytoplankton	Equation 14	m^{-1}	
$\overline{\upsilon_d}$	Average direction cosine E_d stream	–	–	
Parameters				
$\overline{\upsilon_s}$	Average direction cosine E_s stream	0.83	–	Aas (1987)
$\overline{\upsilon_u}$	Average direction cosine E_u stream	0.4	–	Aas (1987)
r_d	E_d-specific scattering coefficient	1.0	–	Aas (1987)
r_s	E_s-specific scattering coefficient	1.5	–	Aas (1987)
r_u	E_u-specific scattering coefficient	3.0	–	Aas (1987)
$a_W(\lambda)$	Light absorption by seawater	Figure 2c	m^{-1}	Pope and Fry (1997)
$b_W(\lambda)$	Light scattering by seawater	Figure 2d	m^{-1}	Smith and Baker (1981)
$a^*_{\text{PH}}(\lambda)$	chl-specific absorption coefficients of phytoplankton	Figure 2c	m^2 mgChl^{-1}	Álvarez, Lazzari, et al. (2022)
$b^*_{\text{PH}}(\lambda)$	Mass-specific scattering coefficients of phytoplankton	Figure 2d	m^2 mmolC^{-1}	Dutkiewicz et al. (2015)
d_{CDOM} (450)	CDOM mass-specific absorption coefficient at 450 nm	0.18	m^2 mmolC^{-1}	Dutkiewicz et al. (2015)
S_{CDOM}	CDOM absorption spectral slope	0.021	nm^{-1}	Kitidis et al. (2006)
d_{NAP}(440)	NAP mass-specific absorption coefficient at 440 nm	0.016	m^2 mmolC^{-1}	Dutkiewicz et al. (2015)
S_{NAP}	NAP absorption spectral slope	0.013	nm^{-1}	Gallegos et al. (2011)
e_{NAP} (550)	NAP mass-specific scattering coefficient at 550 nm	0.345	m^2 mmolC^{-1}	Dutkiewicz et al. (2015)
f_{NAP}	NAP exponent for scattering	0.5	–	Gallegos et al. (2011)

Table 1
Continued

Name	Description	Value	Unit	Source
br_W	Backscattering to total scattering ratio of water	0.5	–	Morel (1974)
br_{NAP}	Backscattering to total scattering ratio of NAP	0.005	–	Gallegos et al. (2011)
$br_{\mathrm{PH}}^{\mathrm{phy}}$	Backscattering to total scattering ratio small phyto	$1.17{\cdot}10^{-4}$	–	Stramski et al. (2001)
$br_{\mathrm{PH}}^{\mathrm{dia}}$	Backscattering to total scattering ratio diatoms	$2.88{\cdot}10^{-5}$	–	Stramski et al. (2001)

Note. All parameter values are included in the up-to-date working directory to run the experiments (Data Availability Statement section).

(Dutkiewicz et al., 2018; Gregg & Rousseaux, 2017). And lastly we converted $R_{\mathrm{RS}}(\lambda, 0^-)$ to above surface remote sensing reflectance $[R_{\mathrm{RS}}(\lambda, 0^+)]$ with the conversion by Lee et al. (2002):

$$R_{\mathrm{RS}}\left(\lambda, 0^+\right) = (0.52 \cdot R_{\mathrm{RS}}(\lambda, 0^-)) \,/\, (1 - 1.7 \cdot R_{\mathrm{RS}}(\lambda, 0^-))\,;\; R_{\mathrm{RS}}(\lambda, 0^-) = R_0(\lambda)/Q \tag{10}$$

Hereafter, we refer to this quantity as $R_{\mathrm{RS}}(\lambda)$ that has units of sr^{-1}.

2.1.2. Treatment of Optically Active Constituents

For each non-water constituent, their IOPs were computed as the product of the constituent mass and their respective mass-specific absorption or scattering coefficients. $a_W(\lambda)$ spectrum was taken from Pope and Fry (1997), and $b_W(\lambda)$ from Smith and Baker (1981). The spectra of the IOPs of each constituent are presented in Figure 2.

2.1.2.1. Phytoplankton

To describe the optical properties of phytoplankton we used chlorophyll-specific absorption spectra of phytoplankton taxa growing in culture, digitized from literature and provided as Supporting Information S1 to Álvarez, Lazzari, et al. (2022). Briefly, Álvarez, Lazzari, et al. (2022) collected published chlorophyll-specific absorption spectra for phytoplankton taxa growing in culture under different conditions of light, nutrient supply, and temperature. From this collection of spectra, we only considered for further analysis spectra of marine taxa which were normalized by total chlorophyll in the original publication ($n = 177$). Absorption spectra ($a^*_{PH}(\lambda)$) were averaged for six phytoplankton types that gather taxa similar in their pigmentary content, *Prochlorococcus*, *Synechococcus*, small eukaryotes, green algae, brown algae and diatoms. We assigned for each of these phytoplankton types a particular set of four pigment groups. All of them contained Chl-a, PSC and PPC. As the fourth pigment group, we assigned phycoerythrin (PEB) to *Synechococcus*, chlorophyll b (CHLB) to green algae and *Prochlorococcus* and chlorophyll c (CHLC) to the other groups (brown algae, small eukaryotes and diatoms). Figure 2 shows all spectra considered for small phytoplankton (Figure 2a) and for diatoms (Figure 2b), color-coded by the fourth pigment group.

Absorption spectra of photosynthetic pigments ($a^*_{\mathrm{PS}}(\lambda)$) were obtained by adjusting $a^*_{\mathrm{PH}}(\lambda)$ to the ratio of light absorption by photosynthetic to total pigments following Hickman et al. (2010). The relative pigment concentrations for the reconstructions were calculated by scaling the weight specific absorption spectra for each pigment group (Bidigare et al., 1990) to yield the lowest sum of residuals between the reconstructed spectrum and the measured $a^*_{\mathrm{PH}}(\lambda)$ (Hickman et al., 2010). $a^*_{PS}(\lambda)$ was reconstructed using the obtained relative concentrations just for the photosynthetic pigments (Babin et al., 1996). The absorption spectra, both $a^*_{\mathrm{PH}}(\lambda)$) and $a^*_{\mathrm{PS}}(\lambda)$, for the small phytoplankton group represented in the model were the averaged ones from *Prochlorococcus*, *Synechococcus*, green algae, brown algae and small eukaryotes (Figure 2a, black lines). The absorption spectra for the diatoms group in the model were the integrated only by diatom species (Figure 2b, black lines).

The resultant $a^*_{\mathrm{PH}}(\lambda)$ were used to compute total absorption by phytoplankton ($a_{\mathrm{PH}}(\lambda)$, m^{-1}) as the sum of the products of phytoplankton chlorophyll ($\mathrm{Chl}^{\mathrm{phy}}$ and $\mathrm{Chl}^{\mathrm{dia}}$, mg Chla m^{-3}) and the chlorophyll-specific coefficients (m^2 mg Chla^{-1}) of small phytoplankton ($a^{*\mathrm{phy}}_{\mathrm{PH}}(\lambda)$) and diatoms ($a^{*\mathrm{dia}}_{\mathrm{PH}}(\lambda)$) (Figure 2c):

$$a_{\mathrm{PH}}(\lambda) = a^{*\mathrm{phy}}_{\mathrm{PH}}(\lambda) \cdot \left[\mathrm{Chl}^{\mathrm{phy}}\right] + a^{*\mathrm{dia}}_{\mathrm{PH}}(\lambda) \cdot \left[\mathrm{Chl}^{\mathrm{dia}}\right] \tag{11}$$

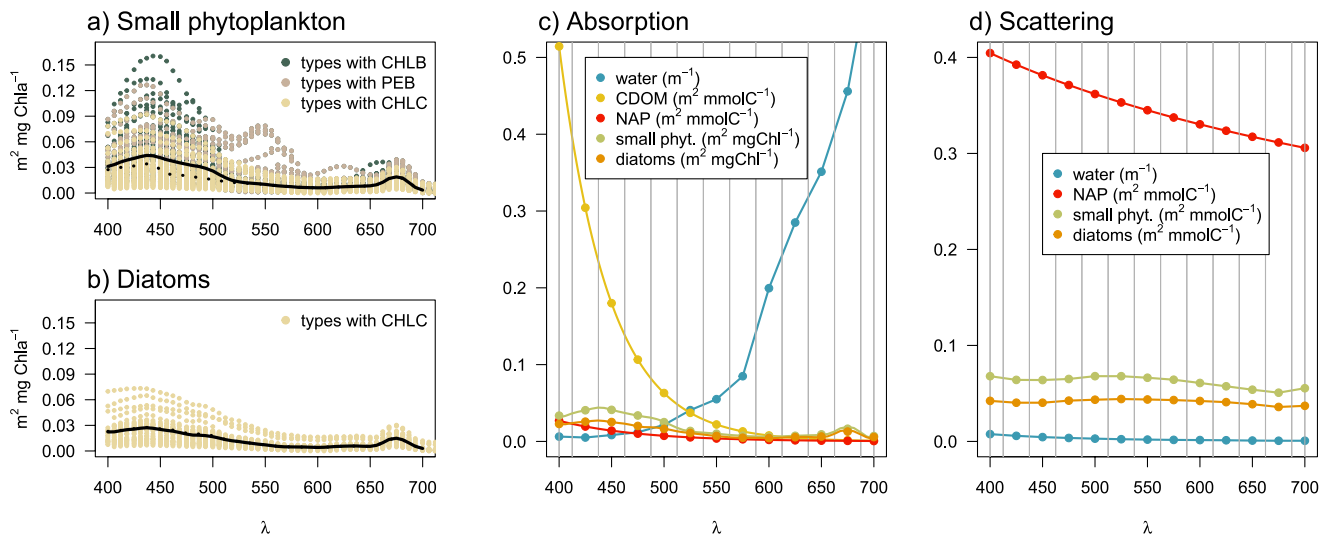

Figure 2. Inherent optical properties of water constituents: $a^*_{\mathrm{PH}}(\lambda)$ and $a^*_{\mathrm{PS}}(\lambda)$ coefficients for (a) small phytoplankton and (b) diatoms. Dotted lines show the collection of $a^*_{\mathrm{PH}}(\lambda)$ spectra collected from literature, color-coded by the fourth pigment group assigned to each taxon. Black lines show the averaged $a^*_{\mathrm{PH}}(\lambda)$ spectrum (solid line) and the $a^*_{\mathrm{PS}}(\lambda)$ spectrum reconstructed (dashed line) for each phytoplankton type represented in the model. Mass-specific (c) absorption (and $a_W(\lambda)$) and (d) scattering (and $b_W(\lambda)$) coefficients of all OAC in the model.

Cellular absorption cross-section for all pigments ($\overline{a}^*_{\mathrm{PH}}$, m^2 mgChla^{-1}) and just for the photosynthetic pigments ($\overline{a}^*_{\mathrm{PS}}$, m^2 mgChla^{-1}) were computed as the average of $a^*_{\mathrm{PH}}(\lambda)$ and $a^*_{\mathrm{PS}}(\lambda)$ between 400 and 700 nm, respectively. $\overline{a}^*_{\mathrm{PS}}$ values of 0.0143 and 0.0115 m^2 mgChla^{-1} were derived for small phytoplankton and diatoms, respectively. Equation 12 only shows the computation of $\overline{a}^*_{\mathrm{PS}}$ but the computation of $\overline{a}^*_{\mathrm{PH}}$ is equivalent substituting $a^*_{\mathrm{PS}}(\lambda)$ by $a^*_{\mathrm{PH}}(\lambda)$:

$$\overline{a}^*_{\mathrm{PS}} = \int_{400}^{700} a^*_{\mathrm{PS}}(\lambda)\, d\lambda/(700-400) \tag{12}$$

The scattering and backscattering coefficients of phytoplankton were assumed to be functions of phytoplankton biomass ($\mathrm{C}^{\mathrm{phy}}$ and $\mathrm{C}^{\mathrm{dia}}$, mmolC m^{-3}) and the mass-specific spectra used in Dutkiewicz et al. (2015). The mass-specific scattering spectrum for diatoms ($b^{*\mathrm{dia}}_{PH}(\lambda)$, m^2 mmolC^{-1}) was identical, and for small phytoplankton ($b^{*\mathrm{phy}}_{PH}(\lambda)$, m^2 mmolC^{-1}) was the average among two *Prochlorococcus* ecotypes, *Synechococcus*, small eukaryotes and coccolithophores (Figure 2d). The scattering coefficients by all phytoplankton ($b_{\mathrm{PH}}(\lambda)$, m^{-1}) was computed as the sum of the products of the phytoplankton biomass and the mass-specific scattering spectrum for each of the two phytoplankton types:

$$b_{\mathrm{PH}}(\lambda) = b^{*\mathrm{phy}}_{PH}(\lambda)\cdot\left[\mathrm{C}^{\mathrm{phy}}\right] + b^{*\mathrm{dia}}_{\mathrm{PH}}(\lambda)\cdot\left[\mathrm{C}^{\mathrm{dia}}\right] \tag{13}$$

We did not consider any wavelength dependency on the total scattering to backward scattering ratio of phytoplankton; hence, total backscattering of phytoplankton ($bb_{\mathrm{PH}}(\lambda)$, m^{-1}) was computed as the total scattering of each phytoplankton type multiplied by a constant backscattering to total scattering ratio, that was 0.038 for small phytoplankton ($br^{\mathrm{phy}}_{\mathrm{PH}}$) and 0.118 for diatoms ($br^{\mathrm{dia}}_{\mathrm{PH}}$) (Dutkiewicz et al., 2015).

$$bb_{\mathrm{PH}}(\lambda) = b^{*\mathrm{phy}}_{\mathrm{PH}}(\lambda)\cdot br^{\mathrm{phy}}_{\mathrm{PH}}\cdot\left[\mathrm{C}^{\mathrm{phy}}\right] + b^{*\mathrm{dia}}_{\mathrm{PH}}(\lambda)\cdot br^{\mathrm{dia}}_{\mathrm{PH}}\cdot\left[\mathrm{C}^{\mathrm{dia}}\right] \tag{14}$$

2.1.2.2. CDOM

As generally defined, CDOM only absorbs and does not scatter light. $a_{\mathrm{CDOM}}(\lambda)$ (m^{-1}) was computed as the product of CDOM biomass ($\mathrm{C}^{\mathrm{CDOM}}$, mmolC m^{-3}) and the mass-specific absorption coefficients ($a^*_{\mathrm{CDOM}}(\lambda)$, m^2 mmolC^{-1}) that decrease exponentially with increasing wavelength (Figure 2c), as:

$$a_{\mathrm{CDOM}}(\lambda) = a^*_{\mathrm{CDOM}}(\lambda)\cdot\left[\mathrm{C}^{\mathrm{CDOM}}\right] = d_{\mathrm{CDOM}}(450)\cdot\exp\left[-S_{\mathrm{CDOM}}\cdot(\lambda-450)\right]\cdot\left[\mathrm{C}^{\mathrm{CDOM}}\right] \tag{15}$$

where $d_{CDOM}(450)$ is the mass-specific absorption coefficient at 450 nm, and S_{CDOM} is the spectral slope of the absorption coefficients (Kitidis et al., 2006) that we considered as 0.021 nm^{-1} (Table 1).

2.1.2.3. NAP

NAPs absorb and scatter light. Here, we did not use absorption and scattering coefficients per particle as done in Dutkiewicz et al. (2015) and that require to assume a uniform size distribution of NAP, and used instead mass-specific coefficients as done by Gregg and Rousseaux (2017). An additional test comparing both approaches showed little differences in terms of total NAP absorption and scattering (Text S4 in Supporting Information S1). NAP absorption ($a_{NAP}(\lambda)$, m^{-1}), was computed as the product of the carbon component of detritus (C^{det}, mmolC m^{-3}) and the mass-specific absorption coefficients of NAP ($a^*_{NAP}(\lambda)$, m^2 $mmolC^{-1}$, Figure 2c), which decrease exponentially with increasing wavelength (Gallegos et al., 2011), as:

$$a_{NAP}(\lambda) = a^*_{NAP}(\lambda) \cdot \left[C^{det}\right] = d_{NAP}(440) \cdot \exp\left[-S_{NAP} \cdot (\lambda - 440)\right] \cdot \left[C^{det}\right] \tag{16}$$

where $d_{NAP}(440)$ is a mass-specific absorption coefficient at 440 nm of 0.016 m^2 $mmolC^{-1}$, and S_{NAP} is the spectral slope of the absorption coefficients that we considered as 0.013 nm^{-1} (Table 1). The NAP scattering coefficient ($b_{NAP}(\lambda)$, m^{-1}) was computed as the product of C^{det} and the mass-specific scattering coefficients$\left(b^*_{NAP}(\lambda)\right.$, m^2 $mmolC^{-1}$, Figure 2d), which are computed as an exponential function of wavelength (Gallegos et al., 2011), as:

$$b_{NAP}(\lambda) = b^*_{NAP}(\lambda) \cdot \left[C^{det}\right] = e_{NAP}(550) \cdot (550/\lambda)^{f_{NAP}} \cdot \left[C^{det}\right] \tag{17}$$

where $e_{NAP}(550)$ is a mass-specific scattering at the reference wavelength 550 nm of 0.345 m^2 $mmolC^{-1}$ and f_{NAP} an exponent of 0.5 (Table 1).

2.1.3. Biogeochemical Model

REcoM2 describes the biogeochemistry in the ocean with an ecological model that includes two phytoplankton functional types (small phytoplankton and diatoms), one zooplankton and one detritus compartment, and inorganic and organic forms of C, N, Si, and Fe. Details about the complete model set up can be consulted elsewhere (Hauck et al., 2013; Schartau et al., 2007). In the next sub-sections we report those equations connected to the sources and sinks of OAC, specifically phytoplankton growth and photoacclimation, and the production of NAP and CDOM.

Phytoplankton is described by their elemental components with flexible stoichiometry, which were carbon (C), nitrogen (N), and chlorophyll (Chl) for small phytoplankton and also silica (Si) for diatoms. Cellular Fe content is assumed to be proportional to N. Phytoplankton growth is a function of temperature, nutrient availability and irradiance. Temperature regulates metabolic rates with an Arrhenius function (Tfunc, dimensionless) of the local temperature (T in Kelvin), relative to a reference temperature (T_{ref}, Table 2). Nutrients limit phytoplankton growth depending on the internal quota of N and Si, and on the external concentration of Fe (Hauck et al., 2013). The multi-nutrient limitation is described by Liebig's law, where the most limiting nutrient, among N and Fe for small phytoplankton and among N, Fe, and Si for diatoms, limits the process (Nlimit, dimensionless). Irradiance controls photosynthesis and photoacclimation, and both were modified to resolve them spectrally.

The rate of change of carbon compounds in phytoplankton (C^{phy} and C^{dia}, mmolC m^{-3}) depends on the production through gross photosynthesis (P^C_{phot}, d^{-1}) and the losses by respiration, excretion, aggregation and predation:

$$\frac{d\boldsymbol{C}}{dt} = \left(P^C_{phot} - \text{Respiration} - \text{Excretion} - \text{Aggregation}\right) \cdot [C] - \text{Predation} \tag{18}$$

P^C_{phot} represents the mass-specific rate of incorporation of inorganic carbon into particulate organic matter. The formulation of the loss terms can be consulted in the supplementary material to Hauck et al. (2013). $P^C_{phot}$is largely a saturating function of the available PAR, commonly described by a family of empirical relationships between production and irradiance, known as PE curves. In REcoM2, P^C_{phot} is described by an exponential formulation (Webb et al., 1974) where the initial slope of the PE curve (α) encompasses two concepts: (a) $a^*_{PS}(\lambda)$ and (b) the photochemical efficiency or quantum yield (ϕ_{max}, $mmolC^{-1}$ μmol $quanta^{-1}$) that accounts for the efficiency with which absorbed energy is converted into carbon biomass and that we considered not wavelength-dependent in the range of 400–700 nm. The PE curve equation was modified to resolve the visible spectrum as follows:

Table 2
Definitions of Variables and Parameter Values of the Biogeochemical Model

	Description	Value	Unit
Input variables			
$E_0(\lambda)$	Total irradiance at the center of the depth layer	Equation 7	μmol quanta $m^{-2}d^{-1}$
PAR	Photosynthetically active radiation from 400 to 700 nm	Equation 8	μmol quanta m^{-2} d^{-1}
DIN	Dissolved inorganic nitrogen	–	mM
dSi	Dissolved silica	–	mM
dFe	Dissolved iron	–	μM
T	Temperature	–	°K
State variables			
C	Phytoplankton carbon	Equation 18	mmolC m^{-3}
Chla	Phytoplankton photosynthetic pigments	Equation 20	mgChla m^{-3}
D1	Fraction of active reaction centers in the PSII	Equation 25	Relative (0–1)
C^{CDOM}	Colored dissolved organic carbon	Equation 23	mmolC m^{-3}
C^{det}	Carbon component of detritus	Equation 24	mmolC m^{-3}
Intermediate variables			
Tfunc	Arrhenius function for temperature regulation	Hauck et al. (2013)	Relative (0–1)
Nlimit	Nutrient growth-limitation term	Hauck et al. (2013)	Relative (0–1)
P^C_{phot}	Rate of photosynthesis	Equation 19	d^{-1}
P^C_{max}	Maximum rate of photosynthesis	Hauck et al. (2013)	d^{-1}
Gd	Damage rate to D1	Álvarez et al. (2019)	d^{-1}
Rep	Repair rate of D1	Álvarez et al. (2019)	d^{-1}
ϕ_{NP}	Non-photoprotected quantum yield of photosynthesis	Equation 26	mmolC μE^{-1}
Q_e	Antenna-based non-photochemical quenching	Equation 27	Relative (0–1)
a^*_{NP}	Non-photoprotected cellular absorption cross section	Equation 28	m^2 $mgChla^{-1}$
a^N	Carbon-specific nitrogen assimilation rate	Hauck et al. (2013)	mmolN $mmolC^{-1}$ d^{-1}
S_{DOM}	Sources of dissolved organic carbon	Hauck et al. (2013)	mmolC m^{-3} d^{-1}
S_{POC}	Sources of particulate organic carbon	Hauck et al. (2013)	mmolC m^{-3} d^{-1}
Θ	Chla to carbon quota	–	g mol^{-1}
Parameters			
$a^*_{PS}(\lambda)$	Absorption coefficients of photosynthetic pigments	Figures 2a and 2b	m^2 $mgChl^{-1}$
$\bar{a}^*_{PS}$	Average of $a^*_{PS}(\lambda)$ between 400 and 700 nm	Equation 12	m^2 $mgChl^{-1}$
P^C_{ref} (diatoms)	Non-limited maximum rate of photosynthesis	3.5	d^{-1}
P^C_{ref} (small phyto)	Non-limited maximum rate of photosynthesis	3	d^{-1}
ϕ_{max} (diatoms)	Maximum quantum yield of photosynthesis	$3.66 \cdot 10^{-5}$	mmolC μmol $quanta^{-1}$
ϕ_{max} (small phyto)	Maximum quantum yield of photosynthesis	$2.33 \cdot 10^{-5}$	mmolC μmol $quanta^{-1}$
θ^{Chl}_N (diatoms)	Maximum Chla to nitrogen ratio	4.2	gChl $molN^{-1}$
θ^{Chl}_N (small phyto)	Maximum Chla to nitrogen ratio	3.78	gChl $molN^{-1}$
k (diatoms)	Maximum loss rate of Chla	0.15	d^{-1}
k (small phyto)	Maximum loss rate of Chla	0.25	d^{-1}
ρ_{POC}	Degradation rate of detritus	0.15	d^{-1}
f_{CDOM}	Fraction of CDOM in the exuded DOC	0.02	Relative (0–1)
h_{CDOM}	Maximum photobleaching rate of CDOM	0.167	d^{-1}
I_{CDOM}	Threshold for maximum photobleaching rate of CDOM	$5.184 \cdot 10^6$	μmol quanta m^{-2} d^{-1}

Table 2
Continued

	Description	Value	Unit
r_{CDOM}	Remineralization rate of CDOM	0.003	d^{-1}
T_{ref}	Reference temperature	288.15	°K

Note. All parameter values are included in the up-to-date working directory to run the experiments (Data Availability Statement section).

$$P^{C}_{\mathrm{phot}} = P^{C}_{\mathrm{max}} \cdot \left(1 - e^{-\phi_{\mathrm{max}} \cdot \theta \cdot \int_{400}^{700} a^{*}_{\mathrm{PS}}(\lambda) \cdot E_0(\lambda) d\lambda / P^{C}_{\mathrm{max}}}\right) \tag{19}$$

where P^{C}_{max} is the maximum growth rate (d^{-1}), nutrient limited and temperature dependent ($P^{C}_{\mathrm{ref}} \cdot \mathrm{Nlimit} \cdot \mathrm{Tfunc}$). The amount of light absorbed by the phytoplankton was determined by the pigment concentration (θ, chlorophyll to carbon ratio, mgChl mmolC^{-1}) times the integral across wavelengths of 400–700 nm of the product between the available spectral irradiance ($E_0(\lambda)$, Equation 7) and $a^{*}_{\mathrm{PS}}(\lambda)$ (dashed lines in Figures 2a and 2b). The product of light absorbed times ϕ_{max} is equivalent to the product $\alpha\theta\mathrm{PAR}$ (d^{-1}) in the non-spectral version of the model.

The values of both $\overline{a}^{*}_{PS}$ and ϕ_{max} shape the initial slope of the PE curve, α, and hence phytoplankton growth models can be very sensitive to changes in these parameters. To ensure the comparability of our suite of experiments, we selected ϕ_{max} values that once multiplied by $\overline{a}^{*}_{\mathrm{PS}}$, provide the same values for α used in former applications of REcoM2 (Hauck et al., 2013). The small phytoplankton type got a ϕ_{max} of $2.33 \cdot 10^{-5}$ and diatoms of $3.66 \cdot 10^{-5}$ mmolC µmol quanta^{-1}. Although it is commonly assumed a value for ϕ_{max} close to the theoretical maximum of $1.25 \cdot 10^{-4}$ mmol CO_2 fixed per µmol quanta absorbed (Bannister, 1974), experimental data show that ϕ_{max} in natural conditions can be much lower (Myers, 1980; Raven & Crawfurd, 2012), and can range between $1.5 \cdot 10^{-5}$ and $8 \cdot 10^{-5}$ mmolC µmol quanta^{-1} (Arbones et al., 2000). The use in our setup of ϕ_{max} values that kept α invariant, meant that for the same $E_0(\lambda)$, P^{C}_{phot} rates were not affected by changes in $a^{*}_{\mathrm{PS}}(\lambda)$ and additionally that for the same PAR, the P^{C}_{phot} rates of the spectral and non-spectral versions of the model were relatively invariant.

Chlorophyll concentration (Chl-a, mg m^{-3}) is produced at a rate (synthesis) inversely proportional to irradiance and θ to account for the effects of photoacclimation (Geider et al., 1998) and degraded at a variable rate (loss) that depends on photosynthetic activity (Álvarez et al., 2018):

$$\frac{d\boldsymbol{Chla}}{dt} = (\mathrm{synthesis} - \mathrm{loss}) \cdot [\mathrm{Chl}] \tag{20}$$

Both terms were modified to include the spectral composition of light as follows:

$$\mathrm{Synthesis} = a^{N} \cdot \theta^{\mathrm{Chl}}_{N} \cdot \left(\frac{P^{C}_{\mathrm{phot}}}{\phi_{\mathrm{max}} \cdot \theta \cdot \int_{400}^{700} a^{*}_{\mathrm{PS}}(\lambda) \cdot E_0(\lambda) d\lambda}\right) \tag{21}$$

$$\mathrm{Loss} = k \cdot \left(1 - e^{-\phi_{\mathrm{max}} \cdot \theta \cdot \int_{400}^{700} a^{*}_{\mathrm{PS}}(\lambda) \cdot E_0(\lambda) d\lambda / P^{C}_{\mathrm{max}}}\right) \tag{22}$$

where a^{N} was the carbon-specific nitrogen assimilation rate (mmolN mmolC^{-1} d^{-1}, for the exact formulation see Equations 11 and 12 in the supplementary material to Hauck et al., 2013), $\theta^{\mathrm{Chl}}_{N}$ is the maximum nitrogen to Chla quota (Table 2) and k is the maximum degradation rate of Chla (d^{-1}) that was 0.25 for small phytoplankton and 0.15 for diatoms (Table 2).

We included a CDOM tracer in REcoM2 ($\mathrm{C}^{\mathrm{CDOM}}$, mmolC m^{-3}) produced as a fraction (f_{CDOM}) of DOC production (S(DOC), mmolC m^{-3} d^{-1}), that included phytoplankton and zooplankton excretion and detritus dissolution (for the exact formulation see Equation 53 in the supplementary material to Hauck et al., 2013). CDOM was destroyed by remineralization with a long timescale (r_{CDOM}, d^{-1}) and by photo-bleaching at a maximum rate (h_{CDOM}, d^{-1}) when PAR was above I_{CDOM} (5.184 mol quanta m^{-2} d^{-1}) that decreased linearly at lower PAR:

$$\frac{d\mathbf{C}^{\mathbf{CDOM}}}{dt} = f_{\mathrm{CDOM}} \cdot \mathrm{S(DOC)} - (h_{\mathrm{CDOM}} \cdot \min(\mathrm{PAR}/I_{\mathrm{CDOM}}, 1) + r_{\mathrm{CDOM}}) \cdot \left[\mathrm{C}^{\mathrm{CDOM}}\right] \tag{23}$$

NAP (C^{det}, mmolC m^{-3}) is generated by carbon sources ($S(C^{det})$, mmolC m^{-3} d^{-1}) associated with sloppy feeding, aggregation of phytoplankton and mortality of zooplankton (for the exact formulation see Equation 46 in the supplementary material to Hauck et al., 2013). The degradation term consists of a constant degradation rate ρ_{POC} (Table 2) and takes into account a temperature dependency Tfunc, as follows:

$$\frac{d\mathbf{C^{det}}}{dt} = S\left(C^{det}\right) - \rho_{POC} \cdot \mathrm{Tfunc} \cdot \left[C^{det}\right] \tag{24}$$

2.1.4. Phytoplankton Photoprotection: PPC:Chla and Variable $a^*_{PH}(\lambda)$

For each phytoplankton type, the rate of change of the relative number of active reaction centers in the PSII (D1) depends on the rate of inactivation of the D1 proteins (Gd, d^{-1}) that is light dependent, and their rate of repair (Rep, d^{-1}) that is nutrient and temperature dependent. For the exact formulation of Gd and Rep see Equations 1 and 2, respectively, in Álvarez et al. (2019).

$$\frac{d\boldsymbol{D1}}{dt} = (1 - D1) \times \mathrm{Rep} - D1 \times \mathrm{Gd} \tag{25}$$

The fraction of D1 proteins available to photochemistry impacts the photochemical efficiency of PSII (ϕ_{max}). The closure of more than a 25% of reaction centers leads to a decrease of ϕ_{max} to ϕ_{NP}, as follows:

$$\phi_{NP} = \min\left(\frac{\phi_{max}}{0.75} \times D1,\ \phi_{max}\right) \tag{26}$$

The build-up of a proton gradient across the thylakoid triggers the de-epoxidation of xanthophylls and hence an increase in antenna-based non-photochemical quenching (Q_e). ϕ_{NP} is considered as a proxy for Q_e, as depicted in Equation 27, but the impact of a variable pool of xanthophylls is not considered.

$$Q_e = 1 - {}^{\phi_{NP}}/_{\phi_{max}} \tag{27}$$

Q_e decreases the Chla-specific optical absorption cross section of photosynthetic pigments, from $\overline{a}^*_{PS}$ to a^*_{NP}, which represent the decrease in absorption cross sections as observed from saturating to inhibitory light levels.

$$a^*_{NP} = \overline{a}^*_{PS} \times (1 - Q_e) \tag{28}$$

The decrease in both ϕ_{NP} and a^*_{NP} under high light conditions and in the absence of a variable pool of photoprotective pigments (this is indicated by the NP subscript) leads to the photoinhibition of the light harvesting apparatus. The difference between the product of the maximum values of $\overline{a}^*_{PS}$ and ϕ_{max} and the product of a^*_{NP} and ϕ_{NP} accounts for the amount of PPC relative to chlorophyll that each phytoplankton type needs to accumulate to avoid such photoinhibition, as follows:

$$\mathrm{PPC} : \mathrm{Chla} = 1 - \left(\overline{a}^*_{PS} \cdot \phi_{max} / a^*_{NP} \cdot \phi_{NP}\right) \tag{29}$$

In the initial formulation (Álvarez et al., 2019), $\overline{a}^*_{PS}$ is set to 0.007 m^2 $mgChla^{-1}$ for both phytoplankton types and ϕ_{max} is set to $5.00 \cdot 10^{-5}$ and $6.75 \cdot 10^{-5}$ mmolC µmol $quanta^{-1}$ for small phytoplankton and diatoms, respectively. In the present work, the values of $\overline{a}^*_{PS}$ were obtained from the $a^*_{PS}(\lambda)$ curves (Equation 12) and were 0.0143 and 0.0115 m^2 $mgChla^{-1}$ for small phytoplankton and diatoms, respectively. ϕ_{max} was set to $2.33 \cdot 10^{-5}$ and $3.66 \cdot 10^{-5}$ mmolC µmol $quanta^{-1}$ for small phytoplankton and diatoms, respectively (Table 2). During the sensitivity analysis of model results to the choice of constant $a^*_{PH}(\lambda)$ and $a^*_{PS}(\lambda)$ spectra (see Section 2.2 and Text S2 in Supporting Information S1), we included $a^*_{PS}(\lambda)$ spectra scaled to match $\overline{a}^*_{PS}$ in the range of values reported in literature, from 0.005 to 0.025 m^2 $mgChla^{-1}$ (Kromkamp et al., 2001; Oliver & Ganf, 1988) to confirm that variations in $\overline{a}^*_{PS}$ and ϕ_{max} did not influence significantly the simulations of PPC:TChla.

To simulate the impact of a variable PPC:TChla ratio on the spectral shape of $a^*_{PH}(\lambda)$ we used empirical relationships obtained from the analysis of the NASA bio-Optical Marine Algorithm Dataset (NOMAD v2; Werdell and Bailey (2005)). NOMAD is a global, high-quality, publicly available (NOBPG, 2018) in situ observation data set for algorithm development and ocean-color satellite validation. It covers many bio-optical variables and includes both open ocean and coastal data sets of collocated optical and High-Performance Liquid Chromatography

(HPLC)-derived pigments. $a_{\mathrm{PH}}(\lambda)$ was derived by subtracting detrital absorption from particulate absorption and $a^*_{\mathrm{PH}}(\lambda)$ by dividing with TChla. PPC:TChla was computed as the sum of Allo, Lut, Viola, Zea, DD, DT, and Caro, divided by TChla. The fraction of diatoms in the sample (fDiatoms) was computed as 1.41xFuco/DP being DP equal to 1.41Fuco + 1.41Perid + 1.27Hex + 0.6Allo + 0.35But + 1.01Chlb + 0.86Zea (Uitz et al., 2006). A total of 268 samples were found to contain simultaneously $a^*_{\mathrm{PH}}(\lambda)$, PPC:TChla and fDiatoms, and were divided into two parts based on fDiatoms, 231 samples with less than 50% of diatoms and 75 samples with more than 50% of diatoms.

To describe changes in the shape of $a^*_{\mathrm{PH}}(\lambda)$ based on the content of PPC:TChla, we collected several metrics from literature, including band ratios and spectral slopes and prioritizing those which have been already correlated to some proportion between photosynthetic and non-photosynthetic pigments (e.g., Eisner et al., 2003; Ferreira et al., 2017; Hirata et al., 2008). The metric that better correlated to PPC:TChla content was the spectral slope of $a^*_{\mathrm{PH}}(\lambda)$ between 489 and 532 nm (Eisner et al., 2003) (Figures 3a and 3b). We assumed that the peak of $a^*_{\mathrm{PH}}(\lambda)$ in the red part of the spectrum was entirely due to photosynthetic pigments. Hence, for wavelengths longer than 532 nm, $a^*_{\mathrm{PH}}(532-700)$ was equal to $a^*_{\mathrm{PS}}(532-700)$. For any given PPC:TChla content the spectral slope derived from the empirical relationships for small phytoplankton (Figure 3a) and diatoms (Figure 3b) was used to reconstruct $a^*_{PH}(489-532)$. For wavelengths shorter than 489 nm, $a^*_{\mathrm{PH}}(400-489)$ was $a^*_{PS}(400-489) + [a^*_{PH}(489) - a^*_{\mathrm{PS}}(489)]$ (Figures 3c and 3d).

2.2. Model Simulations and Experiments

Three-dimensional (3D) simulations were used to investigate the impact of variable $a^*_{\mathrm{PH}}(\lambda)$ in the global variability of phytoplankton absorption coefficients in a complex real system. In the 3D configuration for the global ocean, temperature, dissolved nutrients (DIN, Si, and Fe) and all other BGC model variables in REcoM2, were advected and mixed by the ocean circulation derived from the MIT global circulation model (MITgcm; Campin et al., 2021; J. Marshall et al., 1997). We employed a nearly global model configuration from 80°S to 80°N on a horizontal 2° × 2° grid in Northern hemisphere and 2° × 2° times the cosine of the latitude in the Southern hemisphere, with 30 depth layers (0–5700 m).

Forcing fluxes at surface included daily 10 m winds, 2 m air temperature, humidity and sea level pressure, and monthly precipitation and runoff fields from the CORE data set (Large & Yeager, 2009). Monthly climatological dust deposition field was calculated from 1979 to 2010 data (Mahowald et al., 2003). Spectral plane downwelling irradiance just below the surface of the ocean was obtained from the data product derived from the OASIM Model (Gregg & Casey, 2009) and available as monthly means in the NASA Global Modeling and Assimilation Office ftp (NOBM, 2019). We forced the model with a monthly climatology (that averaged years 2008–2012) of both the direct $[E^{\mathrm{below}}_{d0}(\lambda)]$ and diffuse $[E^{\mathrm{below}}_{s0}(\lambda)]$ components in 13 wavebands (W m^{-2}) from 400 to 700 nm, at 1° × 1° spatial resolution and interpolated on-the-fly to the model grid.

The model was initialized with the January climatological fields of temperature, salinity, nitrate and silicate from the World Ocean Atlas 2009 (Antonov et al., 2010; Garcia et al., 2010; Locarnini et al., 2010) and with mean alkalinity and preindustrial dissolved inorganic carbon fields from GLODAP (R. M. Key et al., 2004). The initial field for dissolved Fe was obtained from PISCES output (Aumont et al., 2003), with values south of 45°S set to average Southern Ocean vertical profiles from Tagliabue et al. (2012). The model was spun up for four years and analyzed for the next fifth year in a 10-daily temporal resolution.

We conducted three 3D experiments:

EXP-S: Sensitivity of model results to the choice of constant $a^*_{\mathrm{PH}}(\lambda)$ and $a^*_{\mathrm{PS}}(\lambda)$ spectra: we run 20 simulations with $a^*_{\mathrm{PH}}(\lambda)$ and $a^*_{\mathrm{PS}}(\lambda)$ spectra scaled to match mean values of absorption coefficients ($\overline{a}^*_{\mathrm{PH}}$ and $\overline{a}^*_{\mathrm{PS}}$) reported in literature. By comparing model output to satellite and in situ observations of apparent and IOPs and BGC products, we assessed the variation in performance metrics. The complete results of EXP-S are reported in Text S2 in Supporting Information S1.

EXP-noPPC: Constant $a^*_{\mathrm{PH}}(\lambda)$: we run one simulation with constant $a^*_{\mathrm{PH}}(\lambda)$ and $a^*_{\mathrm{PS}}(\lambda)$ spectra computed from spectra collected from literature (Section 2.1.2).

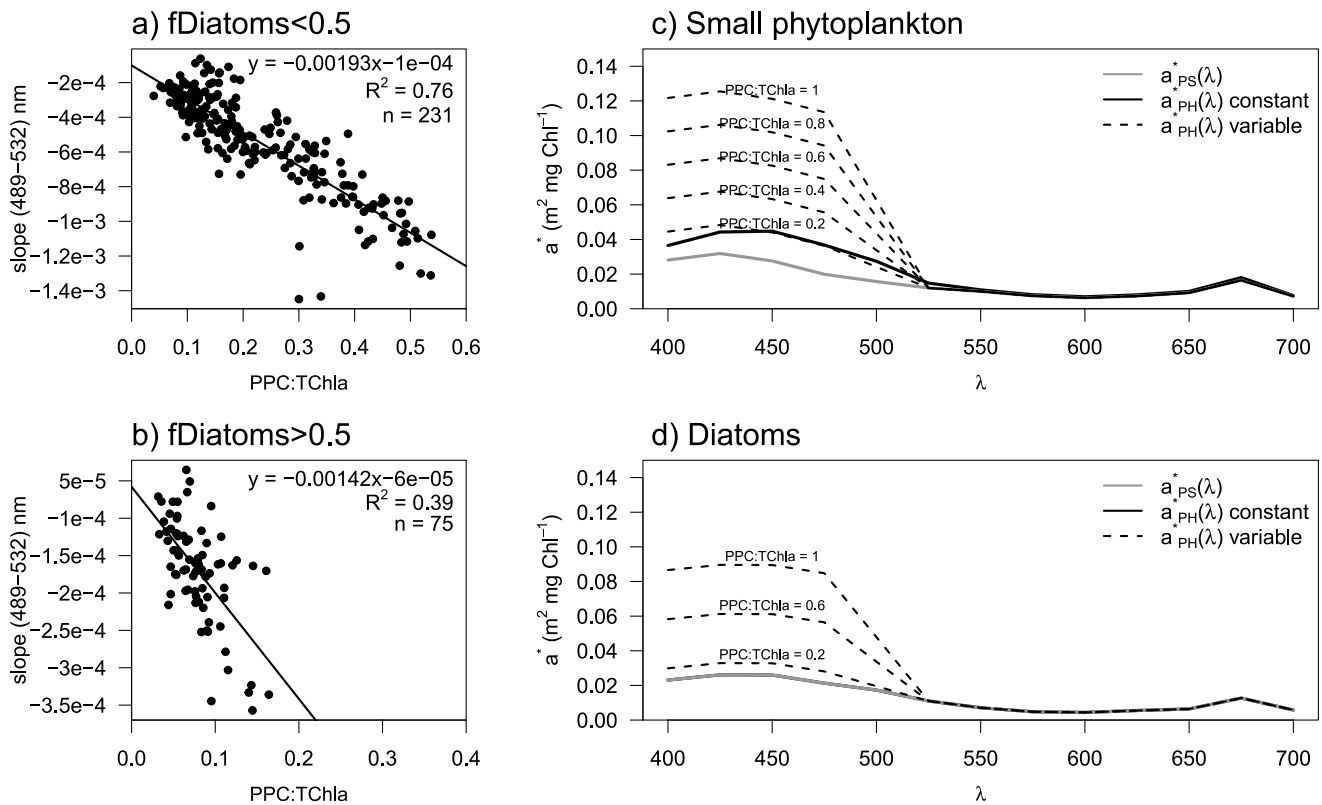

Figure 3. Reconstruction of $a^*_{\mathrm{PH}}(\lambda)$ from PPC:TChla ratios: spectral slope of $a^*_{\mathrm{PH}}(\lambda)$ between 489 and 532 nm as a function of PPC:TChla for samples in the NASA bio-Optical Marine Algorithm Dataset data set with (a) less than 50% of diatoms and (b) more than 50% of diatoms; $a^*_{\mathrm{PS}}(\lambda)$, constant $a^*_{PH}(\lambda)$ derived from literature (Section 2.1.2) and variable $a^*_{\mathrm{PH}}(\lambda)$ as a function of the modeled PPC:TChla ratios for (c) small phytoplankton using the empirical relationship in panel (a) and (d) diatoms using the empirical relationship in panel (b).

EXP-PPC: Variable $a^*_{\mathrm{PH}}(\lambda)$: we run one simulation with constant $a^*_{\mathrm{PS}}(\lambda)$ and variable $a^*_{\mathrm{PH}}(\lambda)$ based on the ratio PPC:TChla simulated for each phytoplankton type (Section 2.1.4).

For each experiment, each variable in the model output, including biological and physical, was averaged to a horizontal 2° × 2° grid and as monthly climatology. This resulted in an 4D array per variable that has a common spatial and temporal resolution to be compared to observations (180° longitude × 90° latitude × 70 depth × 12 time).

3. Satellite and Field Observations

Monthly composites of satellite retrieved $R_{\mathrm{RS}}(\lambda)$, IOPs and TChla were obtained from the Ocean Color Climate Change Initiative data set v4.2 by the European Space Agency (Sathyendranath et al., 2019) that processes extensive ocean color data sets from ESA and NASA missions. $R_{\mathrm{RS}}(\lambda)$ is the primary product retrieved by satellites after atmospheric correction (Jackson et al., 2020). $R_{\mathrm{RS}}(\lambda)$ values from different sensors are shifted to the standard SeaWiFS wavelengths (412, 443, 490, 510, 555, and 670 nm) with a bandwidth of 20 nm. The values for IOPs, that included phytoplankton absorption coefficients ($a_{\mathrm{PH}}(\lambda)$, m^{-1}) and absorption coefficients due to detrital and dissolved matter ($a_{\mathrm{DG}}(\lambda)$, m^{-1}), are computed for the same standard wavelengths, from daily, merged $R_{\mathrm{RS}}(\lambda)$ values using the algorithm in Lee et al. (2009). Total absorption coefficients ($a_{\mathrm{TOT}}(\lambda)$, m^{-1}) are the sum of absorption coefficients of pure water ($a_W(\lambda)$) obtained from Pope and Fry (1997), $a_{\mathrm{PH}}(\lambda)$, and $a_{\mathrm{DG}}(\lambda)$. TChla concentration (TChla, mg m^{-3}) is generated from $R_{\mathrm{RS}}(\lambda)$ by using a blended combination of the band algorithms OC3, OCI (OC4 + CI) and OC5 (O'Reilly & Werdell, 2019), depending on the water type present (Jackson et al., 2017; Moore et al., 2009). For all variables, monthly composites from January 2012 to December 2018 were used to create climatological averages at 2° × 2° spatial resolution to match model output resolution.

We collected in situ observations of $R_{RS}(\lambda)$ and IOPs from published compilations (Casey et al., 2020; Chase et al., 2017; Valente et al., 2019; Werdell & Bailey, 2005), the Australian-waters Earth Observation Phytoplankton-type products database (CSIRO, 2020) and from a set of expeditions available at Pangaea (Bracher). Some of the IOP data sets in Bracher have been submitted to Pangaea in the framework of this study (Bracher & Liu, 2021a, 2021b; Bracher & Taylor, 2021a, 2021b, 2021c, 2021d; Bracher, Taylor, & Cheah, 2021a, 2021b; Bracher & Wiegmann, 2021; Bracher et al., 2021e, 2021f, 2021g, 2021h, 2021o, 2021p). All methods for these data have been published before and are described in brief in the cruise specific data publication, except for the $a_{CDOM}(\lambda)$ data (Bracher et al., 2021a, 2021b, 2021c, 2021d, 2021m, 2021n, 2021i, 2021j, 2021k, 2021l). For these data, the method is described in Text S1.1 in Supporting Information S1 (Lefering et al., 2017; Röttgers et al., 2014). All data sets, their available data types and sources are summarized in Table 3. The values for IOPs included absorption coefficients for CDOM ($a_{CDOM}(\lambda)$, m^{-1}), NAP ($a_{NAP}(\lambda)$, m^{-1}), phytoplankton ($a_{PH}(\lambda)$, m^{-1}) and all particles ($a_P(\lambda)$, m^{-1}). Data were discarded if they (a) had missing date, depth or geographic coordinate fields, (b) were flagged in the original data set, or (c) were out of the range [0–0.15] sr^{-1} for $R_{RS}(\lambda)$ and out of the range [0.0001–10] m^{-1} for IOPs. $R_{RS}(\lambda)$ and IOPs were reported originally at different spectral resolutions, ranging from 1 to 5 nm steps. We averaged all variables in the 25 nm-wide wavebands from 400 to 700 nm used in the model and created monthly climatologies with $2° \times 2°$ spatial resolution and at the 70 depth layers of the model for the variables that were available in the water column.

Pigment concentrations of TChla and PPC were obtained from published HPLC data sets (Peloquin et al., 2013), HPLC data in the AEsOP-CSIRO database (CSIRO, 2020) and HPLC data from a set of cruises available at Pangaea (Bracher). Bracher and Wiegmann (2022) is a new data set incorporated in this study and its method is described in Text S1.2 in Supporting Information S1 (Bidigare, 1991; Hoffmann et al., 2006; Jeffrey et al., 1997; JGOFS, 1994; Barlow et al., 1997; Taylor et al., 2011a). All data sets that provided HPLC data are listed in Table 3. The pigment compilation is in part the same used in Álvarez et al. (2019) and all the details about the quality control of these data can be found in that publication. Briefly, following Aiken et al. (2009), we flagged: (a) samples in which TChla was zero or less, (b) samples in which fewer than four non-zero accessory pigments were reported; (c) samples that fell outside the range of two standard deviations of the regression line of the log-linear relationship between TChla and total accessory pigment concentration; (d) and the entire campaign's samples if more than 35% of samples from a given field campaign was flagged during the third step. If Chla derivatives are reported separately, TChla encompassed them all, and PPC consisted of Allo, Lut, Viola, Zea, DD, DT, and Caro. For TChla and the ratio PPC:TChla we created monthly climatologies with $2° \times 2°$ spatial resolution and at the 70 depth layers of the model.

To test the consistency of model results, we considered satellite retrievals and in situ observations of $R_{RS}(\lambda)$, IOPs and BGC products. Model output at ocean surface of TChla, $R_{RS}(\lambda)$ at 400, 450, 475, 500, 550, and 675 nm, $a_{PH}(450)$, $a_{DG}(450)$ computed as the sum of $a_{CDOM}(450)$ and $a_{NAP}(450)$, and $a_{TOT}(450)$ computed as the sum of $a_{PH}(450)$, $a_{DG}(450)$ and $a_W(450)$ were compared to satellite observations of TChla, $R_{RS}(\lambda)$ at 412, 443, 490, 510, 555, and 670 nm, $a_{PH}(443)$, $a_{DG}(443)$and $a_{TOT}(443)$. For comparison to in situ observations the wavebands were equivalent to model output, $a_{CDOM}(450)$ and $a_{NAP}(450)$ were compared disaggregated and $a_P(450)$ was considered the sum of $a_{PH}(450)$ and $a_{NAP}(450)$. In situ observations included also PPC:TChla and hence the ratios were compared to model output of community aggregated PPC:TChla. Comparison metrics included Pearson's determination coefficient (R), root mean square error (RMSE) and average error (Bias), all computed following Stow et al. (2009).

The data sets by Valente et al. (2019a) and Bracher provided already collocated IOPs and TChla data, and hence permitted to compute chl-specific $a^*_{PH}(\lambda)$. Valente et al. (2019a) compilation included the NOMAD v2 data set that we used to correlate the spectral shape of $a^*_{PH}(\lambda)$ to the content in PPC:Chla (Section 2.1.4) and also $a_{PH}(\lambda)$ values at surface from cruises also included in the Bracher compilation. We excluded from Valente et al. (2019a), all NOMAD samples and Bracher cruises (identified as "nomad" or "awi" in the field "Comment (algal pigments ac data set)"). We refer to this reduced version of the Valente et al. (2019a) compilation as Valente. Valente and Bracher data sets were used to compare observed $a^*_{PH}(\lambda)$ to model results. Note that the Valente compilation only included surface values and the Bracher compilation included samples from surface down to 200 m depth.

Table 3
List of Data Sets With In Situ Observations of Remote Sensing Reflectance (R_{RS}), Absorption Coefficients for Total Particles (a_P), Colored Dissolved Organic Matter (CDOM; a_{CDOM}), Non-Algal or Detrital Material (a_{NAP}) and Phytoplankton (a_{PH}), Chl-Specific Absorption Coefficients of Phytoplankton (a^*_{PH}), and High-Performance Liquid Chromatography (HPLC) Pigments

Data set	Source	$R_{RS}(\lambda)$	$a_P(\lambda)$	$a_{CDOM}(\lambda)$	$a_{NAP}(\lambda)$	$a_{PH}(\lambda)$	$a^*_{PH}(\lambda)$	HPLC
Chase et al. (2017)								
AE1319	Cetinić (2014)	x						
NH1418	Cetinić (2014)	x						
Casey et al. (2020)								
SABOR	Behrenfeld et al. (2014) and Chase et al. (2017)	x						
TARA Oceans	Chase et al. (2017)	x						
TARA Arctic	Matsuoka et al. (2017) and Slade et al. (2010)	x						
BIOSOPE	Bricaud et al. (2010), Miller et al. (2002), and Stramski et al. (2008)	x	x	x	x	x		
ANT26	Stramski et al. (2008)	x	x	x	x	x		
Compass Buoy	Craig et al. (2012)	x	x		x	x		
Valente et al. (2019)								
All cruises	Valente et al. (2019)	x		x		x*	x*	x**
NOMAD v2.0	NOBPG (2018) and Werdell and Bailey (2005)					x	x	x
Bracher								
ANT23.1 (PS69)	Bracher et al. (2015)							x
ANT24.1 (PS71.1)	Bracher (2015b) and Bracher and Taylor (2019)		x					x
ANT24.4 (PS71.4)	Bracher (2015c) and Bracher and Taylor (2021b)		x					x
ANT25.1 (PS73)	Taylor et al. (2011b, 2011c, 2011d)		x			x	x	x
ANT26.3 (PS75)	Peeken and Nachtigall (2014a, 2014b) and Soppa et al. (2013a, 2013b)		x			x	x	x**
ANT26.4 (PS75)	Bracher (2015d) and Bracher and Taylor (2021c, 2021d)		x			x	x	x
ANT27.2 (PS77)	Bracher (2015e)							x
ARK26.3 (PS78)	Bracher et al. (2018), Gonçalves-Araujo et al. (2018), and Peeken and Murawski (2016)	x				x	x	x**
ANT28.3 (PS79)	Bracher (2014a) and Soppa et al. (2013c, 2013d)		x			x	x	x
PS93.2	Liu et al. (2018a, 2019a, 2019c), and Wiegmann et al. (2019)		x		x	x	x	x
PS99	Bracher et al. (2021a, 2021b) and Liu et al. (2018b, 2019d, 2019f, 2019g)		x	x	x	x	x	x
PS103	Bracher (2019b), Bracher and Liu (2021a, 2021b), and Bracher et al. (2021c, 2021d)			x	x	x	x	x
PS107	Liu et al. (2019b, 2019e, 2019h)		x		x	x	x	x
PS113	Bracher et al. (2020) and Bracher et al. (2021m, 2021n, 2021o, 2021p)			x	x	x	x	x
PS121	Bracher and Wiegmann (2022) and Bracher et al. (2021f, 2021h, 2021i, 2021j)			x	x	x	x	x
HE462	Bracher and Wiegmann (2019) and Bracher et al. (2021e, 2021g, 2021k, 2021l)			x	x	x	x	x
SO202	Taylor and Bracher (2012a, 2012b, 2017)		x			x	x	x
SO218	Bracher (2014b) and Bracher, Taylor, and Cheah (2021a, 2021b)		x			x	x	x
SO234/235	Bracher et al. (2019) and Bracher and Wiegmann (2021)		x					x
SO243 (ASTRA)	Bracher (2019a)							x
MSM09	Bracher and Taylor (2017, 2021a)		x					x
MSM18	Bracher (2015a)							x
AesOP-CSIRO								
Beagle (x5)	CSIRO (2020)		x					x

Table 3
Continued

Data set	Source	$R_{RS}(\lambda)$	$a_P(\lambda)$	$a_{CDOM}(\lambda)$	$a_{NAP}(\lambda)$	$a_{PH}(\lambda)$	$a^*_{PH}(\lambda)$	HPLC
BROKEWEST	CSIRO (2020)		x		x	x		x
Bunbury	CSIRO (2020)			x	x	x		
DTree (x2)	CSIRO (2020)			x	x	x		
HImay04	CSIRO (2020)			x	x	x		
HP (x3)	CSIRO (2020)			x	x	x		
LB3172	CSIRO (2020)			x	x	x		
MB (x2)	CSIRO (2020)			x	x	x		
Tas (x2)	CSIRO (2020)			x	x	x		
FR/FRE	CSIRO (2020)			x	x	x		x
GBR (5)	CSIRO (2020)			x	x	x		x
SS (x6)	CSIRO (2020)			x	x	x		x
CLIVAR	CSIRO (2020)				x	x		x
NWS	CSIRO (2020)				x	x		x
SOOP	CSIRO (2020)							x
Sniper (x4)	CSIRO (2020)							x
TIP2000	CSIRO (2020)							x
MAREDAT								
MAREDAT pigments	Peloquin et al. (2013)							x

Note. In data sets marked with (*), total (a_{PH}) and chl-specific absorption coefficients of phytoplankton (a^*_{PH}) do not include cruises marked as "nomad" or "awi." From HPLC data sets marked with (**), only TChla concentrations are considered in this work.

4. Results

4.1. Sensitivity of Model Output to the Constant $a^*_{PH}(\lambda)$ Spectra

Before evaluating the impact of variable $a^*_{PH}(\lambda)$ spectra on the simulation of $a_{PH}(\lambda)$, we first evaluated whether the constant $a^*_{PH}(\lambda)$ setup described in Section 2.1.2 was the most representative for the global ocean. Under EXP-S we performed a series of 20 simulations with a set of constant $a^*_{PH}(\lambda)$ and $a^*_{PS}(\lambda)$ spectra. A complete analysis about the sensitivity of model results in terms of TChla, PPC:TChla, $R_{RS}(\lambda)$ and IOPs to the choice of constant $a^*_{PH}(\lambda)$ spectra is available as Text S2 in Supporting Information S1. In summary, results showed that (a) model simulations of TChla and PPC:TChla ratios kept the accuracy with changing $a^*_{PS}(\lambda)$ spectra and (b) that the constant $a^*_{PH}(\lambda)$ spectra gathered from literature and $a^*_{PS}(\lambda)$ spectra reconstructed from them were among the most representative for the global ocean.

4.2. Spatial Distribution of $a_{PH}(\lambda)$

The annual mean of $a_{PH}(\lambda)$ at 450 nm (m^{-1}) in the surface of the global ocean follows the distribution of phytoplankton chlorophyll (Figure 4). $a_{PH}(443)$ from satellite shows lower values, below 0.01 m^{-1}, in the subtropical gyres followed by the equatorial area. Larger values, up to 0.07 m^{-1}, are observed in subpolar and polar areas (Figure 4a). A similar pattern is observed in $a_{PH}(450)$ from in situ measurements, despite the relative scarcity of observations (Figure 4b). Model simulations of $a_{PH}(450)$ showed the same latitudinal pattern, but the maximum values are larger in the constant $a^*_{PH}(\lambda)$ setup (EXP-noPPC, Figure 4c) compared to the variable $a^*_{PH}(\lambda)$ setup (EXP-PPC, Figure 4d). EXP-PPC is in closer agreement with observations for latitudes poleward of 40°. It is worth noting the band mismatch between the satellite product retrieved at 443 (±10) nm compared to in situ observations and model simulations that represent the 450 (±12.5) nm band. Model output and in situ observations include $a_{PH}(\lambda)$ values between 437.5 and 462.5 nm and the satellite product between 433 and 453 nm, and they overlap in the lower portion of the model waveband (from 437.5 to 453 nm).

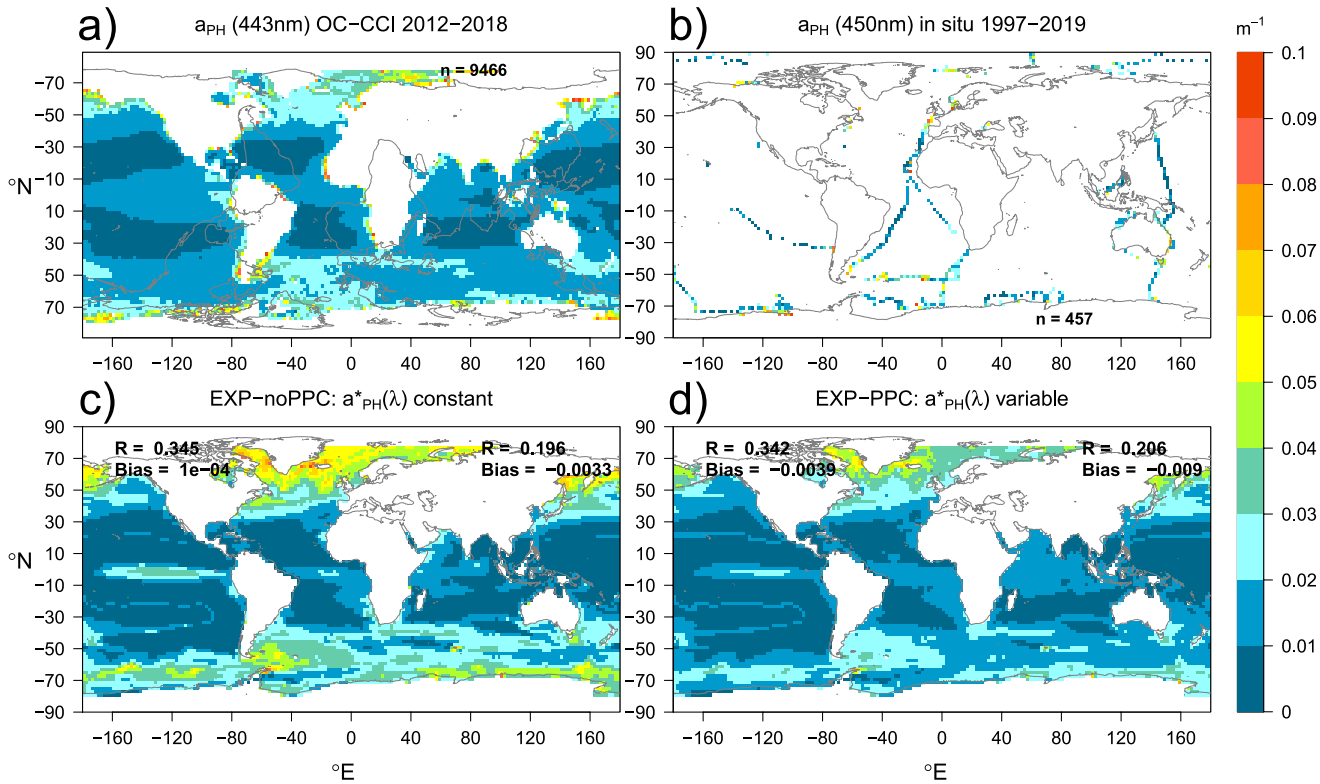

Figure 4. Surface distribution of annual average $a_{\mathrm{PH}}(\lambda)$ (m^{-1}) from (a) satellite retrievals (years 2012–2018) at 443 nm, (b) in situ observations ($n = 457$, years 1997–2019) in the 450 nm waveband, and model simulations in the 450 nm waveband in (c) EXP-noPPC with constant $a^*_{PH}(\lambda)$ and in panel (d) EXP-PPC with variable $a^*_{\mathrm{PH}}(\lambda)$. Pearson's correlation coefficient (R) and bias for the comparison of modeled $a_{PH}(\lambda)$ to the satellite product in panel (a) and in situ observations in panel (b) are included in the top left and top right corner of panels (c and d), respectively.

Similar to the ocean surface, the distribution of $a_{\mathrm{PH}}(450)$ within the water column follows the distribution of TChla (Figure 5). TChla distribution is fairly similar between EXP-noPPC and EXP-PPC, although slightly higher in EXP-PPC (Figure 5a versus Figure 5b) that also translates in a slightly larger annual-integrated net primary production (NPP) and exported production (EXP) in EXP-PPC. Inversely, $a_{\mathrm{PH}}(450)$ values simulated in EXP-PPC are lower than in EXP-noPPC (Figure 5c versus Figure 5d), indicating lower absorption per unit of Chla concentration in the water. The IOPs of other OAC, $a_{\mathrm{CDOM}}(450)$ (Figure 5e versus Figure 5f) and $a_{\mathrm{NAP}}(450)$ (Figure 5g versus Figure 5h) were very similar between EXP-noPPC and EXP-PPC. When comparing the contribution of phytoplankton and other OAC to total absorption, phytoplankton is always the largest contributor to total absorption at the depth of the chlorophyll maximum in EXP-noPPC (Figure 5i). In EXP-PPC, on the other hand, other constituents substituted phytoplankton as the largest contributor to total absorption above the euphotic depth of the subtropical gyres (15°–35° latitude), namely $a_{\mathrm{CDOM}}(450)$ close to the chlorophyll maximum and $a_W(450)$ above 75 m (Figure 5j).

The latitudinal gradients of $a_{\mathrm{PH}}(450)$ in the ocean surface show more clearly that EXP-PPC simulated a smaller range of variability for $a_{\mathrm{PH}}(\lambda)$ than EXP-noPPC for the same TChla concentrations (Figure 6). In EXP-noPPC, the modeled gradient of increasing $a_{\mathrm{PH}}(450)$ from latitude 25° to 65°, both south and northward, is much steeper than observed from satellite $a_{\mathrm{PH}}(443)$ (Figure 6a). The difference between the subtropical minimum and the equatorial local peak was also larger in EXP-noPPC than in EXP-PPC. In EXP-PPC, with variable $a^*_{\mathrm{PH}}(\lambda)$, the difference in $a_{\mathrm{PH}}(450)$ between low-absorbing regions (tropical) and high absorbing regions (subpolar) is smaller than in EXP-noPPC. Hence, model results with variable $a^*_{\mathrm{PH}}(\lambda)$ show better agreement with the satellite product (Figure 6b). The range of $a_{\mathrm{PH}}(450)$ at each latitude from in situ observations was only showed if there are at least three measurements for each latitude grid cell (2°). In the tropical and sub-tropical ocean, in situ observations are overall larger than model and satellite counterparts. Larger inconsistencies among the three types of data sets appear in the polar regions. Southward of the polar circle, model results show a decrease in absorption not

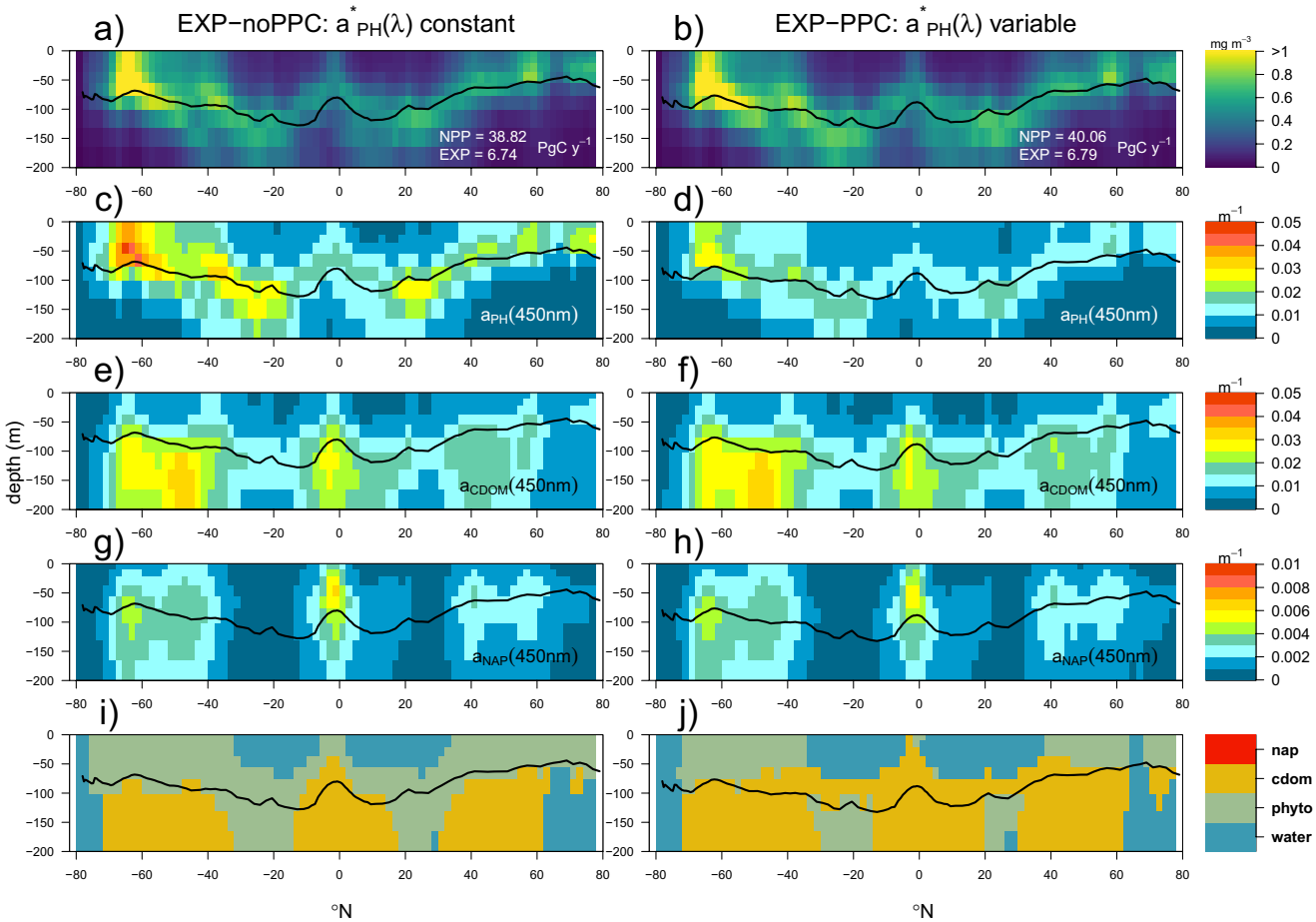

Figure 5. Longitude-averaged depth profiles from model simulations with constant $a^*_{\mathrm{PH}}(\lambda)$ (EXP-noPPC, left panels) and with variable $a^*_{\mathrm{PH}}(\lambda)$ (EXP-PPC, right panels) of (a and b) TChl, and absorption (m^{-1}) at 450 nm by OAC, (c and d) $a_{\mathrm{PH}}(450)$, (e and f) $a_{\mathrm{CDOM}}(450)$, and (g and h) $a_{\mathrm{NAP}}(450)$. (i and j) The optically active constituent, including water, that contributed most to total absorption in both model setups. Black line shows the depth of the euphotic zone (z_{EU}), defined as the depth where 1% of surface PAR is met.

observed in satellite retrievals but observed in situ (Figure 6b). Poleward of 80°N in situ observations show a decrease in $a_{\mathrm{PH}}(450)$ but our model did not cover such latitudes.

Results shown in Figures 4–6 indicate that the range of $a_{\mathrm{PH}}(450)$ values simulated with variable $a^*_{\mathrm{PH}}(\lambda)$ is narrower than this simulated with constant $a^*_{PH}(\lambda)$. This result is consistent for the rest of the wavebands equal or shorter than 500 nm. Figure 7 shows simulated $a_{\mathrm{PH}}(\lambda)$ at 400, 450, 475, and 500 nm compared to in situ observations in the same wavebands and satellite retrievals in comparable wavelengths (412, 443, 490, and 510 nm, respectively). Log-transformed simulated versus observed $a_{\mathrm{PH}}(\lambda)$ values spread around the 1:1 line, but, for all wavelengths, EXP-PPC decreased the spread of simulated $a_{\mathrm{PH}}(\lambda)$ with respect to EXP-noPPC (right versus left panels in Figure 7) when compared both to satellite and in situ data sets. For all wavebands and for both set of observations (in situ in light gray and satellite in dark gray in Figure 7), Pearson's correlation coefficients (R) are higher, and RMSEs lower in EXP-PPC than in EXP-noPPC. The density distribution of $a_{\mathrm{PH}}(\lambda)$ obtained from observations (horizontal histograms in Figure 7) for any of these wavelengths is quasi-unimodal and so it is in the model simulations in EXP-PPC with variable $a^*_{\mathrm{PH}}(\lambda)$ (vertical histograms in the right panels of Figure 7). On the contrary, results of EXP-noPPC with constant $a^*_{\mathrm{PH}}(\lambda)$ show a bimodal distribution of $a_{\mathrm{PH}}(\lambda)$ that covers more than two orders of magnitude in $a_{\mathrm{PH}}(\lambda)$ (vertical histograms in the left panels of Figure 7). For all the wavebands other than 450 nm, the band retrieved by satellites overlaps in the upper portion of the waveband of in situ observations and model simulations. The 412 (±10) nm versus 400 (+12.5) comparison overlaps from 402 to 412.5 nm, the 490 (±10) nm versus 475 (±12.5) comparison overlaps from 480 to 487.5 nm and the 510 (±10) nm versus 500 (±12.5) comparison overlaps from 500 to 512.5 nm.

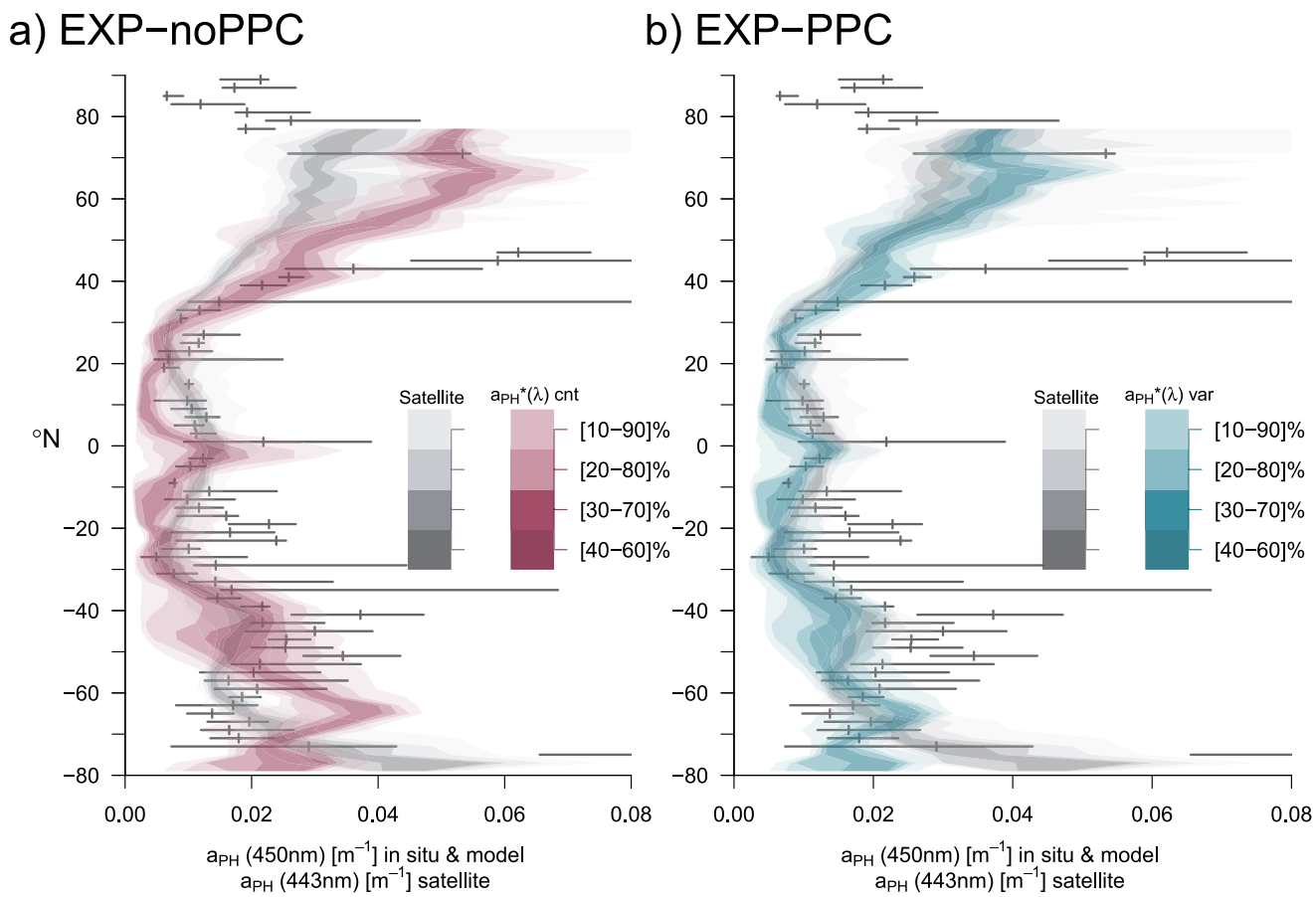

Figure 6. Latitudinal gradient of $a_{\mathrm{PH}}(\lambda)$ (m^{-1}) at ocean surface from model simulations in the 450 nm waveband (colored areas) compared to in situ observations for the same waveband (box and whiskers) and at 443 nm from satellite retrievals (gray areas) in (a) EXP-noPPC with constant $a^*_{PH}(\lambda)$ and in (b) EXP-PPC with variable $a^*_{\mathrm{PH}}(\lambda)$. Color intensity indicates the percentile of values at each latitude for modeled and satellite data, box and whiskers indicate the median and the interquartile range of observed in situ values.

4.3. Bio-Optical Relationships Between $a_{\mathrm{PH}}(450)$ and TChla

The bio-optical relationship between $a_{\mathrm{PH}}(450)$ and the concentration of TChla in the water observed in nature is not isometric. When represented on a decimal log-log graph, the slope of the power law fit is smaller than one, ranging from 0.651 to 0.728 in literature (Bricaud et al., 1995, 2004), 0.678 in the Valente data set ($R^2 = 0.67$, p-value <0.005) and 0.691 in the Bracher data set ($R^2 = 0.80$, p-value<0.005) (Figure 8a). This is explained by the differential contribution of small versus large phytoplankton with increasing phytoplankton biomass and the covariations of accessory pigments with TChla (Bricaud & Morel, 1986). There is a remarkable scatter around the fit, which means that for a given TChla concentration the value of $a_{\mathrm{PH}}(450)$ is highly variable, which is explained by the interplay of changes in community size structure and pigment composition (Bricaud et al., 2004).

To reproduce such bio-optical relationship for our modeled $a_{\mathrm{PH}}(450)$ versus TChla, we averaged $a_{\mathrm{PH}}(450)$ values in bins of log-transformed TChla and fitted a type-II least squares regression model (Legendre, 2018; Legendre & Legendre, 1998). In EXP-noPPC, the slope of the power law relating $a_{\mathrm{PH}}(450)$ and TChla was 0.911 ($R^2 = 0.99$ p-value <0.005) with a limited range of variability around the fit (Figure 8b). This shows that this model setup has little ability to simulate $a^*_{\mathrm{PH}}(\lambda)$ variability, only through changes in the relative contribution of the two phytoplankton types with constant $a^*_{\mathrm{PH}}(\lambda)$ coefficients. In EXP-PPC, the slope of the power law was 0.709 ($R^2 = 0.99$, p-value <0.005) with a larger range of variability around the fit (Figure 8c). This shows that this model setup primarily modifies the light absorption per unit of chlorophyll concentration in the water, and it can simulate higher $a^*_{\mathrm{PH}}(\lambda)$ coefficients when total chlorophyll concentration is lower and vice versa.

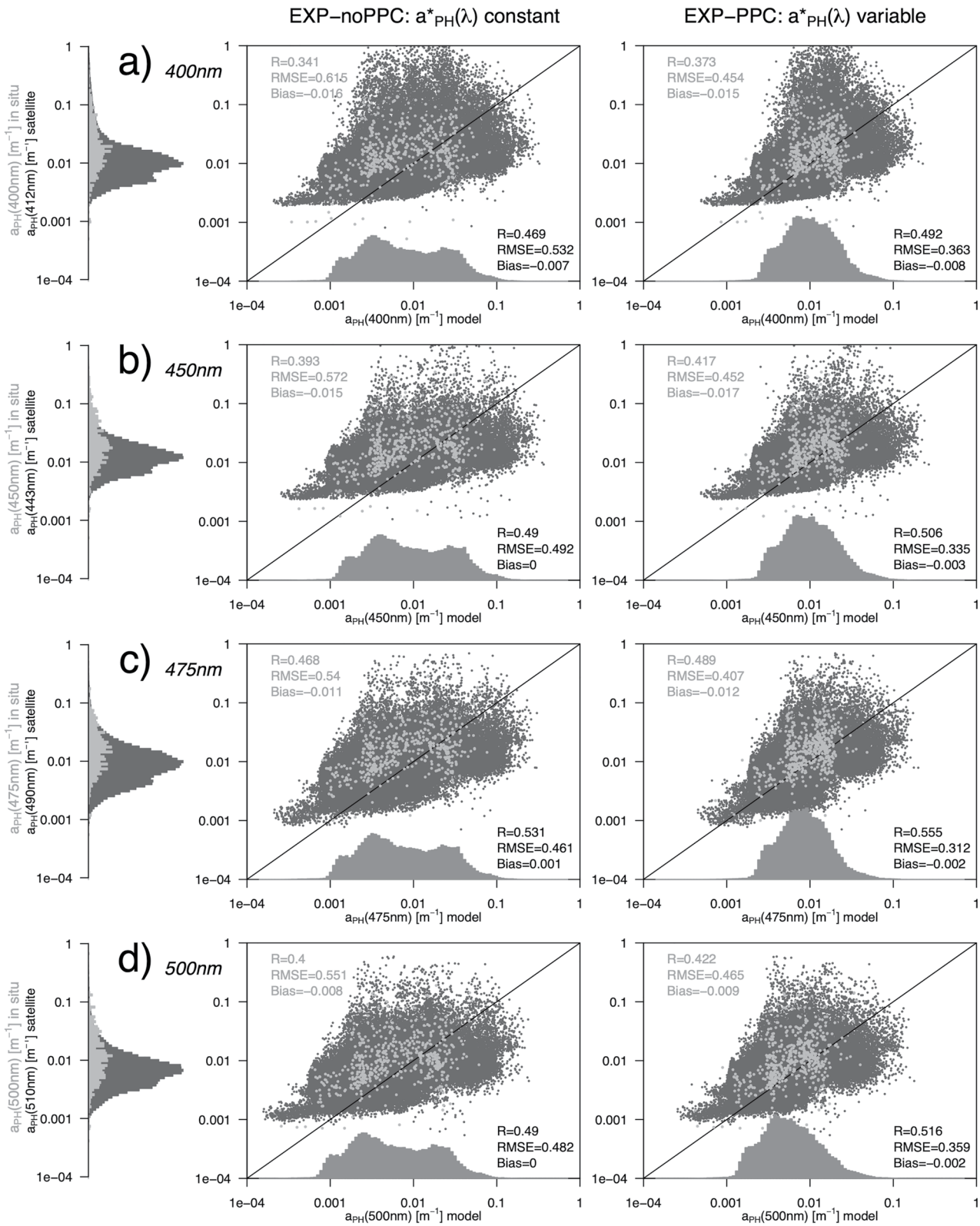

Figure 7. Log-transformed $a_{\mathrm{PH}}(\lambda)$ scatter plots in (a) 400, (b) 450, (c) 475, and (d) 500 nm wavebands: on the ordinate modeled data from EXP-noPPC (constant $a^*_{\mathrm{PH}}(\lambda)$, left panels) and EXP-PPC (variable $a^*_{\mathrm{PH}}(\lambda)$, right panels) and on the abscissa observed data in comparable data sets (in situ in light gray, satellite in dark gray). Vertical and horizontal histograms show the density distribution of $a_{\mathrm{PH}}(\lambda)$ data modeled and observed, respectively.

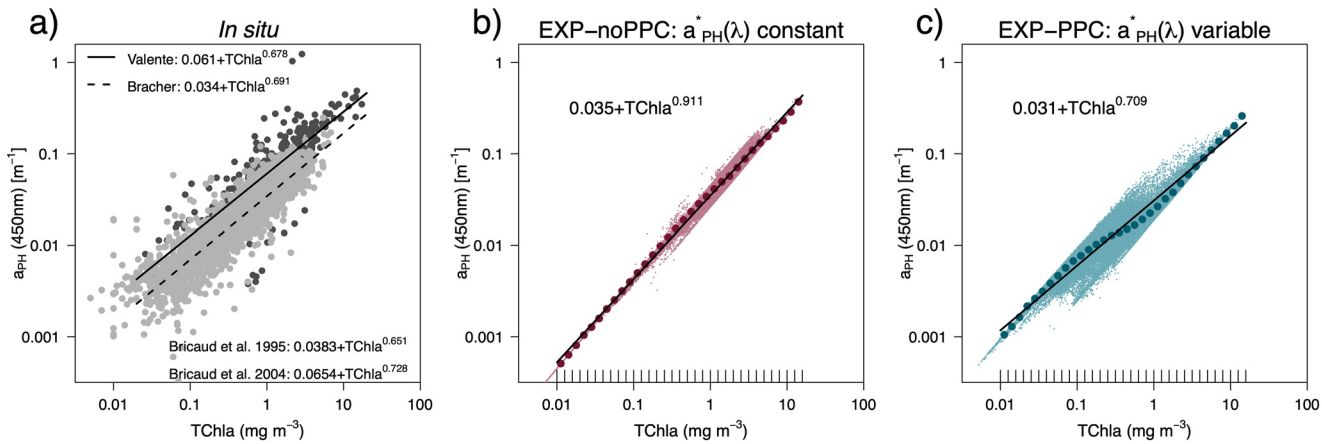

Figure 8. Bio-optical relationship of $a_{\mathrm{PH}}(450)$ (m^{-1}) as a function of TChla (mg m^{-3}) from (a) in situ observations compiled in Valente (black dots) and in Bracher (gray dots), and from model simulations in (b) EXP-noPPC (constant $a^*_{PH}(\lambda)$) and (c) EXP-PPC (variable $a^*_{\mathrm{PH}}(\lambda)$). Bins of TChla used to aggregate $a_{\mathrm{PH}}(450)$ values are indicated in panels (b and c) as inward ticks in the *x*-axis.

In situ observed $a^*_{\mathrm{PH}}(450)$ coefficients for the whole phytoplankton community ranged mostly from 0.001 to 0.15 m^2 mg Chl^{-1}, but there were values up to 0.25 m^2 mg Chl^{-1} (Figure 9a). In EXP-noPPC, $a^*_{PH}(450)$ ranged from 0.025 to 0.05 m^2 mg Chl^{-1}, the respective $a^*_{\mathrm{PH}}(\lambda)$ coefficients for diatoms and small phytoplankton at this wavelength (Figure 9b). On the other hand, EXP-PPC simulated community values for $a^*_{\mathrm{PH}}(450)$ that ranged from 0.02 to 0.1 m^2 mg Chl^{-1} (Figure 9c). The lower panels of Figure 9 show the vertical gradient of such range of variability. Note that in situ observed $a^*_{\mathrm{PH}}(450)$ coefficients were only integrated by the Bracher compilation. The range of $a^*_{\mathrm{PH}}(450)$ coefficients within each depth layer was shown (box and whiskers) together with the number of pixels with observations (*n*) (Figure 9d). In EXP-noPPC, $a^*_{\mathrm{PH}}(450)$ showed an almost constant range of variability with increasing depth (Figure 9e). In EXP-PPC, the range of variability for community $a^*_{\mathrm{PH}}(450)$ was in better agreement with observations in the first depth layers (Figure 9f versus Figure 9d above 50 m). When observed in depth, in EXP-PPC the range of values of community $a^*_{\mathrm{PH}}(450)$ tended to decrease as the proportion of PPC relative to TChl decreased with depth (Figure 9f). From observations, instead, there was a larger variability in $a^*_{\mathrm{PH}}(450)$ below 40 m and PPC:TChla remained higher than model simulations (red line in Figure 9d) but also highly variable (red shaded area in Figure 9d) below that depth.

4.4. Impact of Variable $a^*_{\mathrm{PH}}(\lambda)$ on the Spectral Shape of $R_{\mathrm{RS}}(\lambda)$

The OACs within the ocean dictate how sunlight is absorbed and scattered in the water column, ultimately shaping $R_{\mathrm{RS}}(\lambda)$. Prescribing constant $a^*_{\mathrm{PH}}(\lambda)$ essentially means that the variability in $a_{\mathrm{PH}}(\lambda)$ depends fully on variations of phytoplankton biomass and community composition. With variable $a^*_{\mathrm{PH}}(\lambda)$ the dependency of $a_{\mathrm{PH}}(\lambda)$ on phytoplankton TChla was less pronounced. To evaluate which was the effect of the simulated variability of $a^*_{\mathrm{PH}}(\lambda)$ coefficients in $R_{\mathrm{RS}}(\lambda)$, we compared the spectral shape of model derived $R_{\mathrm{RS}}(\lambda)$ with satellite retrievals and in situ observations.

The globally averaged spectral shape of $R_{\mathrm{RS}}(\lambda)$ from model simulations and from observations shows good agreement in the wavelengths between 425 and 525 nm. At longer wavebands, model simulations tend to underestimate $R_{\mathrm{RS}}(\lambda)$ (Figure 10a). Plots of surface fields showing $R_{\mathrm{RS}}(\lambda)$ simulated by the model, retrieved by satellites and observed in situ can be found in Text S3 in Supporting Information S1. When $R_{\mathrm{RS}}(\lambda)$ values were disaggregated by TChla concentration in the ocean surface, modeled $R_{\mathrm{RS}}(\lambda)$ is underestimated when TChla is in the range 0.9–1.1 mg m^{-3} (Figure 10b) and overestimated when TChla is in the range 0.09–0.11 mg m^{-3} (Figure 10d). The under/overestimation is smaller for EXP-PPC compared to EXP-noPPC which reflects the lower dependency of $a_{\mathrm{PH}}(\lambda)$ on total TChla of the model setup with variable $a^*_{\mathrm{PH}}(\lambda)$.

When $R_{\mathrm{RS}}(\lambda)$ values were disaggregated regionally, EXP-PPC results tended to perform better in low chlorophyll regions, such as the equatorial and subtropical permanently-stratified biomes, than EXP-noPPC (Figure 11a). In subpolar and subtropical seasonally-stratified biomes, on the other hand, differences in $R_{\mathrm{RS}}(\lambda)$ between EXP-noPPC and EXP-PPC are minimal (Figure 11b). In the ice biomes (defined as those with at least a 50%

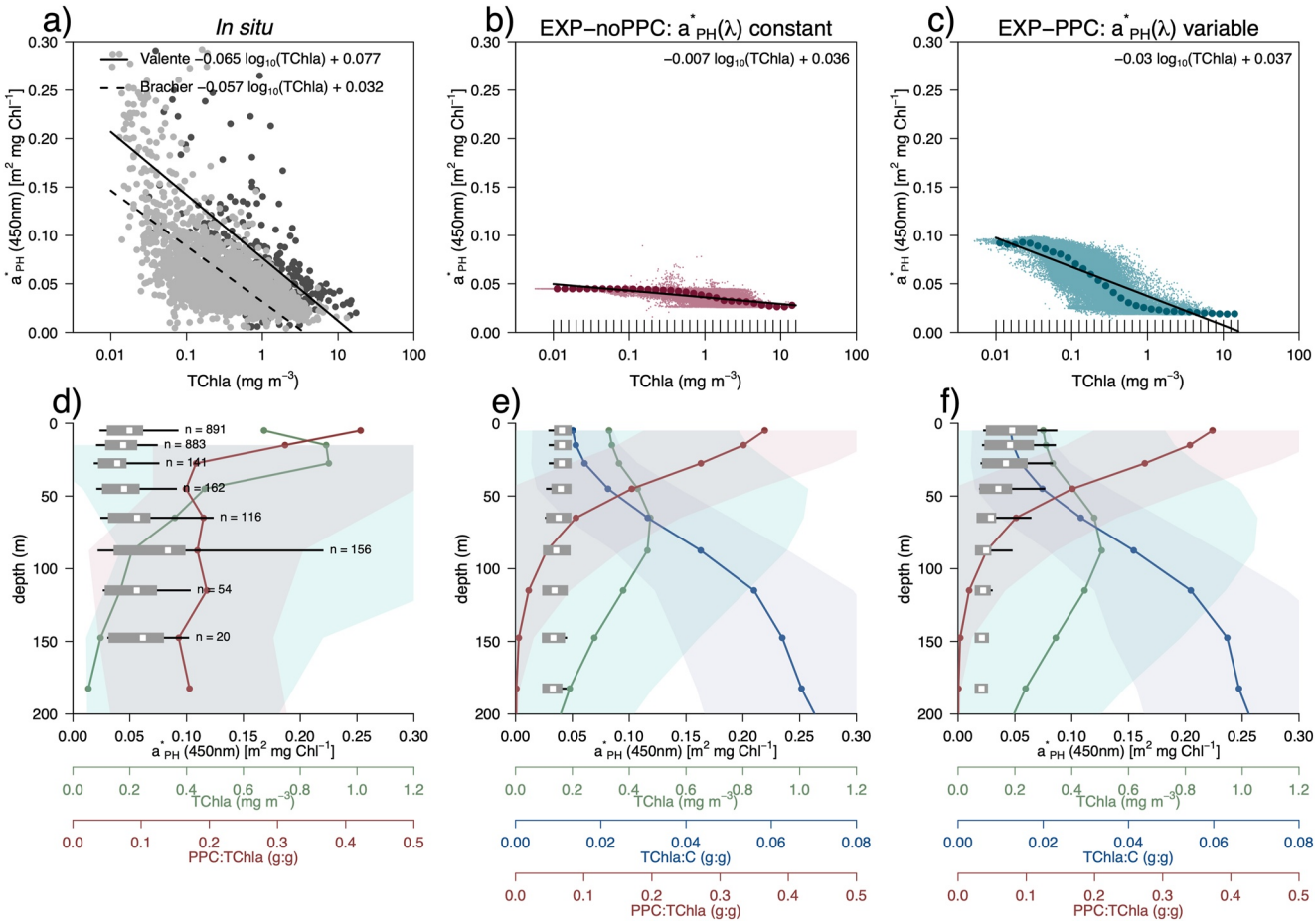

Figure 9. Variability of $a^*_{PH}(450)$ (m^2 mg Chl^{-1}) as a function of TChla (mg m^{-3}) from (a) in situ observations in Valente (black dots) and in Bracher (gray dots), and from model simulations in (b) EXP-noPPC (constant $a^*_{PH}(\lambda)$) and (c) EXP-PPC (variable $a^*_{PH}(\lambda)$). Bins of TChla used to aggregate $a^*_{PH}(450)$ values are indicated in panels (b and c) as inward ticks in the *x*-axis. For (d) the Bracher data set, (e) EXP-noPPC, and (f) EXP-PPC, lower panels show the variation in depth of the range of $a^*_{PH}(450)$ coefficients (box and whiskers), and the mean (points connected by lines) ± the standard deviation (shaded areas) of the TChla concentration (green), the PPC:TChla ratio (red) and the TChl:C ratio (blue).

ice-cover fraction during some time of the year by Fay and McKinley (2014)) the two model simulations are almost identical (Figure 11c) but there were remarkable discrepancies between satellite and in situ observations of $R_{RS}(\lambda)$ (also shown for $a_{PH}(450)$ poleward of 65° in Figure 6), which make these biomes more difficult to evaluate with our current model configuration.

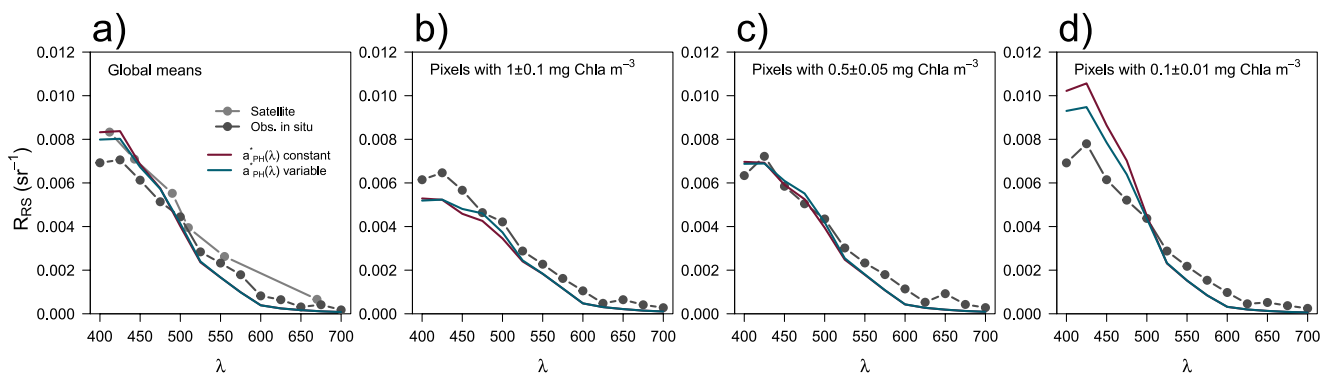

Figure 10. Spectral shape of $R_{RS}(\lambda)$ from in situ observations, satellite retrievals and model simulations: (a) global average and averages for pixels with TChl concentrations in the range (b) 1 ± 0.1, (c) 0.5 ± 0.05, and (d) 0.1 ± 0.01 mg Chl m^{-3}.

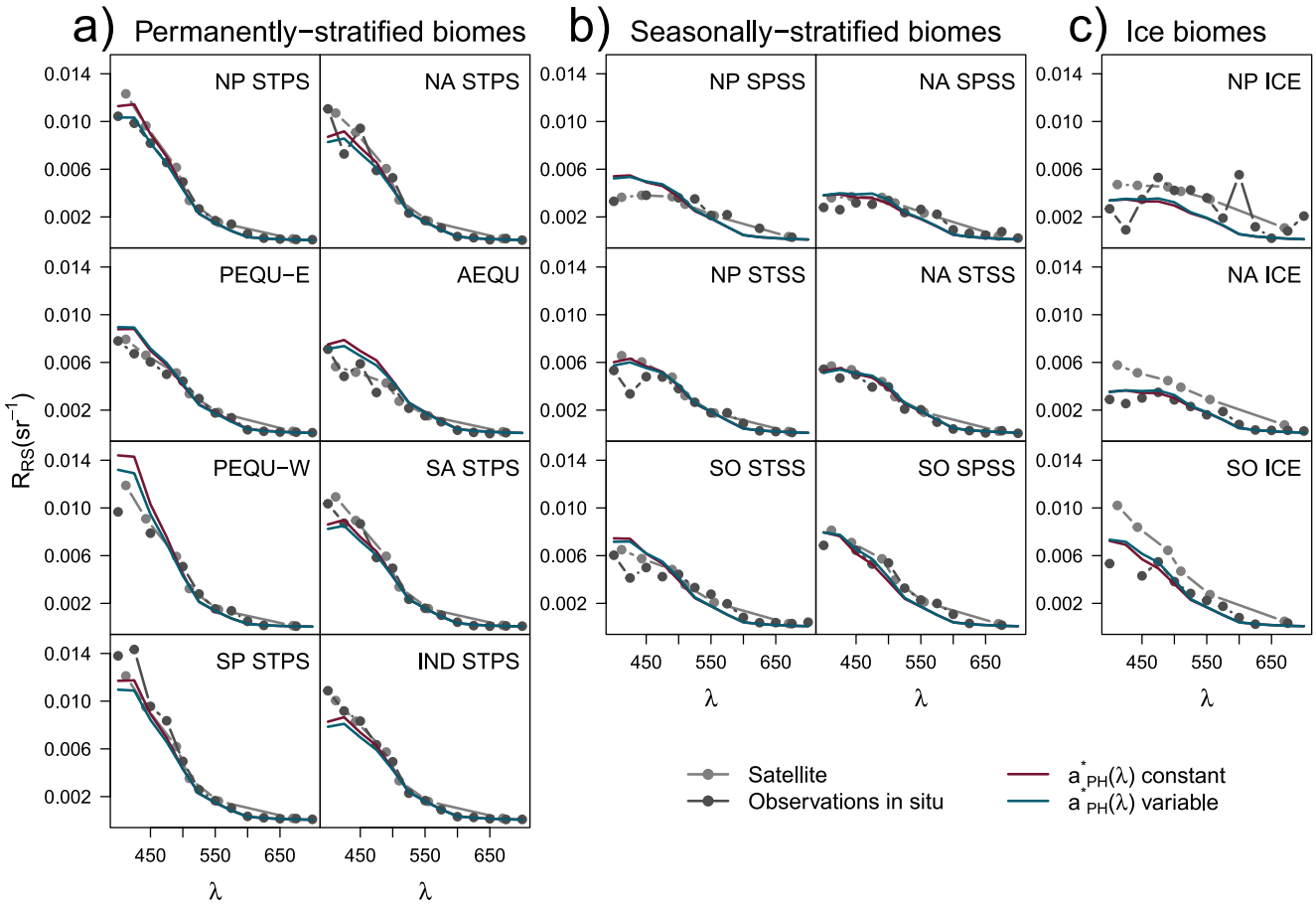

Figure 11. Spectral shape of $R_{RS}(\lambda)$ from in situ observations, satellite retrievals and model simulations (EXP-noPPC in red, EXP-PPC in blue) in different mean biomes defined by Fay and McKinley (2014): (a) equatorial and subtropical permanently-stratified biomes, (b) subpolar and subtropical seasonally-stratified biomes, and (c) ice biomes.

4.5. Performance Metrics With Constant and Variable $a^*_{PH}(\lambda)$

A comprehensive set of skill metrics for the EXP-noPPC and EXP-PPC, model simulations with constant and variable $a^*_{PH}(\lambda)$, respectively, compared to in situ observations is shown in the top panels of Figure 12 and compared to satellite products is shown in the bottom panels of Figure 12. In both simulations, the metrics for the BGC products, TChla and PPC:TChla, are similar (red letters for EXP-noPPC versus blue letters for EXP-PPC in Figures 12a and 12b). Annual means of log-transformed TChla show correlation coefficients around 0.53 when compared to in situ TChla observations (Figure 12a) and around 0.68 when compared to the satellite product (Figure 12b). The PPC:TChla ratio shows a correlation of 0.50 (Figure 12a). $R_{RS}(\lambda)$ in the shorter wavebands keep R above 0.5 when compared to in situ observations (a, b and c in Figure 12c) whereas $R_{RS}(\lambda)$ in the longer wavebands fall to Rs around 0.2–0.3 (d–f in Figure 12c). When compared to the satellite products, $R_{RS}(\lambda)$ in the shorter wavelengths keep R between 0.4 and 0.6 (a–c in Figure 12d) whereas $R_{RS}(\lambda)$ in the longer wavelengths fall below 0.2 (d–f in Figure 12d). For both sets of observations, only wavelengths from 400 to 500 were affected by the different formulation of $a^*_{PH}(\lambda)$ in EXP-noPPC and EXP-PPC (Figures 12c and 12d). Constituents IOPs show correlations below 0.4 when compared to their satellite counterparts (Figure 12f) and below 0.3 when compared to in situ observations (Figure 12e). However, the only IOPs affected by the different formulation of $a^*_{PH}(\lambda)$ in EXP-noPPC and EXP-PPC were $a_{PH}(\lambda)$ and $a_P(\lambda)$ for the in situ observations (a and b in Figure 12e) and $a_{PH}(\lambda)$ and $a_{TOT}(\lambda)$ for the satellite products (a and f in Figure 12e). The surface plots that illustrate all these comparisons are included in Text S3 in Supporting Information S1.

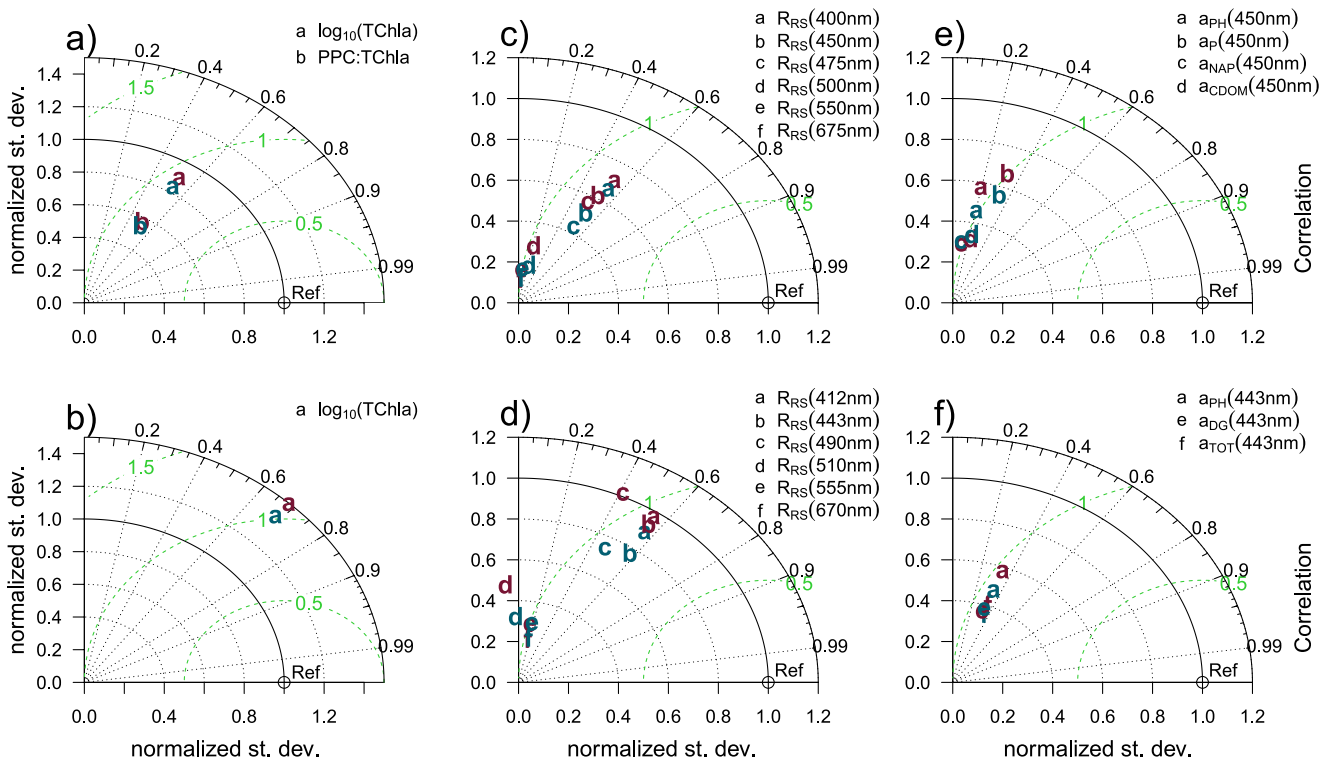

Figure 12. Taylor diagrams summarizing the skill metrics of EXP-noPPC (constant $a^*_{PH}(\lambda)$, in red) and EXP-PPC (variable $a^*_{PH}(\lambda)$, in blue) model output compared against observations taken in situ (top panels) and from satellite retrievals (bottom panels), of (a and b) biogeochemical products, (c and d) $R_{RS}(\lambda)$, and (e and f) inherent optical properties. Green lines show standard deviation arcs around the reference point. Taylor diagrams generated with the R packages *plotrix* 3.8–1 and *Metrics* 0.1.4.

5. Discussion

We present a stoichiometry-based approach to include variability in the optical properties of the phytoplankton community represented in a coupled BGC-optical model. The BGC model REcoM2 simulated a comprehensive pigment signature in terms of photosynthetic pigments and PPCs of two phytoplankton types, diatoms and small phytoplankton. We compared two versions of REcomM2, one where the chl-specific $a^*_{PH}(\lambda)$ coefficients of each phytoplankton type where kept constant and a second one, where the $a^*_{PH}(\lambda)$ coefficients of each phytoplankton type were made variable as a function of its content in PPCs. Using this approach, the bio-optical relationships between phytoplankton absorption, $a_{PH}(\lambda)$, and phytoplankton chlorophyll, commonly observed in nature, emerged. Alternatively, the BGC model had a limited ability to represent variability in $a_{PH}(\lambda)$ when it considered constant chl-specific $a^*_{PH}(\lambda)$ coefficients for each phytoplankton type. Bio-optical relationships between $a_{PH}(\lambda)$ and phytoplankton biomass deviated from observations when the only source of variability in the community aggregated absorption arose from changes in relative contribution of the phytoplankton types. This suggests that including variable $a^*_{PH}(\lambda)$ coefficients based on the content of non-photosynthetic pigments can help representing the spatial and temporal variability of $a_{PH}(\lambda)$ into coupled physical-BGC-optical models of the global ocean, especially in those that represent a limited number of phytoplankton optical types.

Therefore, this paper contributes to an increasing body of literature addressing the issue of including some flexibility in $a^*_{PH}(\lambda)$ coefficients. The election of $a^*_{PH}(\lambda)$ coefficients is central for connecting phytoplankton biomass to IOPs and hence it is a relevant question among BGC/ecosystem modelers that aim to include an optical description of the BGC components (IOCCG, 2020) and also in the ocean color community as they take an optical measurement and derive a BGC product (Werdell et al., 2018). In most cases of BGC-optical modeling, the approaches for representing the variability of $a_{PH}(\lambda)$ include using empirical relationships among $a_{PH}(\lambda)$ and TChla (Bricaud et al., 1995), depicting the allometric constraints of light-harvesting traits (Baird et al., 2013; Brewin et al., 2011) or describing optically different PFT's (e.g., Baird et al., 2016; Brewin et al., 2019; Dutkiewicz et al., 2015; Gregg & Rousseaux, 2016; Hickman et al., 2010). The main insight of our study would be that this variability could be inferred from some estimate of PPCs content provided by the BGC model. We have shown this here for the open

waters of the global ocean. If the focus is narrowed to the IOPs of habitats or regions associated with particular phytoplankton species assemblages, regional- or ecosystem-specific estimates of photoprotective pigments (e.g., Gustafsson et al., 2014; Polimene et al., 2012) can be obtained which may also be useful to improve $a_{\mathrm{PH}}(\lambda)$ estimates.

In this work, such estimate of PPC was derived through a physiological model that described the mechanisms of photoinhibition and photoprotection in phytoplankton (Álvarez et al., 2019). Compared to empirical approximations that derive $a_{\mathrm{PH}}(\lambda)$ based on bulk phytoplankton biomass (e.g., Bricaud et al., 1995; Lutz et al., 1996), our approach has a clear interpretation based on biological and/or optical considerations and provides plausible values of $a_{\mathrm{PH}}(\lambda)$ at the extremes of the Chla range because they are bounded by the prescribed variability of $a^*_{\mathrm{PH}}(\lambda)$. Furthermore, it is able to determine $a_{\mathrm{PH}}(\lambda)$, in principle, for all phytoplankton types represented in the BGC model. The same advantages can be assigned to the approach of portraying $a_{\mathrm{PH}}(\lambda)$ by describing optically different PFT's with constant $a^*_{\mathrm{PH}}(\lambda)$ used by many authors (e.g., Baird et al., 2016; Ciotti et al., 2002; Dutkiewicz et al., 2015; Sathyendranath et al., 2001; Wolanin et al., 2016). But this approach limits the optical variability of the phytoplankton compartment to the $a^*_{\mathrm{PH}}(\lambda)$ spectra prescribed for the PFTs included in the model and do not allow intra-type variability in $a^*_{\mathrm{PH}}(\lambda)$. The reason behind is that intra-type variability is likely to have a small effect compared to differences in $a^*_{\mathrm{PH}}(\lambda)$ spectra between phytoplankton types. However, to the best of our knowledge, there is no systematic analysis on how optically diverse the phytoplankton compartment of a BGC model must be to represent the spatial and temporal variability of $a_{\mathrm{PH}}(\lambda)$.

Phytoplankton content in PPC can be inferred though relatively simple statistical relationships with environmental drivers (Álvarez et al., 2019), which in principle, might be useful to improve $a_{\mathrm{PH}}(\lambda)$ estimates. In that case, the empirical nature of the PPC estimate cannot, by definition, lead to any predictive skill. By impacting $a^*_{\mathrm{PH}}(\lambda)$ coefficients with a mechanistically-derived simulation of PPC, our approach incorporates the influence of light, temperature and nutrient availability on the light harvesting capacity of the phytoplankton community. Changes in the community PPC:Chla ratio encompassed both shifts in community composition and physiological acclimation, and hence both processes are expected to impact our estimates of $a_{\mathrm{PH}}(\lambda)$. Thus, our approach could permit to gain insight on how the combined effects of temperature, nutrients and light may influence the coupling between available light and carbon fixation by phytoplankton. Ultimately, it increases the ability of the BGC model to accurately simulate the response of primary producers under both present and future scenarios.

Total absorption by phytoplankton, $a_{\mathrm{PH}}(\lambda)$, alters the underwater light field and hence the photosynthetic response of phytoplankton. Therefore, the extent to which BGC models with bio-optical components are able to represent variability in $a_{\mathrm{PH}}(\lambda)$ affects their ability to simulate accurately other BGC processes, such as primary production. Variability in $a^*_{\mathrm{PH}}(\lambda)$ coefficients affects the total energy absorbed by phytoplankton assemblages and hence how phytoplankton attenuates light and shades the water column below. We observed that when the impact of photoacclimative processes in $a^*_{\mathrm{PH}}(\lambda)$ was taken into account, our globally-integrated annual estimates of NPP were increased by 1.27 PgC year^{-1}. This was not mediated by any change in the photosynthetic capability of the phytoplankton, because $a^*_{\mathrm{PS}}(\lambda)$ coefficients and photochemical efficiency were unaffected in our experiments, but by changes in the underwater light field. Since TChla concentrations were very similar between EXP-noPPC and EXP-PPC (Figures 5a and 5b, Figures S4c and S4d in Supporting Information S1) the variations in $a_{\mathrm{PH}}(\lambda)$ that affected the underwater light field were likely driven by variations in $a^*_{\mathrm{PH}}(\lambda)$. This suggests that taking into account photoprotection mechanisms that modify the relative importance of photochemical versus non-photochemical pathways can affect substantially modelled primary production. Ocean color-based models that incorporate IOPs derived from satellite measurements into the calculation of phytoplankton growth rates, have shown to obtain improved NPP estimates when compared to direct field measurements (Silsbe et al., 2016). Our results open interesting questions regarding whether a BGC model that explicitly represents photoprotection mechanisms on the derivation of IOPs would obtain similar results.

Other potential directions for future development need to be highlighted nonetheless. Since $a^*_{\mathrm{PH}}(\lambda)$ coefficients are variable based on an empirical relationship with model-derived PPC, our estimates of $a_{\mathrm{PH}}(\lambda)$ are inevitably influenced by the skill of the underlying pigments model and by the choice of the empirical relationship. Our PPC simulations were quite robust under the environmental conditions simulated by the model (Text S2 in Supporting Information S1). The photoinhibition model simulated the content in PPC aligning them to the photoprotection needs of the phytoplankton community under given environmental conditions. This means that the phytoplankton community accumulates as much PPC content as necessary to avoid photoinhibition, by means of acclimation

and/or by changes in community composition. Hence, in future it might be necessary to incorporate limits to the photoprotection capabilities of the community, that is, limits to the biosynthesis of pigments by nutrient availability (Alderkamp et al., 2010), constraints to changes in community composition, or shifts to photoprotection mechanisms that do not involve the synthesis of PPCs (Porcar-Castell et al., 2006; Wagner et al., 2006). In our present setup, we used an empirical relationship between PPC:TChla and the spectral shape of $a^*_{\mathrm{PH}}(\lambda)$. The fact that this relationship could be temporal or regionally variable induces uncertainty in our results. A spectrally-resolved description of the processes involved in PSII inactivation and repair would permit the direct simulation of $a^*_{\mathrm{PH}}(\lambda)$, without having to rely on an empirical connection to PPC:Chla.

Despite potential further improvements of the model configuration, our results simulating the variability of $a_{\mathrm{PH}}(\lambda)$ for the global ocean are supported by a very thorough validation with an extensive collection of in situ observations and satellite retrievals of different bio-optical parameters and biochemical products. Some uncertainty arises from the difficulties in comparing the three sources of data that we considered in this work. Challenges comparing BGC model output, ocean color products and in situ observations are remarkable (IOCCG, 2020) and include misrepresented temporal and spatial scales and the mismatch between the wavebands in model output (400:25:700 nm) and the bands measured by satellite sensors (412, 443, 490, 510, 555, and 670 nm), the level of derivation and associated uncertainty of satellite products (Zheng & DiGiacomo, 2017), the scarcity of observations in the less intensively sampled regions, and the uncertainty in model output that can result from uncertain estimates of parameter values, errors in the model structure compared to the real system, and approximations made by the numerical methods employed in the simulation.

To reduce spectral and spatial-temporal mismatches, further model developments can be targeted towards increased spectral and spatial-temporal resolutions. In the future, an increased spatial resolution of the model and more frequent forcing and output could partly decrease the related mismatches between the compared model, satellite and in situ data. The extension of the spectral range and increase of the spectral resolution is also possible, while current evaluation is limited by the satellite waveband setting. A general problem in development and evaluation of ocean color satellite products (Wolanin et al., 2016) is that the considered spectral range (from 375 nm) as well as resolution are crucial for distinguishing different types of phytoplankton (given their different specific absorption spectra) and a finer (hyper-)resolution (5–10 nm) is desired. Generally, extended spectral range and increased spectral resolution of the model and satellite measurements would allow to resolve accurately distinct absorption details related, for instance, to specific phytoplankton types especially if more than two PFTs are considered, and, therefore, to reduce the mismatches.

Challenges regarding the availability of observations involve both their spatial and temporal coverage and the collocation of optical and BGC data. We presented a nearly-global model setup (excluding areas poleward of 80°N) but there are areas poorly represented in some of the observational data sets. This was particularly true for polar regions, where modelled and observed, but also in situ and satellite, $a_{\mathrm{PH}}(\lambda)$ (Figure 6) and $R_{\mathrm{RS}}(\lambda)$ (Figure 11) were significantly different. Our proposed model connects physiological processes described for several types of phytoplankton with optical properties, and therefore its validation demands data sets that could provide optical data concurrent with pigments data and taxonomical information. The NOMAD data set (Werdell & Bailey, 2005) is the primary example as it provides collocated and complete optical and HPLC data. Similarly, Valente et al. (2019a) provides collocated optical with TChla data which is also very useful to derive chl-specific $a^*_{\mathrm{PH}}(\lambda)$, although leaves out the rest of the pigments and limits their use for obtaining taxonomical information. The Bracher data sets use consistent naming conventions that allow to match optical data sets with their correspondent HPLC samples, therefore providing concurrent information on optics, pigments, and HPLC-derived taxonomy. These kind of comprehensive data sets are crucial to develop and validate modelling tools that connect the photo-physiological processes of a diverse phytoplankton community with optics. We hope that modelling studies like this one presented will encourage instrumental oceanographers, ocean color experts and BGC/ecosystem modelers to advance in the implementation of mechanisms (e.g., naming conventions, sample IDs, and formatted databases) that could stimulate interdisciplinary studies.

Uncertainty in model output related to processes other than the photoacclimation and photoprotection mechanisms considered here also affected our results. Although model simulations of phytoplankton Chla were in the range of accuracy of most BGC models (Text S2 in Supporting Information S1), phytoplankton Chla tended to be higher than expected in the areas where multi-nutrient limitation to phytoplankton growth swaps from being mainly N-limited to Fe-limited, likely reflecting an improvable description of colimitation processes. This

affected the simulation of IOPs as well, especially around the oligotrophic gyres. But, despite being very noticeable in the maps (Figure 4 and Figure S3 in Supporting Information S1), those pixels represent a very small proportion of the model output.

The reduced range of variability of $a_{\mathrm{PH}}(\lambda)$, simulated using variable $a^*_{\mathrm{PH}}(\lambda)$ and result of the non-isometric bio-optical relationship with TChla, contributed to improve the simulation of $R_{\mathrm{RS}}(\lambda)$ along wavelengths from 400 to 500 nm (Figures 10 and 11). Low-chlorophyll regions and high-latitude bloom-forming regions can have vastly different chlorophyll concentrations that primarily reflect differences in phytoplankton biomass. But $R_{\mathrm{RS}}(\lambda)$ reflect also differences in all optical properties, which is much better captured by a model with variable $a^*_{\mathrm{PH}}(\lambda)$. For the bands longer than 525 nm, the model-data discrepancies are the same with constant or variable $a^*_{\mathrm{PH}}(\lambda)$, and the model tends to underestimate $R_{\mathrm{RS}}(\lambda)$ with respect to observations. This could be due the absence in our model parameterization of inelastic light sources such as fluorescence and Raman scattering (B. R. Marshall & Smith, 1990). Nevertheless, results presented suggest that the global water-leaving radiances obtained with the proposed model structure might have potential uses in the future, observing the due caution of the limits of our simulation and the caveats in the simulation of the longer wavelengths. Those applications might include the exploration of the impact in $R_{\mathrm{RS}}(\lambda)$ of changes in the amount and/or optical properties of the BGC components and the assimilation into models of diverse optical products other than TChla. Moreover, an improved simulation of the relationship between $R_{\mathrm{RS}}(\lambda)$ and TChla through the mechanistic description of photophysiological processes will allow the exploration of the reliability of empirically-derived ocean color algorithms that connect $R_{\mathrm{RS}}(\lambda)$ and TChla over the next century.

6. Summary and Concluding Remarks

The incorporation of absorption-based models into BGC models of the global ocean have several advantages since they allow relating spectrally-resolved photophysiological processes (regarding both energy gain and use) with other relevant processes in phytoplankton activity and ecology. Representing the optical variability of the phytoplankton community by prescribing a limited number of phytoplankton types with constant chlorophyll-specific $a^*_{\mathrm{PH}}(\lambda)$ coefficients, even if they are relatively representative for the global ocean, generated $R_{\mathrm{RS}}(\lambda)$ and IOPs whose variability was highly tight to the variability in the chlorophyll concentration. Representing the variability in chlorophyll-specific $a^*_{\mathrm{PH}}(\lambda)$ through the effect of the accumulation of PPCs contributed significantly to improving simulations of the light harvesting capabilities of the phytoplankton types represented in the BGC model REcoM2. The content of PPC pigments of the phytoplankton community impacted significantly the simulated variability of $a_{\mathrm{PH}}(\lambda)$ in the global ocean. This was supported by a very thorough validation with in situ observations of bio-optical and BGC parameters. The statistical relationships observed between $a_{\mathrm{PH}}(\lambda)$ and TChla in the ocean and that indicate the existence of covariations between TChla, the proportions of accessory pigments relative to TChla and the average size of algal populations, was reproduced by the optical-BGC model. The improved representation of the light harvesting-related capabilities of the phytoplankton community lead to decreased $R_{\mathrm{RS}}(\lambda)$ at low latitude oligotrophic regions, and an increase of $R_{\mathrm{RS}}(\lambda)$ at more productive regions, which was in better agreement with satellite retrievals of water-leaving radiances. Hence, a central message from the present work would be that physiological factors that shape differentially the light harvesting capabilities of the phytoplankton community must be considered when evaluating the coupling between phytoplankton IOPs and phytoplankton biomass. This implies to represent better how changes in community composition and pigment content relate to environmental drivers and examine whether photoacclimation, both regarding photosynthetic and photoprotective pigments, influence significantly the underwater light field and the resultant water-leaving radiances.

Data Availability Statement

MIT general circulation model (MITgcm) code can be obtained by cloning https://github.com/MITgcm/MITgcm.git (Campin et al., 2021) with the checkpoint version "checkpoint68d." Regulated Ecosystem Model version 2 (REcoM2) is designed as an additional package to MITgcm and the version described in this work can be obtained by cloning: https://github.com/ealvarez-s/code_recom_radtrans.git (Álvarez, Losa, et al., 2022). The description of the model code included in the archive and documentation for compiling the two executables used in this work (with constant and variable $a^*_{\mathrm{PH}}(\lambda)$) can be found on the PDF file "manual.pdf" also available in the repository. The code modifications (in the package *gchem*) required to use REcoM2 as the biogeochemical model

Acknowledgments
This work is a contribution to the IPSO project "Improving the prediction of photophysiology in the Southern Ocean by accounting for iron limitation, optical properties and spectral satellite data information" funded by the Alfred Wegener Institute (AWI). EÁ has been supported partially in this work by OGS and CINECA under the HPC-TRES program (research line A10), co-funded by the Italian Ministry of Universities and Research through the PRACE-Italy research infrastructure grant. The contribution of SNL was partly made in the framework of the state assignment of the Federal Agency for Scientific Organizations (FASO) Russia (theme FMWE-2021-0014). All simulations were conducted on the GALILEO supercomputing facility at the CINECA consortium; the authors acknowledge the CINECA award under the ISCRA initiative (HP10CMKVJ2) for the availability of high-performance computing resources and support. The authors are thankful to all the scientists and crew involved in the data collection and analyses for providing in situ data via public accessible data bases. For the in situ data collection from AB provided first in the frame of this manuscript (expeditions ANT24.4, ANT26.4, HE462, PS93.2, PS99.1, PS99.2, PS113, PS121, SO218, and SO235) the authors acknowledge the work by many Phytooptics (AWI) group members and collaborators supported by the captain, crew and other scientists and the funding by the Helmholtz Association (HGF Innovative Network Funds Phytooptics, Helmholtz Infrastructure Initiative FRAM), the European Union (Seventh Framework Programme SHIVA-226224FP7-ENV-2008-1), the BMBF (OASIS 03G0235A), ESA (S5P+Innovation Theme 7 Ocean Color 532 (S5POC) project No 4000127533/19/I-NS), the DFG (#268020496-TRR 172 project C03 within the Transregional Collaborative Research Center ArctiC Amplication: Climate Relevant Atmospheric and SurfaCe Processes, and Feedback Mechanisms (AC)3) and the collaborative project OLCI-PFT (ACRI-AWI Offer #209-180104). The authors acknowledge ESA Ocean Color Climate Change Initiative project for providing free and open satellite products as the Ocean Color Climate Change Initiative data set (Version 4.2, European Space Agency) available online at http://www.esa-ocean-colour-cci.org/. AEsOP/CSIRO database is populated with data sets from the Australia's Integrated Marine Observing System (IMOS) which is enabled by the National Collaborative Research Infrastructure Strategy (NCRIS), operated by a consortium of institutions as an unincorporated joint venture, with the University of Tasmania as Lead Agent.

within MITgcm version 68d can be obtained from: https://github.com/ealvarez-s/gchem_recom_MITgcm68d.git. The working directory where all experiments presented in the work can be run can be found at https://github.com/ealvarez-s/global_aphyt.git. The user-configuration files to run the experiments can be found in the directory "namelist/" and all input, forcing and initialization files can be found in the directory "input/." Spectral light at the top of the ocean data can be obtained from the Global Modelling and Assimilation Office of the NASA at https://gmao.gsfc.nasa.gov/gmaoftp/NOBM/monthly/eds/ (accessed 24 October 2019). The collection of absorption spectra of phytoplankton taxa are included as Supporting Information in Álvarez, Lazzari, et al. (2022) and the weight specific absorption spectra for each pigment group are those from Bidigare et al. (1990) available at https://www.oceanopticsbook.info/view/optical-constituents-of-the-ocean/phytoplankton (accessed 22 April 2020). Data sets of $R_{RS}(\lambda)$, inherent optical properties and High-Performance Liquid Chromatography phytoplankton pigments are available in the in-text data citation references gathered in Table 3 and the References list. Such data sets are findable and accessible in SeaBASS, Pangaea, and AesOP-CSIRO. Data from satellites can be obtained from the Ocean Color Climate Change Initiative project at https://www.oceancolour.org/. Data, model output, and scripts for analysis of results can be obtained from: https://github.com/ealvarez-s/results_aphyt.git The analysis of model output has been performed with *R* using the packages *abind* 1.4–5, *akima* 0.6–2.1, *chron* 2.3–56, *Hmisc* 4.5–0, *lmodel2* 1.7–3, *Metrics* 0.1.4, and *RNetCDF* 2.4–2 for data analysis and *plotrix* 3.8–1, *plot3D* 1.3, *unikn* 0.4.0, *viridisLite* 0.4.0, and *wesanderson* 0.3.6 for visualization (all publicly available in CRAN, https://cran.r-project.org/). Model output can be found under the directory "Res_model/" together with a list of the simulations performed (in EXP-S, EXP-noPPC, EXP-PPC, and EXP-D). The formatted collection of observations can be found under the directory "Dat_observations/." Scripts used for processing model output and observations, and generating the figures shown in this work can be found under the directory "Scripts/" numbered by order of execution.

References

Álvarez, E., Lazzari, P., & Cossarini, G. (2022). Phytoplankton diversity emerging from chromatic adaptation and competition for light. *Progress in Oceanography*, *204*, 102789. https://doi.org/10.1016/j.pocean.2022.102789

Álvarez, E., Losa, S. N., & Völker, C. (2022). ealvarez-s/code_recom_radtrans: Initial release of radiative transfer model in REcoM2 via GitHub (v1.0) [Software]. Zenodo. https://doi.org/10.5281/zenodo.6418329

Álvarez, E., Thoms, S., Bracher, A., Liu, Y., & Völker, C. (2019). Modeling photoprotection at global scale: The relative role of Nonphotosynthetic pigments, physiological state and species composition. *Global Biogeochemical Cycles*, *33*(7), 904–926. https://doi.org/10.1029/2018GB006101

Álvarez, E., Thoms, S., & Völker, C. (2018). Chlorophyll to carbon ratio derived from a global ecosystem model with photodamage. *Global Biogeochemical Cycles*, *32*(5), 799–816. https://doi.org/10.1029/2017GB005850

Aas, E. (1987). Two-stream irradiance model for deep waters. *Applied Optics*, *26*(11), 2095–2101. https://doi.org/10.1364/AO.26.002095

Ackleson, S. G., Balch, W. M., & Holligan, P. M. (1994). Response of water-leaving radiance to particulate calcite and chlorophyll *a* concentrations: A model for Gulf of Maine coccolithophore blooms. *Journal of Geophysical Research*, *99*(C4), 7483–7500. https://doi.org/10.1029/93JC02150

Aiken, J., Pradhan, Y., Barlow, R., Lavender, S., Poulton, A., Holligan, P., & Hardman-Mountford, N. (2009). Phytoplankton pigments and functional types in the Atlantic Ocean: A decadal assessment, 1995–2005. *Deep Sea Research Part II: Topical Studies in Oceanography*, *56*(15), 899–917. https://doi.org/10.1016/j.dsr2.2008.09.017

Alderkamp, A.-C., de Baar, H. J. W., Visser, R. J. W., & Arrigo, K. R. (2010). Can photoinhibition control phytoplankton abundance in deeply mixed water columns of the Southern Ocean? *Limnology & Oceanography*, *55*(3), 1248–1264. https://doi.org/10.4319/lo.2010.55.3.1248

Antonov, J. I., Seidov, D., Boyer, T. P., Locarnini, R. A., Mishonov, A. V., Garcia, H. E., et al. (2010). World Ocean Atlas 2009, volume 2: Salinity. In *NOAA Atlas NESDIS 68* (Vol. 2, p. 184).

Arbones, B., Figueiras, F. G., & Varela, R. (2000). Action spectrum and maximum quantum yield of carbon fixation in natural phytoplankton populations: Implications for primary production estimates in the ocean. *Journal of Marine Systems*, *26*(1), 97–114. https://doi.org/10.1016/S0924-7963(00)00042-7

Aumont, O., Maier-Reimer, E., Blain, S., & Monfray, P. (2003). An ecosystem model of the global ocean including Fe, Si, P colimitations. *Global Biogeochemical Cycles*, *17*(2), 1060. https://doi.org/10.1029/2001GB001745

Babin, M., Morel, A., Claustre, H., Bricaud, A., Kolber, Z., & Falkowski, P. G. (1996). Nitrogen- and irradiance-dependent variations of the maximum quantum yield of carbon fixation in eutrophic, mesotrophic and oligotrophic marine systems. *Deep Sea Research Part I: Oceanographic Research Papers*, *43*(8), 1241–1272. https://doi.org/10.1016/0967-0637(96)00058-1

Babin, M., Therriault, J.-C., Legendre, L., & Condal, A. (1993). Variations in the specific absorption coefficient for natural phytoplankton assemblages: Impact on estimates of primary production. *Limnology & Oceanography*, *38*(1), 154–177. https://doi.org/10.4319/lo.1993.38.1.0154

Baird, M. E., Cherukuru, N., Jones, E., Margvelashvili, N., Mongin, M., Oubelkheir, K., et al. (2016). Remote-sensing reflectance and true colour produced by a coupled hydrodynamic, optical, sediment, biogeochemical model of the Great Barrier Reef, Australia: Comparison with satellite data. *Environmental Modelling & Software*, *78*(April), 79–96. https://doi.org/10.1016/j.envsoft.2015.11.025

Baird, M. E., Ralph, P. J., Rizwi, F., Wild-Allen, K., & Steven, A. D. L. (2013). A dynamic model of the cellular carbon to chlorophyll ratio applied to a batch culture and a continental shelf ecosystem. *Limnology & Oceanography*, *58*(4), 1215–1226. https://doi.org/10.4319/lo.2013.58.4.1215

Bannister, T. T. (1974). A general theory of steady state phytoplankton growth in a nutrient saturated mixed layer. *Limnology & Oceanography*, *19*(1), 13–30. https://doi.org/10.4319/lo.1974.19.1.0013

Barlow, R. G., Aiken, J., Holligan, P. M., Cummings, D. G., Maritorena, S., & Hooker, S. (2002). Phytoplankton pigment and absorption characteristics along meridional transects in the Atlantic Ocean. *Deep Sea Research Part I: Oceanographic Research Papers*, *49*(4), 637–660. https://doi.org/10.1016/S0967-0637(01)00081-4

Barlow, R. G., Cummings, D. G., & Gibb, S. W. (1997). Improved resolution of mono- and divinyl chlorophylls a and b and zeaxanthin and lutein in phytoplankton extracts using reverse phase C-8 HPLC. *Marine Ecology Progress Series*, *161*, 303–307. https://doi.org/10.3354/meps161303

Barlow, R. G., Lamont, T., Britz, K., & Sessions, H. (2013). Mechanisms of phytoplankton adaptation to environmental variability in a shelf ecosystem. *Estuarine, Coastal and Shelf Science*, *133*, 45–57. https://doi.org/10.1016/j.ecss.2013.08.006

Behrenfeld, M., Cetinić, I., Gilerson, A., & Twardowski, M. (2014). SABOR (Ship-Aircraft bio-Optical research) collaborative campaign [Dataset]. SeaBASS. https://doi.org/10.5067/SeaBASS/SABOR/DATA001

Bidigare, R. R. (1991). Analysis of algal chlorophylls and carotenoids. In D. C. Hurd & D. W. Spencer (Eds.), *Geophysical Monographs Series* (pp. 119–123). American Geophysical Union. https://doi.org/10.1029/GM063p0119

Bidigare, R. R., Ondrusek, M. E., Morrow, J. H., & Kiefer, D. A. (1990). In-vivo absorption properties of algal pigments. In *Proceedings of SPIE 1302, Ocean Optics X*. Technical Symposium on Optics, Electro-Optics, and Sensors. https://doi.org/10.1117/12.21451

Bracher, A. (2014a). Phytoplankton pigment concentrations during POLARSTERN cruise ANT-XXVIII/3 [Dataset]. Pangaea. https://doi.org/10.1594/PANGAEA.848588

Bracher, A. (2014b). Phytoplankton pigments measured on water bottle samples during SONNE cruise SO218 [Dataset]. Pangaea. https://doi.org/10.1594/PANGAEA.848589

Bracher, A. (2015a). Phytoplankton pigment concentrations during Maria S. Merian cruise MSM18/3 [Dataset]. Pangaea. https://doi.org/10.1594/PANGAEA.848586

Bracher, A. (2015b). Phytoplankton pigment concentrations during POLARSTERN cruise ANT-XXIV/1 [Dataset]. Pangaea. https://doi.org/10.1594/PANGAEA.848583

Bracher, A. (2015c). Phytoplankton pigment concentrations during POLARSTERN cruise ANT-XXIV/4 [Dataset]. Pangaea. https://doi.org/10.1594/PANGAEA.848584

Bracher, A. (2015d). Phytoplankton pigment concentrations during POLARSTERN cruise ANT-XXVI/4 [Dataset]. Pangaea. https://doi.org/10.1594/PANGAEA.848585

Bracher, A. (2015e). Phytoplankton pigment concentrations during POLARSTERN cruise ANT-XXVII/2 [Dataset]. Pangaea. https://doi.org/10.1594/PANGAEA.848590

Bracher, A. (2019a). Phytoplankton pigment concentrations during RV Sonne cruise SO243 [Dataset]. Pangaea. https://doi.org/10.1594/PANGAEA.898920

Bracher, A. (2019b). Phytoplankton pigment concentrations in the Southern Ocean during RV Polarstern cruise PS103 in Dec 2016 to Jan 2017 [Dataset]. Pangaea. https://doi.org/10.1594/PANGAEA.898941

Bracher, A., Cheah, W., & Wiegmann, S. (2019). Phytoplankton pigment concentrations in the tropical Indian Ocean in July and August 2014 during RV Sonne cruises SO234 and SO235 [Dataset]. Pangaea. https://doi.org/10.1594/PANGAEA.898929

Bracher, A., Gonçalves-Araujo, R., Dinter, T., & Cherkasheva, A. (2018). Remote sensing reflectance obtained from spectral underwater upwelling radiance and solar downwelling irradiance measurements during POLARSTERN cruise ARK-XXVI/3 (PS78) [Dataset]. Pangaea. https://doi.org/10.1594/PANGAEA.884528

Bracher, A., & Liu, Y. (2021a). Spectrophotometric measurements of absorption coefficients by non-algal particles in the Atlantic Southern Ocean during RV POLARSTERN cruise PS103 in Dec 2016 to Jan 2017 [Dataset]. Pangaea. https://doi.org/10.1594/PANGAEA.938196

Bracher, A., & Liu, Y. (2021b). Spectrophotometric measurements of absorption coefficients by phytoplankton in the Atlantic Southern Ocean during RV POLARSTERN cruise PS103 in Dec 2016 to Jan 2017 [Dataset]. Pangaea. https://doi.org/10.1594/PANGAEA.938193

Bracher, A., Liu, Y., Hellmann, S., & Röttgers, R. (2021a). Absorption coefficients by coloured dissolved organic matter from North Sea to Fram Strait measured at fixed stations with a Liquid Waveguide Capillary Cell system during POLARSTERN cruise PS99.1 [Dataset]. Pangaea. https://doi.org/10.1594/PANGAEA.938491

Bracher, A., Liu, Y., Hellmann, S., & Röttgers, R. (2021b). Absorption coefficients by coloured dissolved organic matter from North Sea to Fram Strait measured underway with a Liquid Waveguide Capillary Cell system during POLARSTERN cruise PS99.1 [Dataset]. Pangaea. https://doi.org/10.1594/PANGAEA.938494

Bracher, A., Liu, Y., Oelker, J., & Röttgers, R. (2021c). Absorption coefficients by coloured dissolved organic matter across the South Atlantic Ocean measured at fixed stations with a Liquid Waveguide Capillary Cell system during POLARSTERN cruise PS103 [Dataset]. Pangaea. https://doi.org/10.1594/PANGAEA.938467

Bracher, A., Liu, Y., Oelker, J., & Röttgers, R. (2021d). Absorption coefficients by coloured dissolved organic matter across the South Atlantic Ocean measured underway with a Liquid Waveguide Capillary Cell system during POLARSTERN cruise PS103 [Dataset]. Pangaea. https://doi.org/10.1594/PANGAEA.938468

Bracher, A., Liu, Y., & Wiegmann, S. (2021e). Spectrophotometric measurements of absorption coefficients by non-algal particles during HEINCKE cruise HE462 in the North sea and Sogne Fjord from 29 April to 7 May 2016 [Dataset]. Pangaea. https://doi.org/10.1594/PANGAEA.938152

Bracher, A., Liu, Y., & Wiegmann, S. (2021f). Spectrophotometric measurements of absorption coefficients by non-algal particles during RV POLARSTERN cruise PS121 from 11 Aug to 10 Sep 2019 [Dataset]. Pangaea. https://doi.org/10.1594/PANGAEA.938262

Bracher, A., Liu, Y., & Wiegmann, S. (2021g). Spectrophotometric measurements of absorption coefficients by phytoplankton during HEINCKE cruise HE462 in the North sea and Sogne Fjord from 29 April to 7 May 2016 [Dataset]. Pangaea. https://doi.org/10.1594/PANGAEA.938153

Bracher, A., Liu, Y., & Wiegmann, S. (2021h). Spectrophotometric measurements of absorption coefficients by phytoplankton during RV POLARSTERN cruise PS121 from 11 Aug to 10 Sep 2019 [Dataset]. Pangaea. https://doi.org/10.1594/PANGAEA.938260

Bracher, A., Liu, Y., Wiegmann, S., & Röttgers, R. (2021i). Absorption coefficients by coloured dissolved organic matter (CDOM) from North Sea to Fram Strait measured at fixed stations with a Liquid Waveguide Capillary Cell system during POLARSTERN cruise PS121 [Dataset]. Pangaea. https://doi.org/10.1594/PANGAEA.938472

Bracher, A., Liu, Y., Wiegmann, S., & Röttgers, R. (2021j). Absorption coefficients by coloured dissolved organic matter (CDOM) from North Sea to Fram Strait measured underway with a Liquid Waveguide Capillary Cell system during POLARSTERN cruise PS121 [Dataset]. Pangaea. https://doi.org/10.1594/PANGAEA.938473

Bracher, A., Liu, Y., Wiegmann, S., & Röttgers, R. (2021k). Absorption coefficients by coloured dissolved organic matter obtained at fixed stations with a Liquid Waveguide Capillary Cell system during HEINCKE cruise HE462 in the North Sea and Sogne Fjord [Dataset]. Pangaea. https://doi.org/10.1594/PANGAEA.938383

Bracher, A., Liu, Y., Wiegmann, S., & Röttgers, R. (2021l). Absorption coefficients by coloured dissolved organic matter obtained underway with a Liquid Waveguide Capillary Cell system during HEINCKE cruise HE462 in the North Sea and Sogne Fjord [Dataset]. Pangaea. https://doi.org/10.1594/PANGAEA.938384

Bracher, A., Liu, Y., Wiegmann, S., Xi, H., & Röttgers, R. (2021m). Absorption coefficients by coloured dissolved organic matter across the Atlantic Ocean measured at fixed stations with a Liquid Waveguide Capillary Cell system during POLARSTERN cruise PS113 [Dataset]. Pangaea. https://doi.org/10.1594/PANGAEA.938399

Bracher, A., Liu, Y., Wiegmann, S., Xi, H., & Röttgers, R. (2021n). Absorption coefficients by coloured dissolved organic matter across the Atlantic Ocean measured underway with a Liquid Waveguide Capillary Cell system during POLARSTERN cruise PS113 [Dataset]. Pangaea. https://doi.org/10.1594/PANGAEA.938400

Bracher, A., Liu, Y., Xi, H., & Wiegmann, S. (2021o). Spectrophotometric measurements of absorption coefficients by non-algal particles during POLARSTERN cruise PS113 along an Atlantic Transect [Dataset]. Pangaea. https://doi.org/10.1594/PANGAEA.938185

Bracher, A., Liu, Y., Xi, H., & Wiegmann, S. (2021p). Spectrophotometric measurements of absorption coefficients by phytoplankton during POLARSTERN cruise PS113 along an Atlantic Transect [Dataset]. Pangaea. https://doi.org/10.1594/PANGAEA.938178

Bracher, A., & Taylor, B. B. (2017). Phytoplankton pigment concentrations measured by HPLC during Maria S. Merian cruise MSM9/1 [Dataset]. Pangaea. https://doi.org/10.1594/PANGAEA.873070

Bracher, A., & Taylor, B. B. (2019). Particulate absorption during Polarstern cruise ANT-XXIV/1 (PS71)[Dataset]. Pangaea. https://doi.org/10.1594/PANGAEA.896946

Bracher, A., & Taylor, B. B. (2021a). Particulate absorption during Maria S. Merian cruise MSM09/1 [Dataset]. Pangaea. https://doi.org/10.1594/PANGAEA.937967

Bracher, A., & Taylor, B. B. (2021b). Particulate absorption during POLARSTERN cruise ANT-XXIV/4 (PS71) [Dataset]. Pangaea. https://doi.org/10.1594/PANGAEA.936540

Bracher, A., & Taylor, B. B. (2021c). Particulate absorption during POLARSTERN cruise ANT-XXVI/4 (PS75) [Dataset]. Pangaea. https://doi.org/10.1594/PANGAEA.936547

Bracher, A., & Taylor, B. B. (2021d). Phytoplankton absorption during POLARSTERN cruise ANT-XXVI/4 (PS75) [Dataset]. Pangaea. https://doi.org/10.1594/PANGAEA.937971

Bracher, A., Taylor, B. B., & Cheah, W. (2021a). Particulate absorption during RV Sonne expedition SO218 [Dataset]. Pangaea. https://doi.org/10.1594/PANGAEA.936553

Bracher, A., Taylor, B. B., & Cheah, W. (2021b). Phytoplankton absorption during SONNE cruise SO218 [Dataset]. Pangaea. https://doi.org/10.1594/PANGAEA.937982

Bracher, A., Taylor, M. H., Taylor, B. B., Dinter, T., Röttgers, R., & Steinmetz, F. (2015). Phytoplankton pigment concentrations during POLARSTERN cruise ANT-XXIII/1 [Dataset]. Pangaea. https://doi.org/10.1594/PANGAEA.871713

Bracher, A., & Wiegmann, S. (2019). Heincke Cruise HE462 phytoplankton pigments determined by HPLC [Dataset]. Pangaea. https://doi.org/10.1594/PANGAEA.899043

Bracher, A., & Wiegmann, S. (2021). Particulate absorption during RV Sonne expedition SO235 [Dataset]. Pangaea. https://doi.org/10.1594/PANGAEA.936587

Bracher, A., & Wiegmann, S. (2022). Phytoplankton pigment concentrations during POLARSTERN cruise PS121 from North sea to Fram in August to September 2019 [Dataset]. Pangaea. https://doi.org/10.1594/PANGAEA.941011

Bracher, A., Wiegmann, S., Xi, H., & Dinter, T. (2020). Phytoplankton pigment concentration and phytoplankton groups measured on water samples obtained during POLARSTERN cruise PS113 in the Atlantic Ocean [Dataset]. Pangaea. https://doi.org/10.1594/PANGAEA.911061

Brewin, R. J. W., Ciavatta, S., Sathyendranath, S., Skákala, J., Bruggeman, J., Ford, D., & Platt, T. (2019). The influence of temperature and community structure on light absorption by phytoplankton in the North Atlantic. *Sensors*, *19*(19), 4182. https://doi.org/10.3390/s19194182

Brewin, R. J. W., Hardman-Mountford, N. J., Lavender, S. J., Raitsos, D. E., Hirata, T., Uitz, J., et al. (2011). An intercomparison of bio-optical techniques for detecting dominant phytoplankton size class from satellite remote sensing. *Remote Sensing of Environment*, *115*(2), 325–339. https://doi.org/10.1016/j.rse.2010.09.004

Bricaud, A., Babin, M., Claustre, H., Ras, J., & Tièche, F. (2010). Light absorption properties and absorption budget of Southeast Pacific waters. *Journal of Geophysical Research*, *115*(C8), C08009. https://doi.org/10.1029/2009JC005517

Bricaud, A., Babin, M., Morel, A., & Claustre, H. (1995). Variability in the chlorophyll-specific absorption coefficients of natural phytoplankton: Analysis and parameterization. *Journal of Geophysical Research*, *100*(C7), 13321–13332. https://doi.org/10.1029/95JC00463

Bricaud, A., Claustre, H., Ras, J., & Oubelkheir, K. (2004). Natural variability of phytoplanktonic absorption in oceanic waters: Influence of the size structure of algal populations. *Journal of Geophysical Research*, *109*(C11), C11010. https://doi.org/10.1029/2004JC002419

Bricaud, A., & Morel, A. (1986). Light attenuation and scattering by phytoplanktonic cells: A theoretical modeling. *Applied Optics*, *25*(4), 571–580. https://doi.org/10.1364/AO.25.000571

Campin, J.-M., Heimbach, P., Losch, M., Forget, G., edhill3, Adcroft, A., et al., (2021). MITgcm (all versions) [Software]. Zenodo. https://doi.org/10.5281/zenodo.1409237

Casey, K., Rousseaux, C., Gregg, W. W., Boss, E., Chase, A., Craig, S., et al. (2020). A global compilation of in situ aquatic high spectral resolution inherent and apparent optical property data for remote sensing applications. *Earth System Science Data*, *12*(2), 1123–1139. https://doi.org/10.5194/essd-12-1123-2020

Cetinić, I. (2014). RemSensPOC (AE1319 and NH1418) [Dataset]. SeaBASS. https://doi.org/10.5067/SeaBASS/REMSENSPOC/DATA001

Chase, A. P., Boss, E., Cetinić, I., & Slade, W. (2017). Estimation of phytoplankton accessory pigments from hyperspectral reflectance spectra: Toward a global algorithm. *Journal of Geophysical Research: Oceans*, *122*(12), 9725–9743. https://doi.org/10.1002/2017JC012859

Ciotti, A. M., Lewis, M. R., & Cullen, J. J. (2002). Assessment of the relationships between dominant cell size in natural phytoplankton communities and the spectral shape of the absorption coefficient. *Limnology & Oceanography*, *47*(2), 404–417. https://doi.org/10.4319/lo.2002.47.2.0404

Clementson, L. A., & Wojtasiewicz, B. (2019). Dataset on the in vivo absorption characteristics and pigment composition of various phytoplankton species. *Data in Brief*, *25*, 104020. https://doi.org/10.1016/j.dib.2019.104020

Craig, S. E., Jones, C. T., Li, W. K. W., Lazin, G., Horne, E., Caverhill, C., & Cullen, J. J. (2012). Deriving optical metrics of coastal phytoplankton biomass from ocean colour. *Remote Sensing of Environment*, *119*, 72–83. https://doi.org/10.1016/j.rse.2011.12.007

CSIRO. (2020). *Australian-waters Earth observation phytoplankton-type products (AEsOP)* [Repository]. AEsOP-CSIRO. Retrieved from https://aesop.csiro.au/

Dutkiewicz, S. (2018). *Monod_radtrans numerical code V1* [Software]. Harvard Dataverse. https://doi.org/10.7910/DVN/R12GTM

Dutkiewicz, S., Hickman, A. E., & Jahn, O. (2018). Modelling ocean-colour-derived chlorophyll *a*. *Biogeosciences*, *15*(2), 613–630. https://doi.org/10.5194/bg-15-613-2018

Dutkiewicz, S., Hickman, A. E., Jahn, O., Gregg, W. W., Mouw, C. B., & Follows, M. J. (2015). Capturing optically important constituents and properties in a marine biogeochemical and ecosystem model. *Biogeosciences*, *12*(14), 4447–4481. https://doi.org/10.5194/bg-12-4447-2015

Duyens, L. N. M. (1956). The flattering of the absorption spectrum of suspensions, as compared to that of solutions. *Biochimica et Biophysica Acta*, *19*, 1–12. https://doi.org/10.1016/0006-3002(56)90380-8

Edwards, K. F., Thomas, M. K., Klausmeier, C. A., & Litchman, E. (2015). Light and growth in marine phytoplankton: Allometric, taxonomic, and environmental variation. *Limnology & Oceanography*, *60*(2), 540–552. https://doi.org/10.1002/lno.10033

Eisner, L. B., Twardowski, M. S., Cowles, T. J., & Perry, M. J. (2003). Resolving phytoplankton photoprotective: Photosynthetic carotenoid ratios on fine scales using in situ spectral absorption measurements. *Limnology & Oceanography*, *48*(2), 632–646. https://doi.org/10.4319/lo.2003.48.2.0632

Fay, A. R., & McKinley, G. A. (2014). Global open-ocean biomes: Mean and temporal variability. *Earth System Science Data*, *6*(2), 273–284. https://doi.org/10.5194/essd-6-273-2014

Ferreira, A., Ciotti, A. M., Mendes, C. R. B., Uitz, J., & Bricaud, A. (2017). Phytoplankton light absorption and the package effect in relation to photosynthetic and photoprotective pigments in the northern tip of Antarctic Peninsula. *Journal of Geophysical Research: Oceans*, *122*(9), 7344–7363. https://doi.org/10.1002/2017JC012964

Finkel, Z. V. (2004). Resource limitation alters the 3/4 size scaling of metabolic rates in phytoplankton. *Marine Ecology Progress Series*, *273*, 269–279. https://doi.org/10.3354/meps273269

Fujii, M., Boss, E., & Chai, F. (2007). The value of adding optics to ecosystem models: A case study. *Biogeosciences*, *4*(3), 817–835. https://doi.org/10.5194/bg-4-817-2007

Gallegos, C. L., Werdell, P. J., & McClain, C. R. (2011). Long-term changes in light scattering in Chesapeake Bay inferred from Secchi depth, light attenuation, and remote sensing measurements. *Journal of Geophysical Research*, *116*(C7), C00H08. https://doi.org/10.1029/2011JC007160

Garcia, H. E., Locarnini, R. A., Boyer, T. P., Antonov, J. I., Zweng, M. M., Baranova, O. K., & Johnson, D. R. (2010). World Ocean Atlas 2009, volume 4: Nutrients (phosphate, nitrate, and silicate). In *NOAA World Ocean Atlas* (Vol. *71*, p. 398). https://doi.org/10.1182/blood-2011-06-357442

Geider, R. J., Maclntyre, H. L., & Kana, T. M. (1998). A dynamic regulatory model of phytoplanktonic acclimation to light, nutrients, and temperature. *Limnology & Oceanography*, *43*(4), 679–694. https://doi.org/10.4319/lo.1998.43.4.0679

Gonçalves-Araujo, R., Wiegmann, S., & Bracher, A. (2018). Phytoplankton absorption coefficient spectra during POLARSTERN cruise ARK-XXVI/3 (PS78, TRANSARC) [Dataset]. Pangaea. https://doi.org/10.1594/PANGAEA.885246

Gregg, W. W. (2002). A coupled ocean–atmosphere radiative model for global ocean biogeochemical model, NASA Technical report series on global modeling and data assimilation. In *NASA/TM-2002-104606, 22*. Goddard Space Flight Center.

Gregg, W. W., & Casey, N. W. (2007). Modeling coccolithophores in the global oceans. *Deep Sea Research Part II: Topical Studies in Oceanography*, *54*(5–7), 447–477. https://doi.org/10.1016/j.dsr2.2006.12.007

Gregg, W. W., & Casey, N. W. (2009). Skill assessment of a spectral ocean-atmosphere radiative model. *Journal of Marine Systems*, *76*(1–2), 49–63. https://doi.org/10.1016/j.jmarsys.2008.05.007

Gregg, W. W., & Rousseaux, C. S. (2016). Directional and spectral irradiance in ocean models: Effects on simulated global phytoplankton, nutrients, and primary production. *Frontiers in Marine Science*, *3*, 240. https://doi.org/10.3389/fmars.2016.00240

Gregg, W. W., & Rousseaux, C. S. (2017). Simulating PACE global ocean radiances. *Frontiers in Marine Science*, *4*, 60. https://doi.org/10.3389/fmars.2017.00060

Gustafsson, M. S. M., Baird, M. E., & Ralph, P. J. (2014). Modeling photoinhibition-driven bleaching in Scleractinian coral as a function of light, temperature, and heterotrophy. *Limnology & Oceanography*, *59*(2), 603–622. https://doi.org/10.4319/lo.2014.59.2.0603

Hauck, J., Völker, C., Wang, T., Hoppema, M., Losch, M., & Wolf-Gladrow, D. A. (2013). Seasonally different carbon flux changes in the Southern Ocean in response to the southern annular mode. *Global Biogeochemical Cycles*, *27*(4), 1236–1245. https://doi.org/10.1002/2013GB004600

Hickman, A. E., Dutkiewicz, S., Williams, R. G., & Follows, M. J. (2010). Modelling the effects of chromatic adaptation on phytoplankton community structure in the oligotrophic ocean. *Marine Ecology Progress Series*, *406*, 1–17. https://doi.org/10.3354/meps08588

Hirata, T., Aiken, J., Hardman-Mountford, N., Smyth, T. J., & Barlow, R. G. (2008). An absorption model to determine phytoplankton size classes from satellite ocean colour. *Remote Sensing of Environment*, *112*(6), 3153–3159. https://doi.org/10.1016/j.rse.2008.03.011

Hoffmann, L. J., Peeken, I., Lochte, K., Assmy, P., & Veldhuis, M. (2006). Different reactions of Southern Ocean phytoplankton size classes to iron fertilization. *Limnology & Oceanography*, *51*(3), 1217–1229. https://doi.org/10.4319/lo.2006.51.3.1217

Hohn, S. (2009). *Coupling and decoupling of biogeochemical cycles in marine ecosystems* (PhD thesis). Universität Bremen.

Holtrop, T., Huisman, J., Stomp, M., Biersteker, L., Aerts, J., Grébert, T., et al. (2021). Vibrational modes of water predict spectral niches for photosynthesis in lakes and oceans. *Nature Ecology & Evolution*, *5*(1), 55–66. https://doi.org/10.1038/s41559-020-01330-x

IOCCG. (2020). *Synergy between Ocean Colour and biogeochemical/ecosystem models* (In S. Dutkiewicz, Ed., Vol. 19). International Ocean-Colour Coordinating Group (IOCCG). https://doi.org/10.25607/OBP-711

Jackson, T., Chuprin, A., Sathyendranath, S., Grant, M., Zühlke, M., Dingle, J., et al. (2020). Product user guide D3.4 [Report]. Retrieved from https://climate.esa.int/en/projects/ocean-colour/key-documents/

Jackson, T., Sathyendranath, S., & Mélin, F. (2017). An improved optical classification scheme for the Ocean Colour Essential Climate Variable and its applications. *Remote Sensing of Environment*, *203*, 152–161. https://doi.org/10.1016/j.rse.2017.03.036

Jeffrey, S. W., Vesk, M., & Mantoura, R. F. C. (1997). Phytoplankton pigments: Windows into the pastures of the sea. *Nature & Resources*, *33*, 14–29. Retrieved from http://hdl.handle.net/102.100.100/224372?index=1

JGOFS. (1994). Protocols for the joint global ocean flux study (JGOFS) core measurements. In *Intergovernmental Oceanographic Commission Manuals and Guides 29* (Vol. JGOFS Report 19, pp. 170). https://doi.org/10.25607/OBP-1409

Johnsen, G., Samset, O., Granskog, L., & Sakshaug, E. (1994). In vivo absorption characteristics in 10 classes of bloom-forming phytoplankton: Taxonomic characteristics and responses to photoadaptation by means of discriminant and HPLC analysis. *Marine Ecology Progress Series*, *105*, 149–157. https://doi.org/10.3354/meps105149

Jones, E. M., Baird, M. E., Mongin, M., Parslow, J., Skerratt, J., Lovell, J., et al. (2016). Use of remote-sensing reflectance to constrain a data assimilating marine biogeochemical model of the Great Barrier Reef. *Biogeosciences*, *13*(23), 6441–6469. https://doi.org/10.5194/bg-13-6441-2016

Kettle, H., & Merchant, C. J. (2008). Modeling ocean primary production: Sensitivity to spectral resolution of attenuation and absorption of light. *Progress in Oceanography*, *78*(2), 135–146. https://doi.org/10.1016/j.pocean.2008.04.002

Key, R. M., Kozyr, A., Sabine, C. L., Lee, K., Wanninkhof, R., Bullister, J., et al. (2004). A global ocean carbon climatology: Results from GLODAP. *Global Biogeochemical Cycles*, *18*(4), GB4031. https://doi.org/10.1029/2004GB002247

Key, T., McCarthy, A., Campbell, D. A., Six, C., Roy, S., & Finkel, Z. v. (2010). Cell size trade-offs govern light exploitation strategies in marine phytoplankton. *Environmental Microbiology*, *12*(1), 95–104. https://doi.org/10.1111/j.1462-2920.2009.02046.x

Kitidis, V., Stubbins, A. P., Uher, G., Upstill Goddard, R. C., Law, C. S., & Woodward, E. M. S. (2006). Variability of chromophoric organic matter in surface waters of the Atlantic Ocean. *Deep Sea Research Part II: Topical Studies in Oceanography*, *53*(14–16), 1666–1684. https://doi.org/10.1016/j.dsr2.2006.05.009

Kromkamp, J. C., Domin, A., Dubinsky, Z., Lehmann, C., & Schanz, F. (2001). Changes in photosynthetic properties measured by oxygen evolution and variable chlorophyll fluorescence in a simulated entrainment experiment with the cyanobacterium Planktothrix rubescens. *Aquatic Sciences*, *63*(3), 363–382. https://doi.org/10.1007/PL00001360

Kylling, A., Stamnes, K., & Tsay, S.-C. (1995). A reliable and efficient two-stream algorithm for spherical radiative transfer: Documentation of accuracy in realistic layered media. *Journal of Atmospheric Chemistry*, *21*(2), 115–150. https://doi.org/10.1007/BF00696577

Large, W. G., & Yeager, S. G. (2009). The global climatology of an interannually varying air–sea flux data set. *Climate Dynamics*, *33*(2–3), 341–364. https://doi.org/10.1007/s00382-008-0441-3

Lavaud, J., Rousseau, B., & Etienne, A. L. (2004). General features of photoprotection by energy dissipation in planktonic diatoms (Bacillariophyceae). *Journal of Phycology*, *40*(1), 130–137. https://doi.org/10.1046/j.1529-8817.2004.03026.x

Lee, Z. P., Carder, K. L., & Arnone, R. A. (2002). Deriving inherent optical properties from water color: A multiband quasi-analytical algorithm for optically deep waters. *Applied Optics*, *41*(27), 4957–4964. https://doi.org/10.1364/AO.41.005755

Lee, Z. P., Lubac, B., Werdell, J., & Arnone, R. (2009). An update of the quasi-analytical algorithm (QAA_v5) [Report]. Retrieved from http://www.ioccg.org/groups/Software_OCA/QAA_v5.pdf

Lefering, I., Röttgers, R., Utschig, C., & McKee, D. (2017). Uncertainty budgets for liquid waveguide CDOM absorption measurements. *Applied Optics*, *56*(22), 6357. https://doi.org/10.1364/AO.56.006357

Legendre, P. (2018). lmodel2: Model II regression. R package version 1.7-3. Retrieved from https://CRAN.R-project.org/package=lmodel2

Legendre, P., & Legendre, L. (1998). *Numerical ecology* (Second Eng). Elsevier Science B. V.

Liu, Y., Boss, E., Chase, A. P., Xi, H., Zhang, X., Röttgers, R., et al. (2018a). Phytoplankton pigment concentration measured by HPLC during POLARSTERN cruise PS93.2 [Dataset]. Pangaea. https://doi.org/10.1594/PANGAEA.894872

Liu, Y., Boss, E., Chase, A. P., Xi, H., Zhang, X., Röttgers, R., et al. (2018b). Phytoplankton pigment concentration measured by HPLC during POLARSTERN cruise PS99 [Dataset]. Pangaea. https://doi.org/10.1594/PANGAEA.894874

Liu, Y., Boss, E., Chase, A. P., Xi, H., Zhang, X., Röttgers, R., et al. (2019a). Phytoplankton pigment concentration estimated from underway AC-S particulate absorption data during POLARSTERN cruise PS93.2 [Dataset]. Pangaea. https://doi.org/10.1594/PANGAEA.898101

Liu, Y., Boss, E., Chase, A. P., Xi, H., Zhang, X., Röttgers, R., et al. (2019b). Phytoplankton pigment concentration measured by HPLC during POLARSTERN cruise PS107 [Dataset]. Pangaea. https://doi.org/10.1594/PANGAEA.894860

Liu, Y., Boss, E., Chase, A. P., Xi, H., Zhang, X., Röttgers, R., et al. (2019c). Spectral particulate absorption coefficients and their standard deviation derived from underway AC-S measurements during POLARSTERN cruise PS93.2 [Dataset]. Pangaea. https://doi.org/10.1594/PANGAEA.898119

Liu, Y., Boss, E., Chase, A. P., Xi, H., Zhang, X., Röttgers, R., et al. (2019d). Spectral particulate absorption coefficients and their standard deviation derived from underway AC-S measurements during POLARSTERN cruise PS99.2 [Dataset]. Pangaea. https://doi.org/10.1594/PANGAEA.898121

Liu, Y., Boss, E., Chase, A. P., Xi, H., Zhang, X., Röttgers, R., et al. (2019e). Spectral particulate absorption coefficients and their standard deviation derived from underway AC-S measurements during POLARSTERN cruise PS107 [Dataset]. Pangaea. https://doi.org/10.1594/PANGAEA.898117

Liu, Y., Hellmann, S., Wiegmann, S., & Bracher, A. (2019f). Phytoplankton pigment concentrations measured by HPLC during POLARSTERN cruise PS99.1 [Dataset]. Pangaea. https://doi.org/10.1594/PANGAEA.905502

Liu, Y., Wiegmann, S., & Bracher, A. (2019g). Spectrophotometric measurements of absorption coefficients and optical density by total particles, phytoplankton and non-algal particles during POLARSTERN cruise PS99 [Dataset]. Pangaea. https://doi.org/10.1594/PANGAEA.907648

Liu, Y., Wiegmann, S., & Bracher, A. (2019h). Spectrophotometric measurements of absorption coefficients and optical density by total particles, phytoplankton and non-algal particles during POLARSTERN cruise PS107 [Dataset]. Pangaea. https://doi.org/10.1594/PANGAEA.907419

Locarnini, R. A., Mishonov, A. v., Antonov, J. I., Boyer, T. P., Garcia, H. E., Baranova, O. K., et al. (2010). World Ocean Atlas 2009, volume 1: Temperature. In S. Levitus (Ed.), *NOAA Atlas NESDIS 68* (p. 184). U.S. Government Printing Office.

Lohrenz, S. E., Weidemann, A. D., & Tuel, M. (2003). Phytoplankton spectral absorption as influenced by community size structure and pigment composition. *Journal of Plankton Research*, *25*(1), 35–61. https://doi.org/10.1093/plankt/25.1.35

Lutz, V. A., Sathyendranath, S., & Head, E. J. H. (1996). Absorption coefficient of phytoplankton: Regional variations in the North Atlantic. *Marine Ecology Progress Series*, *135*, 197–213. https://doi.org/10.3354/meps135197

Mahowald, N., Luo, C., del Corral, J., & Zender, C. S. (2003). Interannual variability in atmospheric mineral aerosols from a 22-year model simulation and observational data. *Journal of Geophysical Research*, *108*(D12), 4352. https://doi.org/10.1029/2002JD002821

Malerba, M. E., & White, C. R. (2017). Phytoplankton size-scaling of net-energy flux across light and biomass gradients. *Ecology*, *98*(12), 3106–3115. https://doi.org/10.1002/ecy.2032

Marshall, B. R., & Smith, R. C. (1990). Raman scattering and in-water ocean optical properties. *Applied Optics*, *29*(1), 71. https://doi.org/10.1364/AO.29.000071

Marshall, H. L., Geider, R. J., & Flynn, K. J. (2000). A mechanistic model of photoinhibition. *New Phytologist*, *145*(2), 347–359. https://doi.org/10.1046/j.1469-8137.2000.00575.x

Marshall, J., Adcroft, A., Hill, C., Perelman, L., & Heisey, C. (1997). A finite-volume, incompressible Navier Stokes model for studies of the ocean on parallel computers. *Journal of Geophysical Research*, *102*(C3), 5753–5766. https://doi.org/10.1029/96JC02775

Matsuoka, A., Boss, E., Babin, M., Karp-Boss, L., Hafez, M., Chekalyuk, A., et al. (2017). Pan-Arctic optical characteristics of colored dissolved organic matter: Tracing dissolved organic carbon in changing Arctic waters using satellite ocean color data. *Remote Sensing of Environment*, *200*, 89–101. https://doi.org/10.1016/j.rse.2017.08.009

Miller, R. L., Belz, M., del Castillo, C., & Trzaska, R. (2002). Determining CDOM absorption spectra in diverse coastal environments using a multiple pathlength, liquid core waveguide system. *Continental Shelf Research*, *22*(9), 1301–1310. https://doi.org/10.1016/S0278-4343(02)00009-2

Moore, T. S., Campbell, J. W., & Dowell, M. D. (2009). A class-based approach to characterizing and mapping the uncertainty of the MODIS ocean chlorophyll product. *Remote Sensing of Environment*, *113*(11), 2424–2430. https://doi.org/10.1016/j.rse.2009.07.016

Morel, A. (1974). Optical properties of pure water and pure sea water. In N. G. Jerlov & E. S. Nielson (Eds.), *Optical Aspects of Oceanography* (pp. 1–24). Academic Press.

Morel, A., Antoine, D., & Gentili, B. (2002). Bidirectional reflectance of oceanic waters: Accounting for Raman emission and varying particle scattering phase function. *Applied Optics*, *41*(30), 6289–6306. https://doi.org/10.1364/AO.41.006289

Myers, J. (1980). On the algae: Thoughts about physiology and measurements of efficiency. In P. G. Falkowski (Ed.), *Primary productivity in the sea*, *Environmental Science Research* (Vol. 19). Springer. https://doi.org/10.1007/978-1-4684-3890-1_1

NOBM. (2019). *Monthly mean spectral downwelling irradiance* [Repository]. NASA Global Modelling and Assimilation Office.Retrieved from https://gmao.gsfc.nasa.gov/gmaoftp/NOBM/monthly/eds/

NOBPG. (2018). NASA bio-Optical Marine Algorithm Dataset v.2 [Dataset]. SeaBASS. Retrieved from https://seabass.gsfc.nasa.gov/wiki/NOMAD

O'Reilly, J. E., & Werdell, P. J. (2019). Chlorophyll algorithms for ocean color sensors – OC4, OC5 & OC6. *Remote Sensing of Environment*, *229*, 32–47. https://doi.org/10.1016/j.rse.2019.04.021

Oliver, R. L., & Ganf, G. G. (1988). The optical properties of a turbid reservoir and its phytoplankton in relation to photosynthesis and growth (mount bold reservoir, South Australia). *Journal of Plankton Research*, *10*(6), 1155–1177. https://doi.org/10.1093/plankt/10.6.1155

Organelli, E., Nuccio, C., Melillo, C., & Massi, L. (2011). Relationships between phytoplankton light absorption, pigment composition and size structure in offshore areas of the Mediterranean Sea. *Advances in Oceanography and Limnology*, *2*(2), 107–123. https://doi.org/10.1080/19475721.2011.607489

Peeken, I., & Murawski, S. (2016). Chlorophyll *a* measured on water bottle samples using HPLC during POLARSTERN cruise ARK-XXVI/3 (TRANSARC) [Dataset]. Pangaea. https://doi.org/10.1594/PANGAEA.867473

Peeken, I., & Nachtigall, K. (2014a). Phytoplankton pigments measured on water bottle samples during POLARSTERN cruise ANT-XXVI/3 [Dataset]. Pangaea. https://doi.org/10.1594/PANGAEA.869826

Peeken, I., & Nachtigall, K. (2014b). Pigments in surface water during POLARSTERN cruise ANT-XXVI/3 [Dataset]. Pangaea. https://doi.org/10.1594/PANGAEA.869827

Peloquin, J. M., Swan, C., Gruber, N., Vogt, M., Claustre, H., Ras, J., et al. (2013). The MAREDAT global database of high performance liquid chromatography marine pigment measurements. *Earth System Science Data*, *5*(1), 109–123. https://doi.org/10.5194/essd-5-109-2013

Polimene, L., Brunet, C., Allen, J. I., Butenschön, M., White, D. A., & Llewellyn, C. A. (2012). Modelling xanthophyll photoprotective activity in phytoplankton. *Journal of Plankton Research*, *34*(3), 196–207. https://doi.org/10.1093/plankt/fbr102

Pope, R. M., & Fry, E. S. (1997). Absorption spectrum 380–700 nm of pure water. II. Integrating cavity measurements. *Applied Optics*, *36*(33), 8710–8723. https://doi.org/10.1364/ao.36.008710

Porcar-Castell, A., Bäck, J., Juurola, E., & Hari, P. (2006). Dynamics of the energy flow through photosystem II under changing light conditions: A model approach. *Functional Plant Biology*, *33*(3), 229–239. https://doi.org/10.1071/FP05133

Raven, J. A., & Crawfurd, K. (2012). Environmental controls on coccolithophore calcification. *Marine Ecology Progress Series*, *470*, 137–166. https://doi.org/10.3354/meps09993

Röttgers, R., McKee, D., & Utschig, C. (2014). Temperature and salinity correction coefficients for light absorption by water in the visible to infrared spectral region. *Optics Express*, *22*(21), 25093. https://doi.org/10.1364/OE.22.025093

Rozanov, V. V., Rozanov, A. V., Kokhanovsky, A. A., & Burrows, J. P. (2014). Radiative transfer through terrestrial atmosphere and ocean: Software package SCIATRAN. *Journal of Quantitative Spectroscopy and Radiative Transfer*, *133*, 13–71. https://doi.org/10.1016/j.jqsrt.2013.07.004

Salihoglu, B., & Hofmann, E. E. (2007). Simulations of phytoplankton species and carbon production in the equatorial Pacific Ocean 1. Model configuration and ecosystem dynamics. *Journal of Marine Research*, *65*(2), 219–273. https://doi.org/10.1357/002224007780882587

Sathyendranath, S., Brewin, R. J. W., Brockmann, C., Brotas, V., Calton, B., Chuprin, A., et al. (2019). An ocean-colour time series for use in climate studies: The experience of the ocean-colour climate change initiative (OC-CCI). *Sensors*, *19*(19), 4285. https://doi.org/10.3390/s19194285

Sathyendranath, S., Cota, G., Stuart, V., Maass, H., & Platt, T. (2001). Remote sensing of phytoplankton pigments: A comparison of empirical and theoretical approaches. *International Journal of Remote Sensing*, *22*(2–3), 249–273. https://doi.org/10.1080/014311601449925

Sathyendranath, S., Lazzara, L., & Prieur, L. (1987). Variations in the spectral values of specific absorption of phytoplankton. *Limnology & Oceanography*, *32*(2), 403–415. https://doi.org/10.4319/lo.1987.32.2.0403

Schartau, M., Engel, A., Schröter, J., Thoms, S., Völker, C., & Wolf-Gladrow, D. (2007). Modelling carbon overconsumption and the formation of extracellular particulate organic carbon. *Biogeosciences*, *4*, 433–454. https://doi.org/10.5194/bg-4-433-2007

Silsbe, G. M., Behrenfeld, M. J., Halsey, K. H., Milligan, A. J., & Westberry, T. K. (2016). The CAFE model: A net production model for global ocean phytoplankton. *Global Biogeochemical Cycles*, *30*(12), 1756–1777. https://doi.org/10.1002/2016GB005521

Slade, W. H., Boss, E., Dall'Olmo, G., Langner, M. R., Loftin, J., Behrenfeld, M. J., et al. (2010). Underway and moored methods for improving accuracy in measurement of spectral particulate absorption and attenuation. *Journal of Atmospheric and Oceanic Technology*, *27*(10), 1733–1746. https://doi.org/10.1175/2010JTECHO755.1

Smith, R. C., & Baker, K. S. (1981). Optical properties of the clearest natural waters (200–800 nm). *Applied Optics*, *20*(2), 177–184. https://doi.org/10.1364/AO.20.000177

Soppa, M. A., Dinter, T., Taylor, B. B., & Bracher, A. (2013a). Particulate absorption during POLARSTERN cruise ANT-XXVI/3 [Dataset]. Pangaea. https://doi.org/10.1594/PANGAEA.819611

Soppa, M. A., Dinter, T., Taylor, B. B., & Bracher, A. (2013b). Phytoplankton absorption during POLARSTERN cruise ANT-XXVI/3 [Dataset]. Pangaea. https://doi.org/10.1594/PANGAEA.819612

Soppa, M. A., Dinter, T., Taylor, B. B., & Bracher, A. (2013c). Particulate absorption during POLARSTERN cruise ANT-XXVIII/3 [Dataset]. Pangaea. https://doi.org/10.1594/PANGAEA.819613

Soppa, M. A., Dinter, T., Taylor, B. B., & Bracher, A. (2013d). Phytoplankton absorption during POLARSTERN cruise ANT-XXVIII/3 [Dataset]. Pangaea. https://doi.org/10.1594/PANGAEA.819614

Stow, C. A., Jolliff, J., McGillicuddy, D. J., Doney, S. C., Allen, J. I., Friedrichs, M. A. M., et al. (2009). Skill assessment for coupled biological/physical models of marine systems. *Journal of Marine Systems*, *76*(1–2), 4–15. https://doi.org/10.1016/j.jmarsys.2008.03.011

Stramski, D., Boss, E., Bogucki, D., & Voss, K. J. (2004). The role of seawater constituents in light backscattering in the ocean. *Progress in Oceanography*, *61*(1), 27–56. https://doi.org/10.1016/j.pocean.2004.07.001

Stramski, D., Bricaud, A., & Morel, A. (2001). Modeling the inherent optical properties of the ocean based on the detailed composition of the planktonic community. *Applied Optics*, *40*(18), 2929. https://doi.org/10.1364/AO.40.002929

Stramski, D., Reynolds, R. A., Babin, M., Kaczmarek, S., Lewis, M. R., Röttgers, R., et al. (2008). Relationships between the surface concentration of particulate organic carbon and optical properties in the eastern South Pacific and eastern Atlantic Oceans. *Biogeosciences*, *5*(1), 171–201. https://doi.org/10.5194/bg-5-171-2008

Tagliabue, A., Mtshali, T., Aumont, O., Bowie, A. R., Klunder, M. B., Roychoudhury, A. N., & Swart, S. (2012). A global compilation of dissolved iron measurements: Focus on distributions and processes in the Southern Ocean. *Biogeosciences*, *9*(6), 2333–2349. https://doi.org/10.5194/bg-9-2333-2012

Taylor, B. B., & Bracher, A. (2012a). Particulate absorption during SONNE cruise SO202/2 (TRANSBROM) [Dataset]. Pangaea. https://doi.org/10.1594/PANGAEA.804549

Taylor, B. B., & Bracher, A. (2012b). Phytoplankton absorption during SONNE cruise SO202/2 (TRANSBROM) [Dataset]. Pangaea. https://doi.org/10.1594/PANGAEA.804552

Taylor, B. B., & Bracher, A. (2017). Pigment concentrations measured in surface water during SONNE cruise SO202/2 (TRANSBROM) [Dataset]. Pangaea. https://doi.org/10.1594/PANGAEA.880235

Taylor, B. B., Torrecilla, E., Bernhardt, A., Taylor, M. H., Peeken, I., Röttgers, R., et al. (2011a). Bio-optical provinces in the eastern Atlantic Ocean and their biogeographical relevance. *Biogeosciences*, *8*(12), 3609–3629. https://doi.org/10.5194/bg-8-3609-2011

Taylor, B. B., Torrecilla, E., Bernhardt, A., Taylor, M. H., Peeken, I., Röttgers, R., et al. (2011b). Particulate absorption during POLARSTERN cruise ANT-XXV/1 [Dataset]. Pangaea. https://doi.org/10.1594/PANGAEA.819098

Taylor, B. B., Torrecilla, E., Bernhardt, A., Taylor, M. H., Peeken, I., Röttgers, R., et al. (2011c). Phytoplankton absorption during POLARSTERN cruise ANT-XXV/1 [Dataset]. Pangaea. https://doi.org/10.1594/PANGAEA.819097

Taylor, B. B., Torrecilla, E., Bernhardt, A., Taylor, M. H., Peeken, I., Röttgers, R., et al. (2011d). Pigments of phytoplankton during POLARSTERN cruise ANT-XXV/1 [Dataset]. Pangaea. https://doi.org/10.1594/PANGAEA.819070

Uitz, J., Claustre, H., Morel, A., & Hooker, S. B. (2006). Vertical distribution of phytoplankton communities in open ocean: An assessment based on surface chlorophyll. *Journal of Geophysical Research*, *111*(C8), C08005. https://doi.org/10.1029/2005JC003207

Valente, A., Sathyendranath, S., Brotas, V., Groom, S., Grant, M., Taberner, M., et al. (2019). A compilation of global bio-optical in situ data for ocean-colour satellite applications – Version two. *Earth System Science Data*, *11*(3), 1037–1068. https://doi.org/10.5194/essd-11-1037-2019

Wagner, H., Jakob, T., & Wilhelm, C. (2006). Balancing the energy flow from captured light to biomass under fluctuating light conditions. *New Phytologist*, *169*(1), 95–108. https://doi.org/10.1111/j.1469-8137.2005.01550.x

Webb, W. L., Newton, M., & Starr, D. (1974). Carbon dioxide exchange of Alnus rubra: A mathematical model. *Oecologia*, *17*(4), 281–291. https://doi.org/10.1007/BF00345747

Werdell, P. J., & Bailey, S. W. (2005). An improved in-situ bio-optical data set for ocean color algorithm development and satellite data product validation. *Remote Sensing of Environment*, *98*(1), 122–140. https://doi.org/10.1016/j.rse.2005.07.001

Werdell, P. J., McKinna, L. I. W., Boss, E., Ackleson, S. G., Craig, S. E., Gregg, W. W., et al. (2018). An overview of approaches and challenges for retrieving marine inherent optical properties from ocean color remote sensing. *Progress in Oceanography*, *160*, 186–212. https://doi.org/10.1016/j.pocean.2018.01.001

Wiegmann, S., Liu, Y., & Bracher, A. (2019). Spectrophotometric measurements of absorption coefficients by total particles, phytoplankton and non-algal particles during POLARSTERN cruise PS93.2 [Dataset]. Pangaea. https://doi.org/10.1594/PANGAEA.907605

Wolanin, A., Soppa, M., & Bracher, A. (2016). Investigation of spectral band requirements for improving retrievals of phytoplankton functional types. *Remote Sensing*, *8*(10), 871. https://doi.org/10.3390/rs8100871

Xiu, P., & Chai, F. (2014). Connections between physical, optical and biogeochemical processes in the Pacific Ocean. *Progress in Oceanography*, *122*, 30–53. https://doi.org/10.1016/j.pocean.2013.11.008

Zheng, G., & DiGiacomo, P. M. (2017). Uncertainties and applications of satellite-derived coastal water quality products. *Progress in Oceanography*, *159*, 45–72. https://doi.org/10.1016/j.pocean.2017.08.007